Dissertation

An Evaluation and Parameterization of Stably Stratified Turbulence: Insights on the Atmospheric Boundary Layer and Implications for Wind Energy

Submitted by

Jordan M. Wilson

Department of Civil and Environmental Engineering

In partial fulfillment of the requirements

For the Degree of Doctor of Philosophy

Colorado State University

Fort Collins, Colorado

Fall 2014

Doctoral Committee:

Advisor: Subhas K. Venayagamoorthy

Thomas Birner
Paul R. Heyliger
Patrick J. Moriarty

Abstract

An Evaluation and Parameterization of Stably Stratified Turbulence: Insights on the Atmospheric Boundary Layer and Implications for Wind Energy

This research focuses on the dynamics of turbulent mixing under stably stratified flow conditions. Velocity fluctuations and instabilities are suppressed by buoyancy forces limiting mixing as stability increases and turbulence decreases until the flow relaminarizes. Theories that ubiquitously assume turbulence collapse above a critical value of the gradient Richardson number (e.g. $Ri > Ri_c$) are common in meteorological and oceanographic communities. However, most theories were developed from results of small-scale laboratory and numerical experiments with energetic levels several orders of magnitude less than geophysical flows. Geophysical flows exhibit strong turbulence that enhances the transport of momentum and scalars. The mixing length for the turbulent momentum field, L_M, serves as a key parameter in assessing large-scale, energy-containing motions. For a stably stratified turbulent shear flow, the shear production of turbulent kinetic energy, P, is here considered to be of greater relevance than the dissipation rate of turbulent kinetic energy, ε. Thus, the turbulent Reynolds number can be recast as $Re \equiv k^2/(\nu P)$ where k is the turbulent kinetic energy, allowing for a new perspective on flow energetics. Using an ensemble data set of high quality direct numerical simulation (DNS) results, large-eddy simulation (LES) results, laboratory experiments, and observational field data of the stable atmospheric boundary layer (SABL), the dichotomy of data becomes apparent. High mixing rates persist to strong stability (e.g. $Ri \approx 10$) in the SABL whereas numerical and laboratory results confirm turbulence collapse

for $Ri \sim O(1)$. While this behavior has been alluded to in literature, this direct comparison of data elucidates the disparity in universal theories of stably stratified turbulence.

From this theoretical perspective, a Reynolds-averaged framework is employed to develop and evaluate parameterizations of turbulent mixing based on the competing forces of mean shear and buoyancy frequency, S and N, respectively. Length scale estimates for L_M are given by $L_{kS} \equiv k^{1/2}/S$ and $L_{kN} \equiv k^{1/2}/N$, where L_{kS} provides an accurate estimate for eddy viscosity, ν_t, under neutral to strongly stable conditions for SABL data. The relative influence of shear and buoyancy are given by the ratio of the respective time scales, S^{-1} and N^{-1}, with the pertinent time scale of the large-scale motions, $T_P \equiv k/P$, through the parameters ST_P and NT_P. L_{kS}'s range of applicability is further assessed in a ST_P-NT_P parameter space. In developing these parameterizations, the stress-intensity ratio, c^2, is evaluated using high-Re stably stratified data and is shown to exhibit a near constant value ($c^2 \approx 0.25$) for stably stratified geophysical turbulence. These findings provide a clear trajectory for numerical modeling of stably stratified geophysical shear turbulence without reliance on stability or damping functions, tuning parameters, or artificial parameterizations. An initial modeling study of moderate-Re channel and Ekman layer flows using the proposed parameterizations confirms this supposition.

Finally, it is in this new light that large-scale implications of wind energy can now be considered. As a first step in this process, computational fluid dynamics (CFD) studies of wind turbine interactions are carried out under neutrally stratified conditions. Simulations clearly show that actuator line models provide efficacy in wake generation, interaction, and restoration and highlight model requirements for stably stratified conditions. Results suggest

that standard horizontal spacing of 5–10 rotor diameters yield significant reductions in power output and increases turbulence intensity and fatigue loading.

Acknowledgements

Before beginning this dissertation, I would like to acknowledge the people that have made this work possible.

I sincerely thank my advisor, Karan Venayagamoorthy, for taking a chance on me many years ago. Without his support and direction, this work would have not been possible. Karan's infectious enthusiasm, diligent work ethic, and investment in students' lives beyond the classroom has made my time here a true joy. As a mentor and friend, he has provided encouragement and guidance for which I am deeply thankful. Looking forward, I hope to follow his example as an excellent teacher and researcher.

I also thank my committee members, Thomas Birner, Paul Heyliger, and Patrick Moriarty, for their time in reviewing this work and providing valuable input.

I thank my many colleagues, especially Ben Mater, Farid Karimpour, and Zach Elliot, for their friendship over the years. I am thankful for our many lively discussions whether research-related or dealing with the bigger questions of life and for time spent in the great outdoors of Colorado.

Finally, I am especially grateful to my lovely wife, Paige, for her patience and endless love and support. Thanks to my parents, Jeff and Teresa, and siblings, Sara and Ryan, for their encouragement in moving across the country to pursue my degree.

I would like to gratefully acknowledge funding from the National Science Foundation under CAREER grant OCE-1151838, the Center for Research and Education in Wind (CREW), and the Colorado State University Clean Energy Supercluster. Colorado State University's Information Science & Technology Center (ISTeC) Cray HPC System supported by the National Science Foundation under Grant CNS-0923386 provided computational resources.

This research would not have been possible in large part without the contributions of high quality data by numerous individuals to whom I am grateful, specifically: Lucinda Shih, Manuel García-Villalba, Sergio Hoyas, Katsuhiro Miyashita, and Enrico Deusebio for detailed post-processed DNS data sets; Kurt Keller for wind tunnel data; Pete Sullivan and the GABLS organizing committee for LES data; the SHEBA Atmospheric Surface Flux Group and the individuals and institutions of the CASES-99 and FLOSSII initiatives for valuable SABL data sets; and Cole Davis for full rotor simulations of the NREL 5MW turbine.

Table of Contents

Abstract ii

Acknowledgements v

List of Tables x

List of Figures xi

Chapter 1. Introduction 1

1.1. Motivation 1

1.2. Objectives 4

1.3. Dissertation Layout 6

Chapter 2. Governing Equations 8

2.1. Conservation Laws 8

2.2. Equation of State 9

2.3. Energy Equation 10

2.4. Mean Equations 11

2.5. Flux-Gradient Hypotheses 12

Chapter 3. Literature Review 15

3.1. Turbulence in Geophysical Flows 15

3.2. Stably Stratified Turbulence 19

3.3. Parameterizations of Turbulence 24

3.4. Implications on Wind Energy 34

3.5. Summary 37

Chapter 4. An Analysis of Turbulent Mixing in Strongly Stably Stratified Flows 39

4.1. Introduction 39

4.2. Background 41

4.3. Analysis/Results 42

4.4. Conclusions 49

Chapter 5. Turbulence Parameterizations for Strongly Stable Stratification 51

5.1. Introduction 51

5.2. Description of Data Sets 56

5.3. Theoretical Formulation 58

5.4. *A priori* Analysis of the SABL Vertical Profile 69

5.5. Conclusions 75

Chapter 6. Numerical Modeling of Stably Stratified Turbulence with a Hybrid One-Equation Turbulence Closure Model 77

6.1. Introduction 77

6.2. Theoretical Background 78

6.3. Model Description 81

6.4. Numerical Methods 83

6.5. Results 86

6.6. Conclusions 90

Chapter 7. Modeling Wind Turbine Interactions in the Atmospheric Boundary Layer . 93

7.1. Introduction 93

7.2. Theory 96

7.3. Results and Discussion 107

7.4. Conclusions 115

Chapter 8. Summary and Conclusions 117

8.1. Summary of Research 117

8.2. Conclusions on Key Findings 118

8.3. Suggestions for Future Research 119

References 121

List of Tables

4.1 Description of evaluated data sets 43

6.1 Additional model closures 86

7.1 k-ω SST model constants 99

7.2 FRM high-resolution grid sizing 111

List of Figures

3.1 Energy spectrum of turbulence 16

3.2 Schematic of the ABL vertical structure 23

4.1 ν_{eff}/ν as a function of Ri 44

4.2 ν_{eff}/ν as a function of NT_P. Symbols colored by Re_P 45

4.3 R_f as a function of Ri and Re_P 46

4.4 Comparison of L_M and $0.5L_{kS}$ with symbols colored by ST_P and NT_P 47

4.5 Parameter space for stably stratified turbulence 48

5.1 C_{kS} as a function of Ri for SABL data 62

5.2 C_{kS} as a function of Re_{SP} for SABL data 63

5.3 Comparisons of $0.50L_{kS}$ and $0.25L_{kN}$ with L_M 64

5.4 Comparisons of $\tilde{K}_{M_{kS}} \simeq 0.25L_{kS}k^{1/2}$ and $\tilde{K}_{M_{kN}} \simeq 0.13L_{kN}k^{1/2}$ with K_M 66

5.5 Pr_t as a function of Ri 68

5.6 Comparison of $\tilde{K}_H \simeq K_M/Pr_{t_{\text{VS10}}}$ and $\tilde{K}_H \simeq K_M/Pr_{t_{0.74}}$ with K_H 70

5.7 Comparison of $\tilde{K}_H \simeq \tilde{K}_{M_{kS}}/Pr_{t_{\text{VS10}}}$ and $\tilde{K}_H \simeq \tilde{K}_{M_{kN}}/Pr_{t_{\text{VS10}}}$ with K_H 71

5.8 C_{kS} as a function of Ri for SABL and LES data 72

5.9 *A priori* analysis eddy viscosity and diffusivity for LES data 74

6.1 c as a function ν_{eff}/ν for channel and Ekman layer flows 79

6.2 $|S^+|^{-1}$ versus z/δ for channel and Ekman layer flows 80

6.3 Comparison of mixing length estimations for channel flow 81

6.4 Channel flow results for $Re_\tau = 550$ and $Ri_\tau = 60$ with $Pr_t = 0.74$ 87

6.5 Channel flow results for $Re_\tau = 550$ and $Ri_\tau = 60$ with $Pr_{t_{\text{VS10}}}$ 87

6.6 Channel flow results for $Re_\tau = 550$ and $Ri_\tau = 60$ with $Pr_{t_{\text{KV14}}}$ 88

6.7 Channel flow results for $Re_\tau = 550$ and $Ri_\tau = 120$ with $Pr_t = 0.74$ 88

6.8 Channel flow results for $Re_\tau = 550$ and $Ri_\tau = 120$ with $Pr_{t_{\text{VS10}}}$ 89

6.9 Channel flow results for $Re_\tau = 550$ and $Ri_\tau = 120$ with $Pr_{t_{\text{KV14}}}$ 89

6.10 Ekman layer results for $Pr_t = 0.74$ at $tf = 1.8$ 90

6.11 Ekman layer results for $Pr_{t_{\text{VS10}}}$ at $tf = 1.8$ 90

7.1 Schematic of two inline turbines 95

7.2 Vertical profiles of $\overline{u}$ and k for HAWT simulations 102

7.3 Grid independence study for ADM, ALM, and FRM rotor models 104

7.4 Computational grid for FRM simulations 108

7.5 Contours of streamwise velocity for single turbine models 109

7.6 Comparison of downstream vertical profiles of streamwise velocity 109

7.7 Contours of turbulence intensity for single turbine models 110

7.8 Grid independence study of maximum turbine blade pressure 112

7.9 Contours of pressure along blade surfaces 112

7.10 Contours of streamwise velocity for inline turbines spaced at $5D$ 113

7.11 Comparison of downstream vertical profiles of streamwise velocity 114

7.12 Contours of turbulence intensity for inline turbines spaced at $5D$ 114

CHAPTER 1

Introduction

1.1. Motivation

The need for clean, renewable, and reliable energy sources is undeniable. Power generation from wind energy represents the most sustainable form of renewable energy in terms of cost and environmental impact, even ahead of hydro power. Geophysical flows, such as the atmospheric boundary layer (ABL), are very energetic with the potential for a near endless supply of energy. Inherently, strong energetics lead to high levels of turbulence influenced by wind shear, stratification, and boundary proximity. Stable stratification occurs when warm air flows over a cooler surface or through radiative cooling of the Earth's surface and less dense fluid settles over heavier fluid. Buoyancy forces limit turbulent perturbations and instabilities yielding favorable conditions for inertial phenomena such as the development of low-level jets, formation and propagation of internal gravity waves, and shear instabilities. Low-level jets have the potential for massive increases in power generation; however, high shear levels and very energetic bursts of three-dimensional turbulence cause excessive fatigue loads on turbine blades and structures.

A better understanding of stably stratified turbulence in geophysical flows is needed to accurately assess wind resources, power generation, and design specifications in addition to global transport processes pertaining to climate change, pollution, and weather prediction. Much fundamental knowledge has been garnered from direct numerical simulation (DNS) and laboratory experiments in addition to field campaigns. Yet, the Reynolds number, defined by the ratio of characteristic turbulent velocity and length scales, $\mathcal{U}$ and $\mathcal{L}$, to the kinematic viscosity, ν given by $Re = \mathcal{U}\mathcal{L}/\nu$, in these flows typically differ by several orders

of magnitude. Thus, a key question is do energetics play a role in the characteristic behavior of stably stratified turbulence? Does turbulence ubiquitously collapse when stratification is sufficiently strong? An overarching goal of this research is to investigate the influence of energetics on turbulent mixing in strongly stable flow conditions. Of primary importance are the large-scale turbulent motions responsible for momentum transport. Dimensional analysis is a valuable tool from which the characteristic scales of motion can be assessed and used to evaluate flow processes and competing forces. Dimensional analysis also elucidates the energetic influence on stably stratified turbulent mixing.

Fundamental knowledge of the pertinent length, time, and velocity scales of large-scale turbulent motions provides a basis for parameterizations and theoretical and numerical model development. Operational predictive models are essential to understanding many global processes. Historically, numerical modeling of the stable atmospheric boundary layer (SABL) has focused on performance and/or ad hoc parameterizations. In this dissertation, a holistic approach is taken to model development where parameterizations are developed from fundamental analysis and evaluated for efficacy through analytical and numerical endeavors. Reassessment of key model quantities from highly energetic observational data highlights the disparity in many current models.

The research presented in this dissertation is motivated by the need for a complete description of strongly stably stratified turbulence in geophysical flows. Key aspects of highly energetic, stable flow conditions are absent from many theoretical and numerical models. The specific motivating factors for this research are:

- *A need for an energetics-based approach to theories of stably stratified turbulence.* Traditionally, theories have promoted that turbulence collapses marked by the onset

of fossilization beyond a critical limit of stability. In geophysical flows, turbulence never truly ceases to exist as a result of nonlinear interactions between turbulent and non-turbulent motions. While numerous studies have alluded to the differences between laboratory and observational scales, a direct comparison between such data is needed to elucidate that energetics greatly influence mixing at high levels of stratification.

- *A need for holistic parameterizations of turbulent mixing in stable flow conditions.* The bulk of turbulence parameterizations for stable stratification are based on the notion of turbulence collapse. Many existing parameterizations are also based on early surface-based similarity theory whose applicability have been questioned in recent years especially under very stable stratification. Such methodology clearly does not account for the strongly stable, high-Re regimes and precludes the occurrence of such events which are important to global transport processes. As previously mentioned, a focus on performance or results-based parameterization (e.g. tuning of model constants) can lead to unrealistic physics. Numerous stability and damping functions also rely on similarity theory or nonlocal flow descriptions. Large-scale atmospheric models require boundary layer parameterizations linking turbulent transport to the free atmosphere. If turbulence levels are inaccurate, unrealistic levels of mixing can severely affect model accuracy of significance to large-scale (e.g. global) predictive models.
- *A need to connect fundamental boundary layer dynamics with wind energy applications.* Computational fluid dynamics (CFD) modeling of wind turbines requires additional physical considerations compared to simpler boundary layer flows. In the

Reynolds-averaged framework, several models of horizontal-axis wind turbines exist with varying levels of sophistication and associated computational requirements. A need exists to connect fundamental boundary layer dynamics with turbine wake generation, propagation, and decay through higher-order turbulence model closures.

1.2. Objectives

As previously discussed, the main focus of this research is to fundamentally evaluate the energetic influence on stably stratified turbulence. Using high quality direct numerical simulation (DNS), large-eddy simulation (LES), laboratory, and observational data sets, dimensional analysis is used to assess the scales of turbulent mixing and to develop relevant parameterizations. These parameterizations provide a basis for analytical and numerical models. The main objectives of the research presented in this dissertation are:

(1) **To clearly illustrate the dynamic differences in turbulent mixing at high and low levels of energetics under strongly stable stratification.** The primary contribution of this dissertation investigates strong turbulent mixing challenging the notion that turbulence unassumingly shuts off for very stable conditions in geophysical flows. This analysis is contained in chapter 4 using stably stratified DNS, laboratory, and field data. This objective is motivated by the disconnect in theories of stably stratified turbulence in relatively low-Re numerical/laboratory experiments and high-Re geophysical flows. In this study, only turbulent shear flows are considered where the shear production of turbulent kinetic energy, P, is considered of greater significance than the dissipation rate of turbulent kinetic energy, ε,

in describing the large-scale motions. This framework forms the basis for parameterizations of turbulent mixing presented in the later portion of chapter 4 and the entirety of chapter 5.

(2) **To develop parameterizations of turbulent mixing applicable to a range of stratified flow conditions from near-neutral to strongly stable.** A second major contribution of this research is the study of a length scale estimate for the mixing length of the turbulent momentum field, L_M, given by the ratio of turbulent kinetic energy, k, to mean shear, $S = \partial \overline{U}_i / \partial x_j$, written as $L_{kS} \equiv k^{1/2}/S$. The range of applicability of L_{kS} for high- and low-Re flow is additionally assessed through through a parameter space in chapter 4 based on the the shear parameter, ST_P where $T_P \equiv k/P$ is the turbulence production time scale, and the buoyancy parameter, NT_P where N is the buoyancy frequency. Additionally, the stress-intensity ratio, $c^2 = |\overline{u_i' u_j'}|/k$, a key dimensionless ratio in Reynolds-averaged models, is investigated using high-Re stably stratified geophysical observations. Finally, estimates for eddy viscosity, ν_t, are evaluated from an *a priori* analysis of observational and large-eddy simulation (LES) data in chapter 5. The numerical implementation of the developed parameterizations in chapter 6 shows excellent agreement with DNS data.

(3) **To assess the viability of wind turbine models for efficacy in prediction of near and far wake interactions.** As wind turbines continue to reach higher into the atmosphere, understanding the flow dynamics and interactions of downstream wakes is essential to estimating power production and fatigue loading. CFD wind turbine models are evaluated under neutral stratification conditions for accuracy and efficiency for (i) a single turbine and (ii) two inline turbines spaced 5 diameters

apart. This objective serves to lay the groundwork for future research which seeks to investigate the dynamics and performance of wind turbines under stably stratified atmospheric conditions.

1.3. Dissertation Layout

The individual chapters (especially chapters 4, 5, 6, and 7) can be read as stand-alone works where it is possible that portions of the introductory material may also be contained in the literature review. The layout of this dissertation is as follows:

- **Chapter 2** contains a brief discussion of governing equations pertinent to the study of turbulent flows.
- **Chapter 3** contains a literature review beginning with an overview of turbulence theory which is then followed by a discussion of literature pertaining to stably stratified turbulence, historical development of turbulence parameterizations, and implications for wind energy.
- **Chapter 4** contains an analysis of stably stratified turbulence through an ensemble data set wherein objective 1 is thoroughly addressed.
- **Chapter 5** contains a continuation of the theoretical framework presented in chapter 4 with the subsequent development of turbulence parameterizations. This chapter covers several topics given in objective 2.
- **Chapter 6** contains a numerical model implementation from the proposed parameterizations from chapters 4 and 5. This chapter concludes the topics addressed in objective 2.
- **Chapter 7** contains an intercomparison of CFD wind turbine models pertaining to objective 3.

- **Chapter 8** contains a summary of the key findings and contributions of the research in this dissertation.

CHAPTER 2

Governing Equations

To begin the study of any fluid flow, certain assumptions must be made regarding the nature of the fluid. The first major concept is the *continuum hypothesis* which states that even for a flow of the smallest scales (e.g. 10^{-4} m), the length and velocity scales far exceed the molecular scales. This hypothesis then allows for consideration of continuous properties of the flow and regarding molecular properties as inconsequential. The following sections discuss the pertinent conservation laws and develop a framework through which to study turbulent flows.

2.1. Conservation Laws

2.1.1. Continuity Equation. The principle of mass conservation states that the total mass of a system remains constant with time. The system mass is given by the product of the fluid density, ρ, and volume, $\mathcal{V}$. The continuity equation using Einstein summation convention can be written as

$$\frac{\partial \rho}{\partial t} + \frac{\partial \left(\rho U_i\right)}{\partial x_i} = 0, \tag{2.1}$$

where U_i is the velocity field. For constant density-flows, equation (2.1) can be simplified to

$$\frac{\partial U_i}{\partial x_i} = 0. \tag{2.2}$$

The flow is thus said to be *divergence-free* where the net flux through all surfaces of the volume are zero.

2.1.2. Momentum Equation. Newton's second law states that the acceleration of a fluid is proportional to the forces applied and varies inversely to the fluid mass. The dominant external force is the gravitational potential, $\mathbf{\Psi} = gz$ where g is the gravitational acceleration and z is the vertical coordinate. The momentum equation is given by

$$\rho \frac{DU_j}{Dt} = \mu \frac{\partial^2 U_j}{\partial x_i \partial x_i} - \frac{\partial p}{\partial x_j} - \frac{\partial \mathbf{\Psi}}{\partial x_j}, \tag{2.3}$$

where D/Dt is the substantive (or material) derivative, μ is the dynamic viscosity, and p is the pressure field. Equation 2.3 represents a set of nonlinear partial differential equations for most flows of practical consideration. Tractable solutions to equation (2.3) rely on flow approximations (e.g. Poisson's equations) whereas applications to large-scale dynamic flows require numerical integration.

2.1.3. Passive Scalar Equation. In addition to momentum, flows can also transport passive scalars such as sediments or contaminants. Conservative passive scalars do not influence the material properties of the flow and are governed according to

$$\frac{D\phi}{Dt} = \Gamma \frac{\partial^2 \phi}{\partial x_i^2}, \tag{2.4}$$

where ϕ represents a passive scalar quantity and Γ is the diffusivity. If Γ represents thermal diffusivity, then the Prandtl number gives the relationship to viscosity as $Pr = \nu/\Gamma$. Similarly, if Γ is the molecular (mass) diffusivity, the Schmidt number is given by $Sc = \nu/\Gamma$.

2.2. Equation of State

For a baroclinic fluid, the pressure field is a function of density, temperature, and salinity in the case of oceanic flows, $p = p(\rho, T, S)$. For an ideal gas, the kinetic energy of molecules

can be related to the pressure and temperature through

$$p = \rho RT, \tag{2.5}$$

where $R \equiv k_B/m$ is the specific gas constant ($R_{\text{air}} = 287 J/kg \cdot K$), k_B is the Boltzmann constant, and m is mass.

2.3. Energy Equation

The first law of thermodynamics states that internal energy of a system equals the heat supplied minus the work done by the system, $dI = dQ - dW$ where dI is the internal energy change, dQ is the heat transfer, and dW is pressure work. For an adiabatic flow in thermal equilibrium, an equation for the transport of total energy is given by

$$\rho \frac{DE}{Dt} = -\frac{\partial (pU_i)}{\partial x_i}, \tag{2.6}$$

where $E = E_K + I + E_P$ is the total energy, $E_K = U_i^2/2$ is the kinetic energy, and $E_P = gz$ is the gravitational potential energy. The thermodynamic equations for density and temperature under adiabatic conditions can be written as

$$\frac{D\rho}{Dt} = \kappa_\rho \frac{\partial^2 \rho}{\partial x_i^2}, \tag{2.7}$$

$$\frac{DT}{Dt} = \kappa_T \frac{\partial^2 T}{\partial x_i^2}, \tag{2.8}$$

where κ_ρ is the molecular diffusivity for density and κ_T is the molecular diffusivity for heat where $\kappa_\rho \approx \kappa_T$. In the atmosphere, it is often more convenient to use potential temperature,

θ, which can be defined as

$$\theta \equiv T \left(\frac{p}{p_0} \right)^{-R/c_p}, \tag{2.9}$$

where $p_0 \approx 1000$ hPa is a reference pressure and c_p is the specific heat capacity at constant pressure. θ is conserved for adiabatic processes. For moist air, the virtual potential temperature is needed for a complete description given by

$$\theta_v \equiv T_v \left(\frac{p}{p_0} \right)^{-R/c_p}, \tag{2.10}$$

where $T_v = T(1 + 0.61q)$ is the virtual temperature and q is the specific humidity. Thus, equation (2.8) can be rewritten in terms of θ,

$$\frac{D\theta}{Dt} = \kappa_\theta \frac{\partial^2 \theta}{\partial x_i^2}. \tag{2.11}$$

If moisture is significant, θ_v can be substituted in equation (2.11). Concluding, equations (2.2), (2.3), (2.7), and (2.11) represent a complete set of general dynamic equations to describe stratified turbulent flows. The inherent turbulent nature of environmental flows and difficulty in solving these governing equations directly led to the historic field of *turbulence theory*. In the following section, basic turbulence theory is discussed and a working description is developed from which the research presented in this dissertation is based.

2.4. Mean Equations

Reynolds (1894) first proposed that a velocity field could be decomposed into mean and fluctuating components, termed *Reynolds decomposition*,

$$U(x,t) = \overline{U}(x,t) + u'(x,t), \tag{2.12}$$

where $U(x,t)$ is the instantaneous velocity field, $\overline{U}(x,t)$ is the time-averaged mean velocity field, and $u'(x,t)$ is the fluctuating velocity field. Similar decompositions can be made for p, ρ, and θ. Applying Reynolds decomposition to equation (2.3) assuming the validity of the Boussinesq approximation results in the Reynolds-averaged momentum equation written as

$$\frac{\bar{D}\overline{U}_j}{\bar{D}t} = \frac{\partial}{\partial x_i}\left[\nu\left(\frac{\partial \overline{U}_i}{\partial x_j} + \frac{\partial \overline{U}_j}{\partial x_i}\right) - \frac{1}{\rho}\overline{p}\delta_{ij} - \overline{u_i' u_j'}\right], \tag{2.13}$$

where $-\overline{p}\delta_{ij}$ is the isotropic stress from the mean pressure field and $-\overline{u_i' u_j'}$ is the turbulent momentum flux (or Reynolds stresses). The mean density and potential temperature equations applying Reynolds decomposition are then given by

$$\frac{\bar{D}\overline{\rho}}{\bar{D}t} = \frac{\partial}{\partial x_i}\left(\kappa_\rho \frac{\partial \overline{\rho}}{\partial x_i} - \overline{u_i'\rho'}\right), \tag{2.14}$$

$$\frac{\bar{D}\overline{\theta}}{\bar{D}t} = \frac{\partial}{\partial x_i}\left(\kappa_\theta \frac{\partial \overline{\theta}}{\partial x_i} - \overline{u_i'\theta'}\right), \tag{2.15}$$

where $-\overline{u_i'\rho'}$ are $-\overline{u_i'\theta'}$ are the turbulent density and potential temperature fluxes, respectively.

2.5. Flux-Gradient Hypotheses

As the result of Reynolds-averaging, the addition of the turbulent momentum, density, and potential temperature flux terms, $-\overline{u_i' u_j'}$, $-\overline{u_i'\rho'}$, and $-\overline{u_i'\theta'}$, results in an ill-posed set of equations. The flux-gradient hypotheses or relationships assume that the diffusive or viscous transport processes occur down-gradient and are described in the following subsections.

2.5.1. Turbulent-Viscosity Hypothesis. The *turbulent-viscosity hypothesis* states that the deviatoric Reynolds stresses are proportional to the mean rate of strain written as

$$-\overline{u_i' u_j'} = \nu_t \left(\frac{\partial \overline{U}_i}{\partial x_j} + \frac{\partial \overline{U}_j}{\partial x_i} \right) - \frac{2}{3} k \delta_{ij} \tag{2.16}$$

where $k = (1/2)\overline{u_i' u_i'}$ is the turbulent kinetic energy and ν_t is the eddy diffusivity of momentum (or eddy viscosity). Thus, substituting equation (2.16) into equation (2.13) results in the mean momentum equation given by

$$\frac{\bar{D}\overline{U}_j}{\bar{D}t} = \frac{\partial}{\partial x_i} \left[\nu_{\text{eff}} \left(\frac{\partial \overline{U}_i}{\partial x_j} + \frac{\partial \overline{U}_j}{\partial x_i} \right) \right] - \frac{1}{\rho} \frac{\partial}{\partial x_j} \left(\overline{p} + \frac{2}{3} \rho k \right), \tag{2.17}$$

where $\nu_{\text{eff}} = \nu_t + \nu$ is the effective eddy viscosity. Here, ν_t remains the only unknown variable which needs to be closed. Closure for ν_t, or turbulence closure, is further discussed in chapter 3.

2.5.2. Gradient-Diffusion Hypothesis. Similarly, the *gradient-diffusion hypothesis* for density and potential temperature is given by

$$-\overline{u_i' \rho'} = \kappa_{t_\rho} \frac{\partial \overline{\rho}}{\partial x_i}, \tag{2.18}$$

$$-\overline{u_i' \theta'} = \kappa_{t_\theta} \frac{\partial \overline{\theta}}{\partial x_i}, \tag{2.19}$$

where κ_{t_ρ} and κ_{t_θ} are the turbulent eddy diffusivities of density and potential temperature. For all intensive purposes, the eddy diffusivities for $\overline{\rho}$ and $\overline{\theta}$ are considered to be approximately equal and represented by κ_t ($\kappa_t \equiv \kappa_{t_\rho} \equiv \kappa_{t_\theta}$). Substituting equations (2.18) and (2.19) for the turbulent eddy diffusivities of density and potential temperature transport,

respectively, into equations (2.14) and (2.15) yields

$$\frac{\bar{D}\overline{\rho}}{\bar{D}t} = \frac{\partial}{\partial x_i}\left(\kappa_{\text{eff}}\frac{\partial\overline{\rho}}{\partial x_i}\right), \tag{2.20}$$

$$\frac{\bar{D}\overline{\theta}}{\bar{D}t} = \frac{\partial}{\partial x_i}\left(\kappa_{\text{eff}}\frac{\partial\overline{\theta}}{\partial x_i}\right), \tag{2.21}$$

where $\kappa_{\text{eff}} = \kappa_t + \kappa$ is the effective eddy diffusivity. Thus, for scalar transport, active or passive, in a turbulent flow, κ_t requires closure which is also addressed in chapter 3.

CHAPTER 3

Literature Review

3.1. Turbulence in Geophysical Flows

The majority of environmental or geophysical flows are classified as turbulent. Turbulence describes the seemingly random or chaotic motions which occur in conjunction with a mean flow. A substantial feature of turbulent flows is enhanced (or increased) mixing often quantified through the Reynolds number, $Re = \mathcal{UL}/\nu$ where $\mathcal{U}$ and $\mathcal{L}$ are characteristic velocity and length scales and ν is the kinematic viscosity, respectively. A complete and universal theory of turbulence remains elusive despite well over a century of research. Much of what is known about turbulence has resulted from theoretical and experimental studies pertaining to characteristic scales and the transfer of energy through these scales. Early theories relied on fundamental statistical descriptions:

(i). *Homogeneous turbulence* - properties are invariant with translation;

(ii). *Isotropic turbulence* - properties are invariant with rotation; and

(iii). *Stationary turbulence* - properties are invariant with time.

With these idealized conditions in mind, Richardson (1922) proposed a theory of turbulence wherein kinetic energy is generated at the large scales of motion and subsequently transferred through the inertial subrange and finally extinguished through viscous dissipation and the irreversible transfer to heat. This process is referred to as the *energy cascade* as depicted graphically in figure 3.1. From this perspective, Kolmogorov (1941) proposed a set of hypotheses stating that for active turbulent motions (e.g. $Re \gg 1$) (i) the kinematic viscosity and dissipation rate of turbulent kinetic energy, ν and ε, respectively, are unique parameters

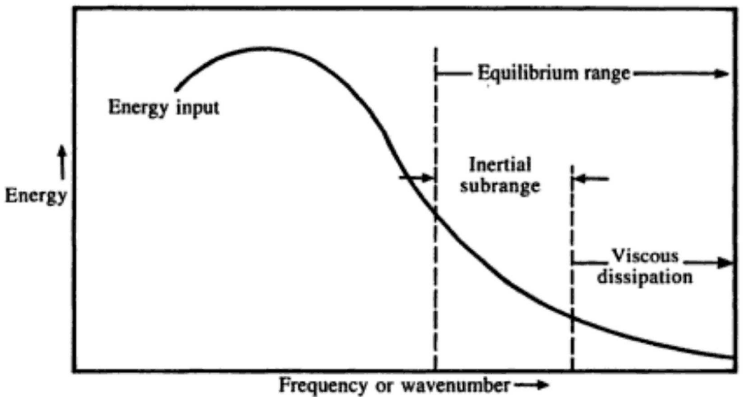

FIGURE 3.1. Schematic for the down-gradient energy spectrum of turbulence (figure 2.1 in Garratt, 1992).

and (ii) there exists an inertial subrange where the transfer of energy is dependent solely on ε. From these hypotheses, a set of length, velocity, and time scales pertaining to the smallest energy-containing scales (or Kolmogorov scales) of motion are given by

$$\eta = \left(\nu^3/\varepsilon\right)^{1/4}, \tag{3.1}$$

$$u_\eta = \left(\varepsilon\nu\right)^{1/4}, \tag{3.2}$$

$$\tau_\eta = \left(\nu/\varepsilon\right)^{1/2}. \tag{3.3}$$

Kolmogorov's theory of turbulence provides a framework by which turbulence can be described from resultant eddy interactions with mean flow as kinetic energy is transferred to the turbulent field at large-scales and dissipated through small-scale eddies (e.g. Wyngaard, 2010). Excellent reviews on fundamental turbulence theory and application are given by Monin and Yaglom (1971), Tennekes and Lumley (1972), Townsend (1976), Pope (2000), and Durbin and Pettersson Reif (2001).

The effective transport and mixing mechanisms in turbulent flows are governed by the large-scale motions. The largest isotropic eddies are described by the following velocity,

length, and time scales.

$$\mathcal{U} \equiv k^{1/2}, \tag{3.4}$$

$$\mathcal{L} \equiv \frac{k^{3/2}}{\varepsilon}, \tag{3.5}$$

$$\tau \equiv \frac{k}{\varepsilon}, \tag{3.6}$$

where $\mathcal{L}$ represents the largest active eddy size and τ is the time required to dissipate the amount of energy k at the rate ε. The representative Reynolds number is thus given by $Re = k^2/(\nu\varepsilon)$.

Turbulent processes are governed largely by the influences of velocity shear, stratification, and boundary effects. Deferring further discussion of stratification and boundary effects to later in this chapter, if shear influences are significant, inhomogeneities begin to present as well as anisotropy and the Reynolds (or apparent) stresses transfer momentum from the background flow to turbulent motions. If this transfer is directed counter-gradient to shear, mean kinetic energy is transfered to the flow disturbance resulting in the shear generation of turbulence, P, which is a dominant source of turbulence in geophysical flows (e.g. Smyth and Moum, 2000). Corrsin (1958) found that the largest survivable eddy for a turbulent shear flow is given by

$$L_C = \left(\frac{\varepsilon}{S^3}\right)^{1/2}, \tag{3.7}$$

where $S = \partial\overline{U}_i/\partial x_j$ is the mean shear rate. Here, survivable refers to an eddy that is unaffected by external influence. For example, an eddy with a representative length of $\mathcal{L} > L_C$ would likely be deformed by shear. For turbulent shear flows, P can be considered of equal significance to ε from which an analogous time scale can be constructed, $\tau_P \equiv k/P$. τ_P effectively describes the time required to generate the energy k at the rate P. Thus, for

active turbulence, τ and τ_P are approximately equal with their sum representing the lifespan of a turbulent eddy (Pope, 2000).

In highly turbulent geophysical flows, the large-scale motions responsible for transporting momentum, energy, and scalars have direct implications on many practical issues such as pollutant dispersion and global circulation (e.g. Tennekes and Lumley, 1972). The expansive scales of atmospheric and oceanic flows in conjunction with many external factors (e.g. mesoscale motions or topographic effects) adds further complexity to a study of turbulence. Geophysical turbulence has been and will continue to be a very active area of research as evident through numerous books, countless journal articles, and annual scientific meetings and conferences. Geophysical and environmental flows are characteristically different than most industrial or engineering flows of interest with time and length scales of turbulent motions larger by orders of magnitude.

To assess and study fundamental aspects of turbulent dynamics, numerous laboratory and numerical studies have been performed such as the works of Counihan (1969), Cermak (1971), Thorpe (1973), Hopfinger (1973), Lin and Veenhuizen (1974), and Willis and Deardorff (1974). Additionally, a thorough review of many seminal wind tunnel studies pertaining to boundary layer turbulence is given by Garratt (1990). Direct numerical simulation (DNS) studies have given valuable insights on physical processes in the ABL such as those by Coleman et al. (1990), Coleman et al. (1992), Miyashita et al. (2006), Schlatter et al. (2009), Marlatt et al. (2012), Garcia and Mellado (2012), and Deusebio et al. (2014). Given the relatively low Reynolds numbers in such experiments, some uncertainty exists in applying this knowledge to geophysical scales of turbulence (e.g. Riley and Lelong, 2000). Field measurements are useful in describing large-scale processes but cannot capture all of

the scales of turbulence due to instrumentation limitations, non-turbulent motions (e.g. internal gravity waves), and the stochastic nature of turbulence. Physical measurements of the atmosphere are obtained from fixed meteorological towers, aircraft, and tethered balloons and kites. A few of the earliest studies are discussed by Clarke et al. (1971) and Businger et al. (1971) from the Wangara and Kansas experiments, respectively. The extensive works of Stull (1988), Sorbjan (1989), and Garratt (1992) describe the many dynamic processes of turbulence, heat and mass transfer, solar radiation, soil physics, surface vegetation, and human interactions within the planetary boundary layer. Definitions of atmospheric turbulence generally assume a down-gradient transfer of energy and Reynolds-averaging to determine a statistically relevant averaging period about which to calculate fluctuations and fluxes. Stratification adds further complexity where even less is known about these flows and is discussed in the following section.

3.2. Stably Stratified Turbulence

In addition to being turbulent, most geophysical flows also experience stratification effects wherein density variations lead to the introduction of buoyancy forces. In a heterogeneous flow under stable flow conditions, a displaced fluid particle will oscillate about its equilibrium position over some distance η. This motion can be described by

$$\frac{\partial^2 \eta}{\partial t^2} = \frac{g}{\theta}\frac{\partial \theta_0}{\partial z}\eta. \tag{3.8}$$

The frequency of this oscillation is given by the buoyancy (or Brunt-Väisällä) frequency, $N = [(g/\theta_0)\partial\overline{\theta}/\partial z]^{1/2}$. In stable flow conditions, a displaced fluid parcel will return to its

equilibrium position through restorative gravitational and buoyancy forces limiting vertical velocity fluctuations. For a sheared flow, the gradient Richardson number, Ri, is an important stability parameter,

$$Ri = \frac{N^2}{S^2}. \tag{3.9}$$

For unstable stratification, a negative gradient in $\overline{\theta}$ yields $Ri < 0$ whereas stable stratification results in a positive gradient in $\overline{\theta}$ and $Ri > 0$. Another closely related parameter is the flux Richardson number, R_f, providing a ratio of turbulence destruction (or production) by buoyancy forces to production due to shear.

$$R_f = \frac{-B}{P}, \tag{3.10}$$

where $B = (g/\theta_0)\overline{u_i'\theta'}\delta_{i3}$ is the buoyant production of k (or buoyancy flux) and $P = -\overline{u_i'u_j'}(\partial\overline{U}_i/\partial x_j)$ is the shear production of k. Ri and R_f are local flow parameters for describing stable flow conditions.

Stable flow conditions lead to a characteristically different behavior of turbulence in the ABL and can be significantly more difficult to identify (Mahrt, 2014). Lilly (1983) originally coined the term *stably stratified turbulence* defining the unique interactions of turbulent and non-turbulent motions in the stably stratified atmosphere. First, it is necessary to reassess the relevant scales of stably stratified turbulence as buoyancy effects enter the picture. A common parameter is the buoyancy length scale given by

$$L_b \equiv \frac{\sigma_w}{N}, \tag{3.11}$$

where $\sigma_w = \overline{w'^2}^{1/2}$ is the root-mean-square (r.m.s) of the vertical velocity fluctuations. L_b provide a measure of the maximum vertical distance traveled by a fluid parcel with a given measure of buoyancy in N. In analogous form to the Corrsin scale (equation (3.7)), Dougherty (1961) and Ozmidov (1965) independently proposed the length scale commonly referred to as the Ozmidov scale

$$L_O \equiv \left(\frac{\varepsilon}{N^3}\right)^{1/2}, \tag{3.12}$$

defining the largest survivable eddy in a buoyancy-dominated flow.

As stability increases, the vertical perturbations and instabilities of three-dimensional turbulence are suppressed leading to a relaminarization of the flow or turbulence "collapse." Gibson (1980) described this process as the onset of fossilization. As stably stratified turbulence decays, quasi-horizontal, two-dimensional motions, or "pancake vortices" form that grow with time creating a layering effect in the flow (Lin and Pao, 1979; Spedding et al., 1996; Riley and deBruynKops, 2003) and also feed into the formation and propagation of internal gravity waves (e.g. Stewart, 1969). A longstanding question in the study of stably stratified turbulence is when does turbulence collapse and return to a laminar state? Richardson (1920) proposed that this transition occurs at $Ri \sim O(1)$. The hydrodynamic stability criterion for stationary, homogeneous conditions has been widely accepted for a critical gradient Richardson number, $Ri_c \approx 0.25$ (e.g. Miles, 1961; Howard, 1961). Turbulence collapse may also be assessed through a local Froude number, $Fr = \mathcal{U}/N\mathcal{L}$, as done in the laboratory experiments of Ivey and Corcos (1982) and Thorpe (1982). The review by Hopfinger (1987) assessed criterion based on the ratio of buoyancy to overturning length scales

$$\frac{L_b}{L_E} \equiv \frac{\sigma_w/N}{\theta'/(\partial\overline{\theta}/\partial z)} \qquad \text{or} \qquad \frac{L_O}{L_E} \equiv \frac{(\varepsilon/N^3)^{1/2}}{\theta'/(\partial\overline{\theta}/\partial z)}, \tag{3.13}$$

where L_E is the Ellison length scale (Ellison, 1957). L_E measures the active eddies or overturns according to the scalar field (e.g. θ). However, active mixing is more accurately described by the mixing length of the turbulent momentum field, L_M. The buoyancy Reynolds number, $Re_b \equiv \varepsilon/(\nu N^2)$, characterizes the energetics of a stably stratified flow and yields a rough estimate of the collapse (e.g. Hopfinger, 1987). In DNS experiments of channel flow, Nieuwstadt (2005) and Flores and Riley (2011) evaluated the ratio of channel height to the Obukhov length, (h/L), and non-dimensional Obukhov length, $L^+ = Lu_\tau/\nu$ whereas García-Villalba and del Álamo (2011) utilized a Nusselt number, $Nu = 2hq_w/(\kappa\Delta\rho)$. Clearly, many criteria exist for describing flow relaminarization for relatively low-Re scenarios.

As these quasi-horizontal, two-dimensional motions create a layering effect, local shear can lead to inflectional instabilities (or Kelvin-Helmholtz instabilities) which continue to grow leading to local production of three-dimensional turbulence (e.g. De Silva et al., 1996; Sun et al., 1998; Smyth and Moum, 2000). Lilly (1983) noted similar behavior in the atmosphere as layers decorrelate at high-Re. The breaking of internal waves also generates three-dimensional turbulence (e.g. Lombard and Riley, 1996; Lelong and Dunkerton, 1998). Bartello (1995) added that geophysical turbulence under strongly stable conditions exhibits scales not achieved in laboratory and favor a down-scale transfer of energy. Geophysical flows can exhibit stably stratified turbulence in intermittent bursts or in a continuous manner (e.g. Gregg, 1987; Mahrt, 2007) and likely always exists to some degree due to the coexistence of turbulent and non-turbulent motions. Mahrt (1989) distinguished between locally intermittent events and "global intermittency" where patches of eddies form. Atmospheric and oceanic flows also experience external forcing through meso- or submeso scale motions,

currents, gravity or drainage fronts, and surface effects. Thus, stably stratified geophysical turbulence is inherently a nonlinear stability problem.

Additionally, further turbulence modification occurs when the Earth's rotational effect is significant measured by the Rossby number, $Ro = \mathcal{U}/(f\mathcal{L}) < 1$. For instance, perturbations and instabilities can be further suppressed leading to the onset of additional inertial phenomena. For example, low-level jets are a unique feature of the SABL formed through a variety of mechanisms. Blackadar (1957) suggested that a force imbalance occurs as frictional drag along the Earth's surface decreases due to rising convective air currents that dissipate with surface cooling. As surface winds accelerate, a decoupling occurs between the inner and outer layers leading to an increased wind shear (see e.g. figure 3.2). The inner layer represents

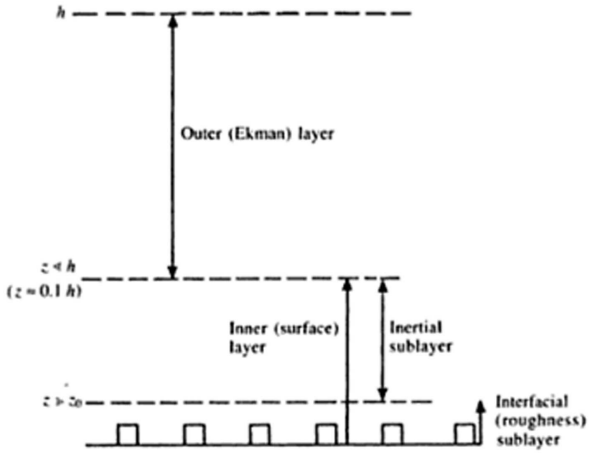

FIGURE 3.2. Schematic of the atmospheric boundary layer vertical structure for neutrally stratified flow conditions (figure 1.1 in Garratt, 1992).

the region were surface influences are prominent that diminish transitioning to the outer layer where rotational forces become important. The outer layer is also referred to as the Ekman layer (Ekman, 1905). Additionally, over vast expanses such as the Great Plains in the United States, the Coriolis force causes a turn (rightward in the northern hemisphere) in the mean velocity. An inertial oscillation forms with a period of $\pi/(\Omega \sin\phi)$, where Ω is the

Earth's rotation rate and ϕ is latitude, when aligned with the mean wind speed results in an apparent speed (Kelley et al., 2004). Furthermore, jets may also result purely from density currents (e.g., thunderstorm gust fronts and drainage-flow fronts) resulting in a cold-air layer behind the front (Bowen, 1996; Whiteman et al., 1997). The additional shear in the region of these jets may enhance the formation of internal waves (e.g. Blumen et al., 2001; Mahrt and Vickers, 2002; Newsom and Banta, 2003; Sun et al., 2004).

3.3. Parameterizations of Turbulence

DNS of turbulent geophysical flows remains impossible due to computational requirements. Practical numerical models must have computational time less than real time to provide predictive capabilities in forecasting applications such as national weather prediction (NWP) or global circulation models. To circumvent the computational requirements of DNS, large-eddy simulation (LES) techniques were developed from a need to provide time-dependent predictions by the meteorological research community. LES resolves the large-scale eddies and parameterizes smaller scale motions allowing for simulation of realistic flow conditions (e.g. Moeng and Wyngaard, 1984; Mason and Thomson, 1987; Mason and Derbyshire, 1990; Andrén et al., 1994; Moeng and Sullivan, 1994; Kosović, 1997; Porté-Agel et al., 2000; Kosović and Curry, 2000). While care must be taken in prescribing sub-grid scale (SGS) models governing the amount of mixing transfered to the resolved scales, LES is advantageous in many practical modeling applications assuming the availability of sufficient computational resources. Yet, in many instances Reynolds-averaged techniques are preferable due to computational efficiency and are employed in many operational and research models. Model predictions of stably stratified turbulence in the planetary boundary layer

remain rather poor warranting further investigation (e.g. Viterbo et al., 1999). As stratification increases, turbulence also becomes decoupled from the surface (Mahrt, 1999) and similarity theory does not hold warranting local parameterizations of turbulent mixing.

The generalized flux-gradient relationships for a horizontally-homogeneous flow are written as

$$-\overline{u'w'} = K_M \frac{\partial \overline{u}}{\partial z}, \tag{3.14}$$

$$-\overline{v'w'} = K_M \frac{\partial \overline{v}}{\partial z}, \tag{3.15}$$

$$-\overline{w'\theta'} = K_H \frac{\partial \overline{\theta}}{\partial z}, \tag{3.16}$$

$$-\overline{w'q'} = K_Q \frac{\partial \overline{Q}}{\partial z}, \tag{3.17}$$

where K_M is the eddy diffusivity of momentum (or eddy viscosity, ν_t), K_H is the eddy diffusivity of heat, K_Q is the eddy diffusivity of specific humidity, q' is the fluctuating component of specific humidity, and $\overline{Q}$ is the average specific humidity. K_H and K_Q are approximately equal, $K_H \approx K_Q$, and generically termed the eddy diffusivity, κ_t. Dimensional analysis reveals the eddy viscosity, ν_t, may be represented through an appropriate combination of velocity and length scales, $\nu_t \sim u^* l^*$, or length and time scales, $\nu_t \sim l^{*2} t^{*-1}$. In what follows, existing zero-, one-, and two-equation turbulence closure schemes (or Reynolds-Averaged Navier-Stokes, RANS) with application to the ABL are discussed. Given the countless number of models in literature with varying degrees of empiricism, the following review focuses on key aspects of respective model parameterizations. Higher-order closures (e.g. Reynolds-stress models) have been used sparingly in geophysical applications due to the high computational costs and are not discussed further in this chapter.

3.3.1. Parameterizations of Eddy Viscosity.

3.3.1.1. *Zero-Equation Turbulence Closure and Similarity Theory.* Zero-equation closures solve for the eddy viscosity from obtainable meteorological or model parameters. Prandtl (1925) suggested that the velocity scale of turbulence is proportional to the product of the mixing length and mean shear rate, $u^* \sim l_m S$. Thus, the eddy viscosity for zero-equation closure is given by

$$\nu_t = l_m^2 S. \tag{3.18}$$

Prandtl's mixing length hypothesis implies that the turbulent mixing length varies proportionally with the distance from a surface or boundary, $l_m = \kappa z$ where $\kappa \approx 0.39 - 0.43$ is the von Kármán constant.

From this hypothesis, Monin and Obukhov (1954) proposed a similarity theory to describe the effects of stratification on mean profiles of velocity and temperature within the surface or constant-flux layer. Foken (2006) provides an excellent review of Monin-Obukhov similarity theory from early development to its current state in the meteorological community. The relevant parameters are taken to be shear velocity, height, buoyancy parameter, and surface heat flux, u_*, z, g/θ_0, and $(\overline{w'\theta'})_0$, respectively. Within this dynamic sublayer, Obukhov (1946) suggested the characteristic length scale, or Obukhov length, written here in the modern form

$$L = -\frac{u_*^3 \theta_0}{\kappa g \left(\overline{w'\theta'}\right)_0}. \tag{3.19}$$

Dimensionless groupings can then be cast for the velocity and temperature gradients written as

$$\frac{\kappa z}{u_*}\left(\frac{\partial \overline{U}}{\partial z}\right) = \Phi_M(\zeta), \tag{3.20}$$

$$\frac{\kappa z}{\theta_*}\left(\frac{\partial \overline{\theta}}{\partial z}\right) = \Phi_\theta(\zeta), \tag{3.21}$$

where $\overline{U}$ is the mean horizontal velocity, Φ_M is the momentum stability function, $\zeta = z/L$ is the non-dimensional height parameter, $\theta_* = |\overline{w'\theta'}_0|/u_*$ is the shear potential temperature scale, and Φ_H is the thermodynamic stability function. While early works assumed the stability functions were equal, $\Phi_M \approx \Phi_H$, they are more frequently associated with the form proposed by Businger et al. (1971),

$$\Phi_M(\zeta) = \begin{cases} (1-\gamma_1\zeta)^{-\frac{1}{4}}, & -2 < \zeta < 0 \quad \text{(unstable)} \\ 1+\beta\zeta, & 0 \le \zeta < 1 \quad \text{(stable)} \end{cases}, \tag{3.22}$$

$$\Phi_H(\zeta) = \begin{cases} Pr_t\,(1-\gamma_2\zeta)^{-\frac{1}{2}}, & -2 < \zeta < 0 \quad \text{(unstable)} \\ Pr_t + \beta\zeta, & 0 \le \zeta < 1 \quad \text{(stable)} \end{cases}, \tag{3.23}$$

where $Pr_t = 1$ is the turbulent Prandtl number, $\beta = 5$ is coefficient of thermal expansion, and $\gamma_1 = \gamma_2 = 16$ are empirical constants following Dyer (1974). For neutral and stable stratification when pressure perturbations are inconsequential to the transport of momentum, equations (3.22) and (3.23) imply that $\Phi_M \approx \Phi_H$. The modified velocity and temperature profiles are obtained from integration of equations (3.22) and (3.23) with respect to z yielding

$$\overline{U}(z) = \frac{u_*}{\kappa}\left[\log\left(\frac{z}{z_0}\right) - \Psi_M(\zeta)\right], \tag{3.24}$$

$$\overline{\theta}(z) = \theta_0 - \frac{\theta_*}{\kappa}\left[\log\left(\frac{z}{z_\theta}\right) - \Psi_H\left(\zeta\right)\right], \tag{3.25}$$

where z_0 is the aerodynamic roughness height and Ψ_M and Ψ_H are the momentum and thermodynamic profile correction functions given in equations (3.26) and (3.27), respectively.

$$\Psi_M\left(\zeta\right) = \begin{cases} \log\left[\left(\frac{1+x^2}{2}\right)\left(\frac{1+x}{2}\right)^2 2\right] - 2\tan^{-1}x + \frac{\pi}{2}, & -2 < \zeta < 0 \quad \text{(unstable)} \\ -\beta\zeta, & 0 \leq \zeta < 1 \quad \text{(stable)} \end{cases}, \tag{3.26}$$

$$\Psi_H\left(\zeta\right) = \begin{cases} 2\log\left(\frac{1+x^2}{2}\right), & -2 < \zeta < 0 \quad \text{(unstable)} \\ -\beta\zeta, & 0 \leq \zeta < 1 \quad \text{(stable)} \end{cases}, \tag{3.27}$$

where $x = (1 - \gamma_1\zeta)^{1/4}$. While Monin-Obukhov similarity theory performs well under weak stability in the surface layer, it does not hold for strongly stable stratification (see e.g. Klipp and Mahrt, 2004; Cheng and Brutsaert, 2005; Grachev et al., 2005, 2013, and references therein)

Nieuwstadt (1984) presented a local similarity theory redefining parameters locally rather than at the surface. For steady-state, the dimensionless turbulent momentum and temperature flux profiles were found to be

$$\frac{\tau}{u_*^2} = \left(1 - \frac{z}{h}\right)^{3/2}, \tag{3.28}$$

$$\frac{\overline{w'\theta'}}{\overline{w'\theta'}_0} = 1 - \frac{z}{h}, \tag{3.29}$$

where $\tau = (|\overline{u'w'}|^2 + |\overline{v'w'}|^2)^{1/2}$ are the turbulent momentum fluxes and h is the boundary layer height. Zilitinkevich (1972) proposed the boundary layer height approximation

$$h = c(u_* L/f)^{1/2}, \tag{3.30}$$

where $c^2 = \sqrt{3}\kappa R_f$ assuming a constant R_f over the extent of h. From these relationships, Holtslag and Nieuwstadt (1986) proposed the following zero-equation model for eddy viscosity which remains prominent in the numerical modeling community,

$$\nu_t = \frac{u_* \kappa z \left(1 - z/h\right)^2}{1 + \beta z/L}, \tag{3.31}$$

Despite the simplicity, this equation predicts ν_t remarkably well even when compared with high fidelity DNS results (e.g. Deusebio et al., 2014). However, Derbyshire (1990) notes that Nieuwstadt's theory does not address boundary conditions, steady-state conditions, internal waves, or model consistency in variable stability limits. Internal wave activity varies geographically and cannot be negated. Derbyshire (1990) extends Nieuwstadt's model for near-neutral and moderately stable regimes. This extended analytical model is often the basis for comparisons with numerical models and experimental data. Monin-Obukhov similarity theory and Nieuwstadt's local similarity remain prominent closures with renewed interest in recent years. Holt and Raman (1988) provided a review of other early K-theory model closures. Additional gradient-based scaling theories have been proposed by Sorbjan (2006), Sorbjan and Balsley (2008), Sorbjan and Grachev (2010), and Grachev et al. (2014).

Transitioning back to a traditional view of zero-equation models with the added knowledge of the Obukhov length, L, and its relevancy to the SABL, Blackadar (1962) proposed that the mixing length of the turbulent momentum field reaches a maximum size some finite distance away from the surface given by

$$l_m = \left(\frac{1}{\kappa z} + \frac{1}{\lambda}\right)^{-1}, \tag{3.32}$$

where $\lambda = 2.7 \times 10^{-4}|G|/|f|$ is the maximum mixing length, G is the geostropic wind, and f is the Coriolis parameter. Traditionally, λ was taken to be a constant $O(10^2)$ (Cuxart et al., 2006) but recent studies have suggested λ of $O(10^1)$ is more appropriate (e.g. Kim and Mahrt, 1992; Sun, 2011; Sorbjan, 2012; Huang et al., 2013). Delage (1974) furthered Blackadar's original form by incorporating a stability parameter to dampen the mixing length at strong stability,

$$l_m = \left(\frac{1}{\kappa z} + \frac{1}{\lambda} + \frac{\beta}{\kappa L} \right)^{-1}. \tag{3.33}$$

Although appealing in their simplicity, the algebraic closures inherent in zero-equation models rely heavily on empirical model constants and lack description of additional turbulent parameters.

3.3.1.2. *One-Equation Turbulence Closure.* In one-equation closure, the velocity scale is most commonly assumed to scale with the turbulence kinetic energy $u^* \sim k^{1/2}$. A mean equation for k with the Boussinesq approximation is written as

$$\frac{\bar{D}k}{\bar{D}t} = -\overline{u_i' u_j'} \frac{\partial \overline{U}_i}{\partial x_j} + \frac{g}{\theta_0} \overline{u_i' \theta'} \delta_{i3} - \frac{\partial (\overline{u_i' k})}{\partial x_i} - \frac{1}{\theta_0} \frac{\partial (\overline{u_i' p'})}{\partial x_i} - \varepsilon, \tag{3.34}$$

where $-\partial(\overline{u_i' k})/\partial x_i$ is the transport of k, $-(1/\theta_0)\partial(\overline{u_i' p'})/\partial x_i$ is the pressure transport of k, and $\varepsilon = \nu \overline{(\partial u_i'/\partial x_j)(\partial u_j'/\partial x_i)}$ is the molecular (or viscous) dissipation of k. Generally, the pressure transport term is found to be insignificant compared to other terms. Equation (3.34) can be simplified for homogeneous stratified conditions as

$$\frac{\partial k}{\partial t} = \frac{\partial}{\partial z} \left(\frac{\nu_t}{\sigma_k} \frac{\partial k}{\partial z} \right) + P + B - \varepsilon, \tag{3.35}$$

where $\sigma_k = 1.3$ is the turbulent Prandtl number for turbulent kinetic energy. The eddy viscosity is now written as

$$\nu_t \sim c l_m k^{1/2}, \tag{3.36}$$

where c is an empirical model constant defined by $c^2 = |\overline{u_i' u_j'}|/k$ known as the stress-intensity ratio. From early laboratory experiments $c^2 \approx 0.3$ has been widely considered to be universally constant. However, recent studies of high-Re flows suggest that $c^2 \approx 0.25$ may in fact be more accurate in highly turbulence conditions (Marušic and Perry, 1995; Hoyas and Jiménez, 2006). Karimpour and Venayagamoorthy (2014a) observed that $c^2 \approx 0.25$ appears to be an asymptotic limit for high-Re. Nieuwstadt (1984) observed that $c^2 \approx 0.22 - 0.27$ remains approximately constant in the ABL near neutral stability. Mauritsen et al. (2007) observed that c^2 decreases with increasing stability (e.g. Ri) for the SABL.

Here it is now possible to discuss more physically relevant lengths scales with a prognostic equation for k. Thorough reviews of historical and operational one-equation model closures are given by Holt and Raman (1988) and Cuxart et al. (2006). Numerous models utilize a form of Blackadar (1962), equation (3.32), or Delage (1974), equation (3.33). For k-equation closure, Duynkerke and Driedonks (1987) proposed a mixing length given by the minimum between

$$l_N = c_s \frac{k^{1/2}}{N}, \tag{3.37}$$

and

$$l_B = \left(\frac{\Phi_M}{\kappa z} + \frac{1}{\lambda} \right)^{-1}, \tag{3.38}$$

such that $l_m = \min(l_N, l_B)$. Weng and Taylor (2003) and Weng and Taylor (2006) revisited one-equation closure where l_m is defined similarly to Duynkerke and Driedonks (1987). An

algebraic formula for ε is given by

$$\varepsilon = \frac{(\alpha k)^{3/2}}{l_\varepsilon}, \tag{3.39}$$

where $\alpha \approx c^2$ is an empirical constant and l_ε is the dissipation length scale define using a modified for of equation (3.33) written as

$$l_\varepsilon = \left(\frac{1}{\kappa z} + \frac{1}{\lambda} + \frac{\beta - 1}{\kappa L} \right)^{-1}. \tag{3.40}$$

Operational single-column models utilize one-equation closure to solve for the eddy viscosity within the boundary layer to provide a turbulence mixing length in the upper atmosphere.

3.3.1.3. *Two-Equation Turbulence Closure.* Two-equation closure models increase in sophistication through an additional prognostic equation for a relevant turbulent parameter. Two popular models used in geophysical applications are the k-ε model (Jones and Launder, 1972; Launder and Spalding, 1974) and the q^2-l model of (Mellor and Yamada, 1982) where $q^2 \sim 2k$. The q^2-l model remains prominent in many operational national weather prediction and climate models including the weather research and forecasting (WRF) model. On the other hand, the k-ε model is perhaps most widely used RANS model in engineering applications and will be the focus of this section.

Early simulations of geophysical flows using the k-ε model were performed by Lee and Kao (1979) for the atmosphere and Marchuk et al. (1977) and Svensson (1979) for the ocean. For the standard k-ε a prognostic ε can be written as

$$\frac{\partial \varepsilon}{\partial t} = \frac{\partial}{\partial z} \left(\frac{\nu_t}{\sigma_\varepsilon} \frac{\partial \varepsilon}{\partial z} \right) + C_{\varepsilon 1} \frac{\varepsilon}{k} P + C_{\varepsilon 3} \frac{\varepsilon}{k} B - C_{\varepsilon 2} \frac{\varepsilon^2}{k}. \tag{3.41}$$

where $\sigma_k = 1.0$, $\sigma_\varepsilon = 1.3$, $C_{\varepsilon 1} = 1.44$, and $C_{\varepsilon 2} = 1.92$ are the standard set of model equations (Launder and Spalding, 1974). The standard eddy viscosity is $\nu_t = C_\mu k^2/\varepsilon$ where C_μ is the square of the stress-intensity ratio, c^4. $C_\mu = 0.09$ is the calibrated constant based on $c^2 \approx 0.3$. The k-ε model is most sensitive to the value of C_μ (Apsley and Castro, 1997). C_μ is also believed to vary with stability (e.g. Freedman and Jacobson, 2003), where for the equilibrium assumption in a stratified flow, the dominant balance in equation (3.35) is $P + B = \varepsilon$. Thus, from $R_f = -B/P$, C_μ is effectively reduced by $(1 - R_f)$ such that the modified eddy viscosity is given by

$$\nu_t = (1 - R_f) C_\mu \frac{k^2}{\varepsilon}. \tag{3.42}$$

In modeling applications of the SABL, equation (3.42) is insufficient to capture all of the dynamic effects of stratified turbulence. As discussed by Mason and Sykes (1980) and Detering and Etling (1985), the standard k-ε model produces a very deep boundary layer over-predicting eddy viscosity and friction velocity. Rodi (1980) suggested that the model constants are not necessarily universal in parameterizing turbulent momentum, heat, and specific humidity fluxes. Many expanded or modified sets of empirical model constants have been also suggested (e.g. Panofsky et al., 1977).

Apsley and Castro (1997) attributed the shortcomings of the k-ε model to an over-prediction of the mixing length, $l_m \sim k^{3/2}/\varepsilon$, and assigned an upper limit according to equation (3.32) (Blackadar, 1962). The *production of dissipation* term is then modified according to $C'_{\varepsilon 1} = C_{\varepsilon 1}\,(l_m/\gamma h)$ where $\gamma = 0.0075$ is an empirical constant. Sumner and Masson (2012) revisited Apsley and Castro's modifications to further develop a length-limited k-ε model consistent with Monin-Obukhov similarity theory. The value of $C_{\varepsilon 3}$ for the *buoyancy*

production of dissipation is another area of contention in modeling stable flow conditions with k-ε closure with a range of 0–0.2 proposed by Rodi (1987). Burchard and Baumert (1995) suggested that $C_{\varepsilon 3}$ may in fact be a negative value. A comprehensive review of $C_{\varepsilon 3}$ constant values is presented by Baumert and Peters (2000). Additionally, stability-dependent functions of $C_{\varepsilon 3}$ have been explored by Freedman and Jacobson (2003), Alinot and Masson (2005), and Sumner and Masson (2012).

3.3.2. The Turbulent Prandtl Number. In the Reynolds-averaged framework, the eddy diffusivity, κ_t, is determined using the turbulent Prandtl number, $Pr_t \equiv \nu_t/\kappa_t$. For simple flows Pr_t is approximately unity (Pope, 2000) with a general range of 0.5–1 for unstratified turbulent flows (e.g. Kays, 1994). Under stable flow conditions it is thought that Pr_t is an increasing function of stability (Munk and Anderson, 1948; Kondo et al., 1978; Gerz et al., 1989; Beljaars and Holtslag, 1991; Holt et al., 1992; Strang and Fernando, 2001; Kim and Mahrt, 1992; Schumann and Gerz, 1995; Shih et al., 2000; Zilitinkevich and Baklanov, 2002; Venayagamoorthy and Stretch, 2010). At high stability, scalar transport is much less efficient than momentum transport. In the SABL, this behavior is possibly linked to pressure perturbations caused by turbulence and internal waves motions at high stability (Mahrt, 1998). Accurate scalar mixing remains a challenge in numerical modeling of stably stratified wall-bounded flows with no definitive solution. It is quite possible there remains an unexplored linkage between Pr_t and flow energetics.

3.4. Implications on Wind Energy

Inertial phenomena in the SABL such as internal wave motions, bursts of three-dimensional turbulence, and low-level jets have a significant impact on wind turbine fatigue and failures (e.g. Zhou and Chow, 2012). The representation of such phenomena inherently rely on the

modeling framework (e.g. LES or RANS) and the physical extent of the computational domain. As wind turbine sizes continue to increase and reach high into the atmosphere, strong shear and fluctuating loads are likely to impact the longevity of composite blade materials. Fluctuations may also be enhanced through wake meandering from upstream turbines in wind farms (Högström et al., 1988; Vermeer et al., 2003). To analyze the effects and interactions of boundary layer dynamics and wind turbines, accurate computational models of horizontal wind turbines are required.

3.4.1. Wind Turbine Models. At a basic level, a wind turbine is a device for extracting momentum and kinetic energy from wind and converting it to electrical energy. The lift along the blades surfaces transforms streamwise momentum to torque converted to electrical energy by the generator. Representation of wind turbines in CFD models vary in sophistication commonly represented through actuator disk (ADM), actuator line (ALM), and full rotor (FRM) models. Actuator disk and line models are generally used to determine the influence of a wind turbine on the ABL extending blade element momentum (BEM) theory (Burton et al., 2001) while full rotor models determine loads on turbine structures and power production (Vermeer et al., 2003). The following sections further discuss these individual models.

3.4.1.1. *Actuator Disk Model.* The basis for the actuator disk model is the distribution of typical wind turbine body forces over a volume in the computational domain rather than the actual rotor geometry. This allows for a computational model without the need for a highly resolved mesh in the region of the rotor to accurately capture the boundary layer effects along the blades. An actuator disk usually induces a velocity variation (Burton et al., 2001). Development of actuator disk methods are further described by Sørensen and

Myken (1992), Sørensen and Kock (1995), Madsen (1996), and Mikkelsen (2003). These formulations generally do not depict the turbine nacelle or tower. The effects of rotation can also be accounted for using a rotating implementation (e.g. Porté-Agel et al., 2011)

3.4.1.2. *Actuator Line Model.* The largest limitation of the actuator disk methodology is the uniform force distribution in the tangential direction. In reality, the thrust and axial forces decay radially from the hub. The influence of the blade shape and orientation can be resolved as an integrated quantity in the azimuthal direction. Sørensen and Shen (2002) developed a three-dimensional actuator line model which accounts for these mentioned effects in addition to rotation and the subsequent induction of tip vortices. Actuator line model studies have been performed by Porté-Agel et al. (2011), Wu and Porté-Agel (2011), and Churchfield et al. (2012a) with a noticeable improvement in accuracy without the added computation costs associated with full three-dimensional rotor models.

3.4.1.3. *Full Rotor Turbine Model.* Full rotor models consist of explicit three-dimensional rotor and blades surfaces which are rotated in the flow domain. Rotation is achieved through either multiple reference frames or sliding mesh surfaces. These models require a mesh resolution adequately sized to capture the boundary layer effects on the turbine blade surfaces. The fine grid requirements result in a model that is computationally expensive and does not significantly improve far wake resolution.

3.4.2. Wind Farm Models and Further Implications. Due to computational requirements for simulating wind turbine dynamics in addition to the complexities of the ABL, LES studies remain rather limited (e.g. Calaf et al., 2010; Lu and Porté-Agel, 2011; Porté-Agel et al., 2011; Churchfield et al., 2012a) with more prevalent studies of RANS models (e.g. Xu and Sankar, 2000; Alinot and Masson, 2002; Sørensen and Shen, 2002; Gómez-Elvira

et al., 2005; Kasmi and Masson, 2008). Simulation accuracy of single and multiple turbine arrays depends on a variety of factors including turbulence parameterizations and the sophistication of turbine models. Despite advances in computational resources and model accuracy in recent years, many large-scale wind farm models rely on methods other than computational fluid dynamics. For example, Frandsen et al. (2006) proposed an empirical model including turbulence and wake effects. Other models represent turbines as simple drag-disks or apply an empirical wake model within the context of a RANS model of the ABL.

Furthermore, as the horizontal extent of wind farms continues to grow, wind turbines act as roughness elements creating a "wind-farm-induced ABL" (e.g. Frandsen, 1992; Finnigan and Belcher, 2004; Frandsen et al., 2006). Meyers and Meneveau (2012) noted that power output and thrust of individual turbines can become parameters of turbine spacing and loading than of the incident wind field. An outstanding question is what are the broader impacts of wind turbines on atmospheric processes? Fitch et al. (2013a) evaluated the mesoscale influences of wind farms observing similar modification to the ABL in addition to changes in turbulent kinetic energy and surface fluxes. Recently, weather forecasting models have been coupled with LES wind farm models opening an avenue to explore global impacts of wind farms (Fitch et al., 2013b; Aitken et al., 2014; Mirocha et al., 2014). Of course, global influences of wind turbines must be evaluated in the light of their importance in relation to diminishing natural resources, air pollution, and climate change.

3.5. Summary

The literature review presented in this chapter covers a broad spectrum of topics. The intent of this presentation is to provide a trajectory for the research presented in the following chapters.

- Stably stratified turbulence has traditionally been studied through either small-scale laboratory and numerical experiments or observational studies of oceanic and atmospheric flows. Universality of stratified turbulent theories has long been assumed by scaling independent of the Reynolds number. A holistic analysis of an ensemble data of stably stratified turbulence is needed to further evaluate current and future parameterizations.
- Countless turbulence closure models have been proposed for evaluation of the stably stratified atmospheric boundary layer without consensus upon a singular framework or level of accuracy. Additionally, many closure schemes were developed from relatively low-Re flows warranting a top-down approach to parameterization beginning with geophysical flows.
- Numerical modeling of stably stratified turbulence often rely on a myriad of stability and/or damping functions which can be fundamentally- or empirically-based. A capable model must be able to capture dynamic effects irrespective of Re effects.
- Refocusing towards an engineering perspective of wind energy, numerical models must capture relevant physics in a timely manner. Computational wind turbine models require model capabilities not necessary in simulations of the planetary boundary layer.

CHAPTER 4

An Analysis of Turbulent Mixing in Strongly Stably Stratified Flows[1]

4.1. Introduction

An outstanding question in the study of stably stratified turbulence is what are the dynamics of turbulent mixing under strongly stable flow conditions? This question likely provokes many more questions than definitive answers. Undoubtedly, stable stratification affects mixing processes pertinent to global issues of air and water quality and climate change often assessed through predictive models. The Reynolds-averaged framework is prominent in many practical applications and relies on fundamental knowledge of stably stratified turbulence garnered from laboratory experiments, numerical simulations, and field observations discussed in the thorough reviews of Gregg (1987), Riley and Lelong (2000), Peltier and Caufield (2003), Ivey et al. (2008), and Mahrt (2014).

As stability increases, buoyancy forces suppress vertical perturbations and turbulence tends to a fossilized and quasi-two-dimensional state (Gibson, 1980). A common notion is that turbulence "collapse" occurs at a critical value of the gradient Richardson number, $Ri_c \sim O(1)$ (e.g. Miles, 1961; Howard, 1961). Extensive laboratory experiments (Stillinger et al., 1983; Itsweire et al., 1986; Rohr et al., 1988) and direct numerical simulation (DNS) (Gerz et al., 1989; Holt et al., 1992; Itsweire et al., 1993) have been performed to investigate stably stratified turbulence phenomena. At strong stability (e.g. high-Ri), quasi-horizontal scales, or so-called "pancake" vortices, create a layering effect that expand with time (Lin and

[1]The research presented in this chapter represents a manuscript in preparation for submission to a peer-reviewed journal. The chapter is written in a collective "we" to acknowledge collaboration with co-author, Dr. Subhas K. Venayagamoorthy.

Pao, 1979). The kinetic energy relinquished from the breakdown of large-scale eddies can lead to the formation and propagation of inertial waves motions or be mixed irreversibly through transference to background potential energy. Inter-facial shear can lead to instabilities and injections of turbulence from shear generation of turbulent kinetic energy (TKE) through internal intermittency (e.g. Turner, 1973). However, the Reynolds number, Re, in laboratory and numerical studies is relatively low with limited external forcing.

Stably stratified turbulence in geophysical flows is characteristically different from laboratory and numerical scales and universal theories rarely hold for both cases (Mahrt, 2014). An outstanding question that remains is whether strong mixing can be sustained under strongly stable flow conditions? Lilly (1983) suggested that quasi-horizontal layers in the atmosphere are likely to decouple causing shear instabilities and injections of three-dimensional turbulence. While the large-scale modification of stratified turbulence by these small-scale events remains an open question, Riley and Lindborg (2008) suggested that a down-scale transfer of energy through smaller-scale instabilities and turbulence could lead to avenues not traditionally seen in laboratory or numerical experiments. However, geophysical flows cannot be viewed through a traditional lens in that turbulence, to some degree, almost never ceases to exist even under strongly stable flow conditions. Internal wave motions coexist with non-linear quasi-horizontal motions leading to highly energetic bursts of three-dimensional turbulence (Gibson, 1999). Internal and external forces (e.g. mesoscale motion or currents) play roles in the sustenance of turbulence at high Ri which can be exhibited by intermittent or continuous states (Mahrt, 2007). Such observations in the stable atmospheric boundary layer (SABL) have led to the supposition that no Ri_c exists from an energetics standpoint

(e.g. Galperin et al., 2007). A primary objective of this chapter is to investigate stably stratified turbulence in low- and high-Reynolds number flows. We therefore believe it is instructive to address this issue through an in-depth analysis of DNS and laboratory experiments and high quality observational data of the stable atmospheric boundary layer (SABL).

In what follows, we discuss relevant descriptive parameters of stably stratified turbulence in section 4.2. In section 4.3, we present a comparative analysis of selected existing data sets highlighting the contrasting behavior of DNS and laboratory studies and strongly energetic SABL observations. Conclusions are given in section 4.4.

4.2. Background

4.2.1. Relevant Parameters. To begin, we consider the fundamental parameters of homogeneous turbulence given by the turbulent kinetic energy, $k = (1/2)\overline{u_i' u_i'}$, turbulent kinetic energy dissipation rate, $\varepsilon = \nu\overline{(\partial u_i'/\partial x_j)(\partial u_j'/\partial x_i)}$, kinematic viscosity, ν, and kinematic diffusivity κ. Large-scale motions can be described by relevant velocity, $u \sim k^{1/2}$, length, $l \sim k^{3/2}/\varepsilon$, and time, $\tau \sim k/\varepsilon$, scales representing the largest motions of isotropic turbulence. A characteristic turbulent Reynolds number is given by $Re = k^2/(\nu\varepsilon)$. For stably stratified shear turbulence, additional parameters are introduced through the mean shear rate, $S = \partial\overline{U}_i/\partial x_j$ and the Brunt-Väisällä (or buoyancy) frequency, $N = [(g/\theta_0)(\partial\overline{\theta}/\partial z)]^{1/2}$. S and N effectively represent inverse time scales of shear and buoyancy effects. The relationship between buoyancy and shear is generally assessed through the gradient Richardson number, $Ri = N^2/S^2$, or the flux Richardson number, $R_f = -B/P$ where $B = (g/\theta_0)\overline{w'\theta'}$ is destruction of k by buoyancy for stable stratification and $P = -\overline{u_i' u_j'}(\partial\overline{U}_i/\partial x_j)$ is the shear generation of k. Flow energetics in stable conditions can also be posed in the form

of a turbulent Froude number, $Fr = \varepsilon/(kN)$ (e.g. Ivey and Imberger, 1991), or buoyancy Reynolds number, $Re_b = \varepsilon/(\nu N^2)$ (e.g. Shih et al., 2005).

Considering that the large-scale turbulent motions in a stably stratified shear flow are of primary importance, we revise the turbulent Reynolds number to $Re_P = k^2/(\nu P)$ where P is of more relevance than ε. A relevant time scale is then given by $T_P \equiv k/P$ and the relative influence of buoyancy and shear are encapsulated in the buoyancy parameter, NT_P, and shear parameter, ST_P. We can develop two additional energetic parameters which we will term the shear-production Reynolds numbers,

$$Re_{SP} \equiv \frac{\nu_t}{\nu} = \frac{P}{\nu S^2} = Re_P \left(ST_P\right)^{-2}, \tag{4.1}$$

and the buoyancy-production Reynolds number,

$$Re_{NP} \equiv \frac{\nu_t}{\nu}\frac{S^2}{N^2} = \frac{P}{\nu N^2} = Re_P \left(NT_P\right)^{-2}, \tag{4.2}$$

where $\nu_t = -\overline{u_i' u_j'}/(\partial \overline{U}_i/\partial x_j)$ is the eddy (or turbulent) viscosity. Re_{SP} can also be thought of as the non-dimensionalized eddy viscosity relating turbulent mixing to kinematic viscosity. Re_{NP} is an analogous parameter given by $Re_{SP}Ri^{-1}$ and $Re_{SP} \approx Re_{NP}$ when $Ri \approx 1$. From this dimensionless parameter set, we can evaluate the large-scale motions of active turbulence in stably stratified flow conditions.

4.3. Analysis/Results

We analyze several existing high-quality laboratory, numerical, and observational data sets of stably stratified shear flow, including several boundary layer flows, described in table 4.1.

TABLE 4.1. Description of evaluated data sets

Flow Type	Data	Re_{SP}	NT_P	ST_P	Ri
SSHSF[a]	DNS	0 - 28	0 - 1	0 - 10	0 - 0.6
NSC[b]	DNS	4 - 163	-	3.8 - 9.4	-
NSC & SSC[c]	DNS	0.1 - 43	0.4 - 45	3.5 - 62	0 - 0.52
NSEL[d]	DNS	3.5 - 36	-	3.9 - 6	-
SSEL[e]	DNS	0.1 - 13.5	0.42 - 1.2	1 - 6	0 - 0.3
SSHSF[f]	WT	0 - 17	3.8 - 50	5 - 100	0.02 - 1
SHEBA[g]	Obs	1,100 - 300,000	0.15 - 25	3.7 - 21	0 - 7.7
CASES-99[h]	Obs	1,200 - 300,000	0.2 - 42	4 - 19	0 - 7.3
FLOSSII[i]	Obs	6,900 - 450,000	0.2 - 100	5 - 100	0 - 7.8

[a]Stably stratified homogeneous shear flow (Shih et al., 2000).

[b]Neutrally stratified channel flow (Hoyas and Jiménez, 2006). Data from log-law region, $0.05 \lesssim z/h \lesssim 0.9$.

[c]Neutrally and stably stratified channel flow (García-Villalba and del Álamo, 2011). Data from log-law region, $0.05 \lesssim z/h \lesssim 0.9$.

[d]Neutrally stratified Ekman layer flow (Miyashita et al., 2006). Data is taken above the buffer region ($z^+ \gtrsim 20$) and $\overline{w'\theta'} < 0.05(\overline{w'\theta'})_s$.

[e]Stably stratified Ekman layer flow (Deusebio et al., 2014). Data is taken above the buffer region ($z^+ \gtrsim 20$) and $\overline{w'\theta'}$ is negative.

[f]Stably stratified homogeneous shear flow wind tunnel experiments (Keller and van Atta, 2000).

[g]Surface Heat Budget of the Arctic Ocean experiment (SHEBA) (Uttal et al., 2002).

[h]Cooperative Atmospheric Surface Exchange Study - 1999 (CASES-99) (Poulos et al., 2002).

[i]Fluxes over Snow Surfaces II experiment (FLOSSII) (Mahrt and Vickers, 2005).

4.3.1. ENERGETICS OF STABLY STRATIFIED TURBULENCE. We first analyze the turbulent mixing levels through the non-dimensionalized effective eddy viscosity, ν_{eff}/ν where $\nu_{\text{eff}} = \nu_t + \nu$. Figure 4.1 compares ν_{eff}/ν as a function of Ri revealing that the SABL data exhibit mixing rates several orders of magnitude larger than the DNS and wind tunnel studies. Within the Reynolds-averaged framework, high values of ν_t for strong stability (e.g. high Ri) support the conclusion of Galperin et al. (2007) that a critical value of gradient Richardson number, Ri_c, is not universally applicable. In fact, turbulence likely never completely collapses in geophysical flows due to local instabilities and bursts of three-dimensional turbulence. As illustrated in figure 4.2, the local turbulent production Reynolds number, Re_P, in the SABL is $O(10^7)$ where additional avenues to turbulence are possible (Riley and Lindborg, 2008) and sustained through coexisting turbulent and non-turbulent motions (Mahrt, 2014).

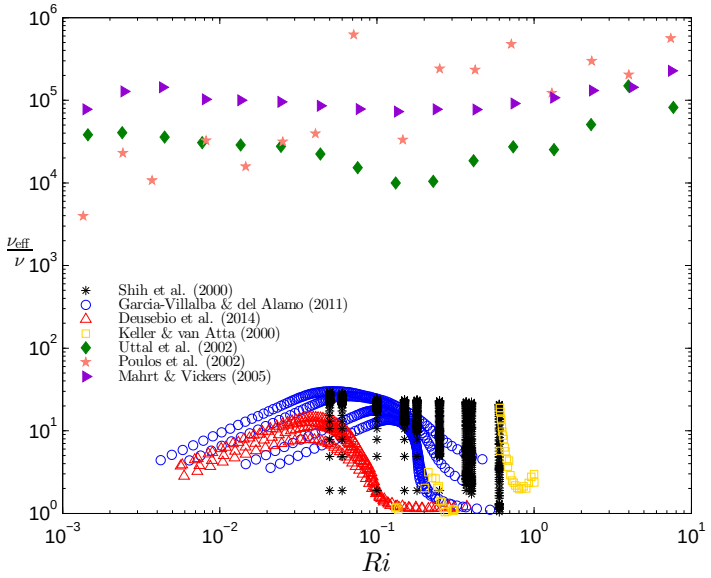

FIGURE 4.1. Non-dimensionalized effective eddy viscosity, ν_{eff}/ν, as a function of gradient Richardson number, Ri.

From these results it is plausible to speculate that the DNS at much higher Re_P will replicate the dynamics observed in geophysical flows. Of course, DNS at the atmospheric or oceanic scales remains a practical impossibility even for the state-of-the-art parallel supercomputer systems.

4.3.2. PARAMETERIZATIONS OF TURBULENT MIXING. In the context of Reynolds averaged modeling, parameterizations link the dynamics of "real-world" turbulence to attainable model quantities. Many meteorological and oceanic models operate under the premise that turbulence shuts down beyond Ri_c but this is not necessarily the case under high Re conditions warranting an analysis of other existing parameterizations.

4.3.2.1. *The Flux Richardson Number.* The flux Richardson number, R_f, is a prominent stability parameter in many operational models. Mellor and Yamada (1982) proposed a model for R_f as a monotonic function of Ri that under stationary, homogeneous conditions approaches an asymptotic maximum value near $Ri \approx 1$. Figure 4.3(a) presents R_f as a

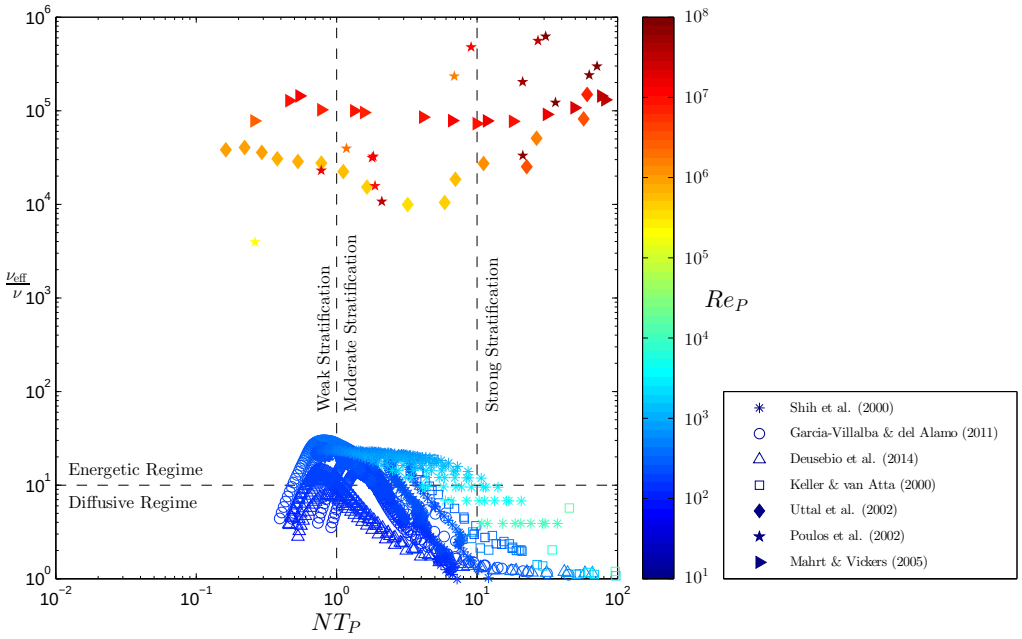

FIGURE 4.2. Non-dimensionalized effective eddy viscosity, ν_{eff}/ν, as a function of buoyancy parameter, NT_P. Symbols are colored by corresponding values of turbulent production Reynolds number, Re_P. The dashed lines roughly delineate indicate regimes of strong mixing and weak mixing for varying buoyancy effects.

function of Ri for the ensemble data set. For low Ri the data follow the R_f model function quite well, but deviate under strongly stable conditions indicative of non-stationarity, with a lot of the scatter occurring in the low Reynolds number DNS and laboratory experiments. To further analyze the energetic contribution to stably stratified turbulence, R_f is given as a function of Re_P in figure 4.3(b). It appears that R_f can attain higher values for large Reynolds number flows, contrary to the typically accepted notion that turbulence can not be sustained if $R_f \gtrsim 0.2$ (e.g. see Turner 1973). A complete description of turbulent mixing requires an understanding of the actual mechanisms of turbulence generation (Mater and Venayagamoorthy, 2014b). Data required for such an analysis remains elusive in field studies due to limitations in instrumentation and the geographic extent of such flows.

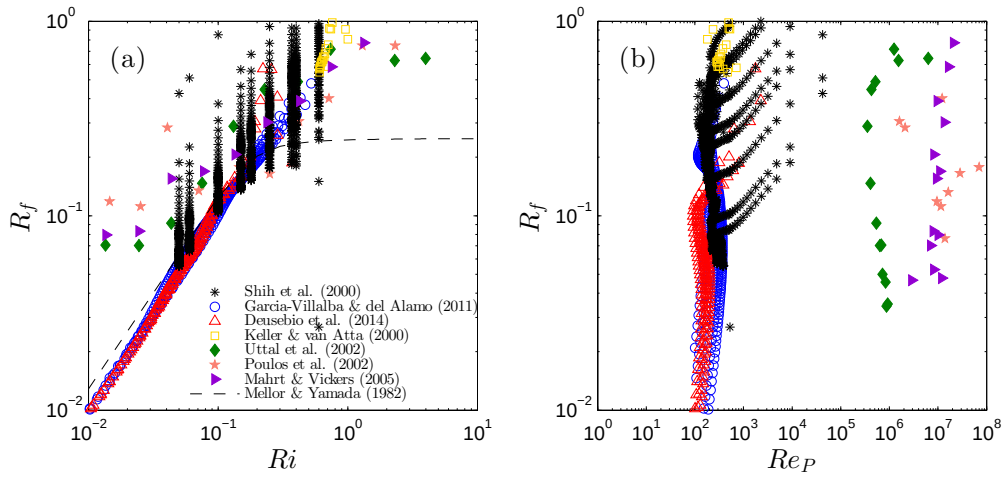

FIGURE 4.3. (a) R_f as a function of Ri plotted with the model function of Mellor and Yamada (1982) (dashed line) and (b) R_f as a function of Re_P.

4.3.2.2. *Relevant Length Scales.* Towards modeling, a key question is what is the correct momentum mixing length under stable flow conditions? Many eddy viscosity models limit the mixing length through stability or damping functions suppressing or extinguishing turbulent mixing (e.g. Holt and Raman, 1988). Motivated by the observation of high mixing in strongly stable stratification from this analysis, we investigate the scaling between the shear length scale, $L_{kS} \equiv k^{1/2}/S$ and the exact mixing length, L_M. For horizontally homogeneous flow conditions, L_M can be written as (Coleman et al., 1990),

$$L_M = \frac{\left(|\overline{u'w'}|^2 + |\overline{v'w'}|^2\right)^{1/4}}{\left[(\partial\overline{u}/\partial z)^2 + (\partial\overline{v}/\partial z)^2\right]^{1/2}}. \tag{4.3}$$

Mater and Venayagamoorthy (2014a) concluded that L_{kS} provides an accurate description of large-scale motions for stably stratified turbulence. We extend this work by comparing the estimate L_{kS} with L_M in figure 4.4. The model constant of L_{kS} is found to be the square root of the stress-intensity ratio, $c = \sqrt{|\overline{u_i'u_j'}|/k} \approx 0.5$, as found in the high-$Re$ laboratory and numerical experiments of Marušic and Perry (1995) and Hoyas and Jiménez (2006). We

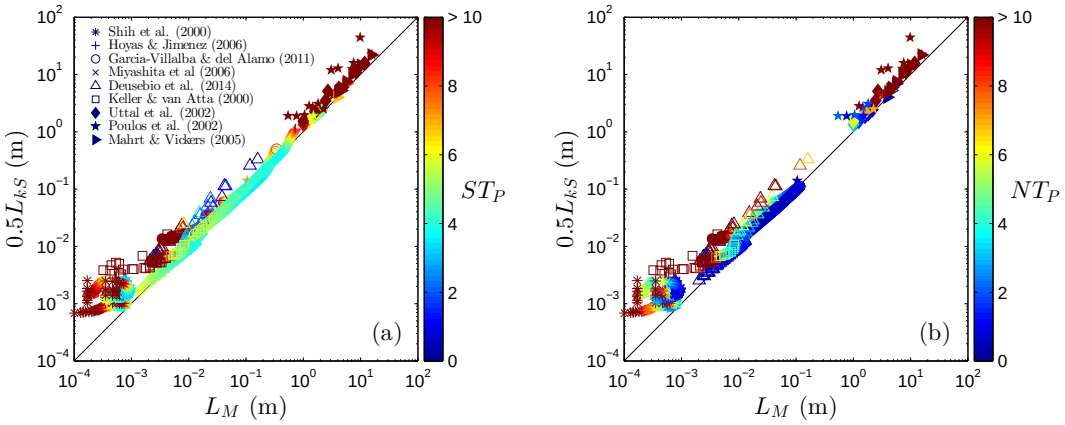

FIGURE 4.4. Comparison of actual and estimated momentum mixing length, L_M and $0.5L_{kS}$, respectively. Symbols in (a) are colored by shear parameter, ST_P, and symbols in (b) are colored by buoyancy parameter, NT_P.

observe that L_{kS} accurately estimates L_M over a wide range of scales ($\sim 10^{-4} - 10^{1}$ m) for neutrally and stably stratified flow conditions. The DNS and laboratory data suggests that L_{kS} does not approximate L_M closely for low ST_P values suggesting $3 \lesssim ST_P \lesssim 10$ as an approximate range of applicability. On the other hand, the low-Re data fall outside at high values of NT_P whereas the SABL data remains well described by L_{kS}. Despite strong buoyancy effects, the high mixing rates (e.g. high Re_{SP}) in the atmospheric data indicate a continued correlation with L_{kS}. The less energetic flows appear to follow the traditional notion of turbulence collapse beyond Ri_c. Thus, we take L_{kS} to accurately estimate L_M in the range $0 \lesssim NT_P \lesssim 10$. These results illustrate that a shear mixing length parameterization provides an accurate measure of the actual mixing of the momentum field for a broad range of stability conditions without reliance on stability or damping functions.

4.3.2.3. *Parameter Space for Stably Stratified Turbulence.* For a turbulent flow (i.e. $Re_P \gg 1$), we can assess the competing shear and buoyancy effects inherent in Ri values through a comparison of the shear and buoyancy parameters, ST_P and NT_P, respectively, in order to explore the range of applicability of the mixing length estimate L_{kS}. Assuming large-scale

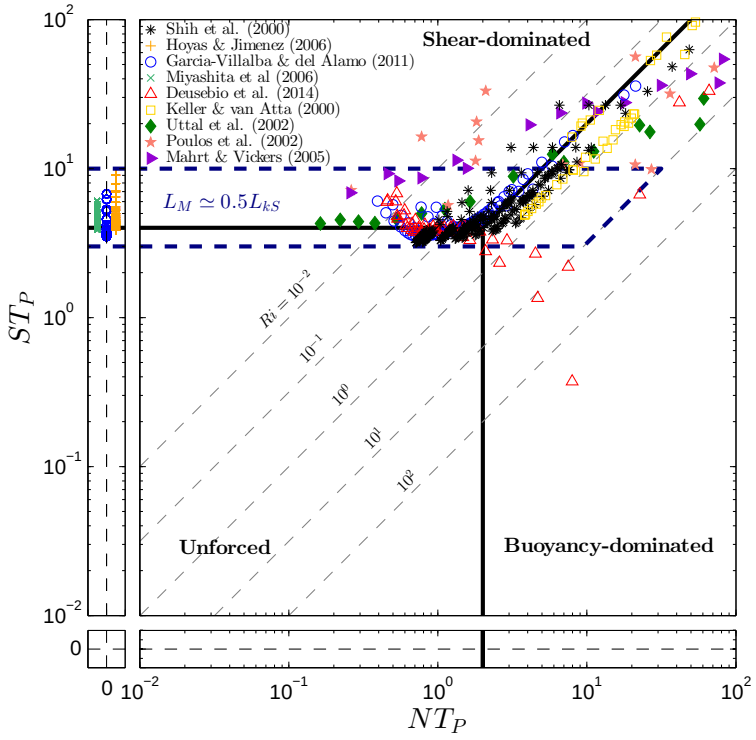

FIGURE 4.5. Parameter space for stably stratified turbulence.

motions correlate with the time scale $T_P \equiv k/P$, we extend the framework of Mater and Venayagamoorthy (2014a) evaluating a ST_P-NT_P parameter space as illustrated in figure 4.5. Conceptually, figure 4.5 represents a cross-section of a three-dimensional space where Re_P extends into and/or out of the page. Thus, data could occupy the same ST_P-NT_P values while being separated by several orders of magnitude in Re_P. The unforced regime is largely artificial only achieved in low-Re experiments of developing turbulence. We take the transition from unforced to shear-dominated turbulence at $ST_P \approx 4$ and from unforced to buoyancy-dominated at $NT_P \approx 2$. ST_P by definition is the inverse of the stress-intensity ratio. For the purpose of description, the transition between the shear- and buoyancy-dominated regimes is taken to be the hydrodynamic stability criterion of $Ri \approx 1/4$. We see that the approximate range of applicability for the estimate L_{kS} discussed in section

4.3.2.2 captures a large portion of the analyzed data. The shear-to-buoyancy transition in geophysical flows remains elusive and we preclude any strict definition of this regime change. The ST_P-NT_P parameter space thus provides a relative measure of the non-dimensional time scale ratios of active turbulence.

4.4. Conclusions

A critical analysis of laboratory, DNS, and field data establishes that assessing flow energetics is crucial to understanding stably stratified turbulence. At high stability, the quasi-horizontal layer motions in conjunction with nonlinear internal wave motions can lead to shear instabilities and injections of three-dimensional turbulence at high Re that may be intermittent or continuous. The dichotomy between small-scale and large-scale flows is clearly illustrated in the orders of magnitude disparity in turbulent mixing levels. As mixing appears to shut-down beyond Ri_c for laboratory and DNS data, strong mixing persists to high Ri for the SABL observations supporting the notion that no energetics Ri_c exists. For these high Reynolds number flows, the shear-based length scale, L_{kS}, provides an accurate estimate for the actual mixing length of the turbulent momentum field, L_M, covering a broad range of the ST_P-NT_P parameter. In boundary layer and geophysical flows, the shear production of turbulent kinetic energy sustains high mixing rates to large values of Ri. The results of this analysis reveal that the dynamics of stable stratified turbulence depend dually on the energetics and stability level and that model parameterizations for geophysical flows cannot rely solely on knowledge garnered from DNS and laboratory experiments.

The research in this chapter presents a theoretical framework with which to critically evaluate parameterizations of stably stratified turbulence. In this light, chapter 5 results as

a natural extension proposing parameterizations for turbulence mixing based on the analysis of observational and LES data of the SABL.

CHAPTER 5

Turbulence Parameterizations for Strongly Stable Stratification[1]

5.1. Introduction

Turbulent mixing in the stable atmospheric boundary layer (SABL) is essential to the transport of momentum, heat, and scalars with direct implications on small-scale (e.g. air quality and wind energy) and large-scale (e.g. circulation and climate change) processes. In geophysical flows, the state of turbulence is influenced largely by shear, stratification, and boundary proximity. Stable stratification suppresses turbulence as restorative buoyant and gravitational forces limit vertical fluctuations transferring turbulent kinetic energy (TKE) to potential energy (PE) or mixing irreversibly on a molecular level. A dynamic equation for TKE for stably stratified homogeneous flow, with the Boussinesq approximation and Einstein summation convention can be written as

$$\frac{\partial k}{\partial t} + \overline{U}_j \frac{\partial k}{\partial x_j} = -\overline{u_i' u_j'} \frac{\partial \overline{U}_i}{\partial x_j} + \frac{g}{\theta_0} \overline{u_i' \theta'} \delta_{i3} - \varepsilon, \tag{5.1}$$

where $k = (1/2)\overline{u_i' u_i'}$ is the turbulent kinetic energy, $-\overline{u_i' u_j'}$ are the turbulent momentum fluxes, g is the gravitational acceleration, θ_0 is a reference potential temperature, $-\overline{u_i' \theta'}$ is the potential temperature flux, δ_{i3} is the Kronecker delta function, and $\varepsilon = \nu \overline{(\partial u_i'/\partial x_j)(\partial u_j'/\partial x_i)}$ is the dissipation rate of turbulent kinetic energy. For a stationary flow, the dominant

[1] A manuscript of the research presented in the chapter has been submitted to the *Journal of the Atmospheric Sciences* entitled "Parameterizations of Turbulent Mixing in the Stable Atmospheric Boundary Layer" and unanimously recommended for publication pending revision based on the comments of three anonymous reviewers. The chapter is written in a collective "we" to acknowledge collaboration with co-author, Dr. Subhas K. Venayagamoorthy. As this manuscript was tailored towards the meteorological community, the nomenclature for eddy viscosity and diffusivity takes the form $K_M \equiv \nu_t$ and $K_H \equiv \kappa_t$.

balance on the right-hand-side (r.h.s.) of equation (5.1) is between the shear production of TKE, $P = -\overline{u_i' u_j'}(\partial \overline{U}_i / \partial x_j)$, buoyancy production (or destruction for stable stratification) of TKE, $B = (g/\theta_0)\overline{u_i' \theta'}\delta_{i3}$, and dissipation of TKE, ε. Within the stably stratified ABL, as stability increases the flow becomes buoyancy-dominated eventually leading to a "collapse" of turbulent mixing and flow relaminarization. Stable stratification also permits additional phenomena such as low-level jets, meandering motions, and internal gravity waves (Mahrt, 1998). Stability can be assessed with a ratio of buoyant to shear production of TKE through the flux Richardson number given by

$$R_f = \frac{-B}{P}. \tag{5.2}$$

For stationary, homogeneous conditions, R_f tends to an upper limit, $R_{f\infty}$, in the range of $0.20 - 0.25$ for atmospheric flows (see e.g. Mellor and Durbin, 1975). A state of continuous turbulence is exhibited for $R_f \lesssim 0.25$ termed the *weakly* stable boundary layer. The *intermittently* stable regime occurs in the range of $0.25 \lesssim R_f \lesssim 1$ and $R_f \gtrsim 1$ indicating the *strongly* stable regime (Stull, 1988; Mahrt, 1998, 1999). R_f may be negative for non-stationary flows represented through imbalance in the production and dissipation terms on the r.h.s. of equation (5.1) (Shih et al., 2005).

Another closely related stability parameter is the gradient Richardson number,

$$Ri = \frac{N^2}{S^2}, \tag{5.3}$$

where $N = [(g/\theta_0)(\partial \overline{\theta}/\partial z)]^{1/2}$ is the buoyancy (or Brunt-Väisällä) frequency, $\overline{\theta}$ is the averaged potential temperature, and $S = [(\partial \overline{u}/\partial z)^2 + (\partial \overline{v}/\partial z)^2]^{1/2}$ is the mean shear rate. Ri

quantifies stability through the ratio of buoyancy frequency to shear leading to the qualification of shear-dominated, $N \ll S$, or buoyancy-dominated, $N \gg S$ delineated about a critical gradient Richardson number, Ri_{c} (Richardson, 1920). Ri_c has been the focus of a vast body of research (e.g. Taylor, 1931; Miles, 1961; Businger et al., 1971; Turner, 1973; Rohr et al., 1988; Itsweire et al., 1993; Armenio and Sakar, 2002; Zilitinkevich and Baklanov, 2002; Galperin et al., 2007; Ohya et al., 2008; Grachev et al., 2013) with a consensus in the range $Ri_c \simeq 0.2 - 1.0$. From classical analysis of stationary, homogeneous conditions, Miles (1961) arrived at $Ri_{\mathrm{c}} \approx 0.25$. As stability increases, shear decreases leading to inertial oscillations such as internal gravity waves. As stability continues to increase, Kelvin-Helmholtz shear instabilities may form and internal waves can break leading to an influx of shear-generated turbulence (Mahrt, 1998; Smyth and Moum, 2000). This process of decreasing and increasing shear results in Ri remaining relatively constant with a value near Ri_{c} (see e.g. Townsend, 1976; Nieuwstadt, 1984; Kim and Mahrt, 1992; Derbyshire, 1994; Mahrt, 1998, and references therein). Further insights on the transition from weakly to strongly stratified turbulence are given through a quasi-dynamic definition of Ri_c where as stability increases, turbulence is sustained up to $Ri \approx 1$; however, for decreasing stability the flow remains laminar until $Ri \approx 0.2$ (Galperin et al., 2007). Sustained turbulence at high Ri remains an area of open research (see e.g. Zilitinkevich et al., 2008).

Lastly, a stability parameter used to describe stratification in boundary layer flows is the Obukhov length (Obukhov, 1946) given by

$$L = -\frac{u_*^3 \theta_0}{\kappa g(\overline{w'\theta'})_0} \tag{5.4}$$

where $u_* = (|\overline{u'w'}|+|\overline{v'w'}|)^{1/2}$ is the friction (or shear) velocity, κ is the von Kármán constant, and $(\overline{w'\theta'})_0$ is the vertical turbulent potential temperature flux at the surface. L describes the characteristic length of the dynamic sublayer (Obukhov, 1946) where stratification effects are negligible (e.g. Monin and Yaglom, 1971). The Obukhov length is commonly associated with Monin-Obukhov (hereafter MO) similarity theory (Monin and Obukhov, 1954) cast in terms of a dimensionless parameter, $\zeta = z/L$. Nieuwstadt (1984) introduced a local similarity theory extending the original framework of MO similarity theory beyond the surface layer defining the terms in equation (5.4) locally. Similarity theory describes the vertical structure of turbulence based on the surface layer parameters and is assumed valid under stationary, homogeneous conditions for the weakly stable regime (Kaimal and Finnigan, 1994). Under very stable conditions, turbulence statistics become independent of height, referred to as "z-less" stratification (Monin and Yaglom, 1971; Wyngaard and Coté, 1972; Nieuwstadt, 1984), where much less is known about the applicability of similarity theory (see e.g. Pahlow et al., 2001, and references therein). More recently, L has been used to describe the onset of turbulence collapse in wall-bounded flows. Nieuwstadt (2005) used a non-dimensional height, h/L, and Flores and Riley (2011) proposed $L^+ = Lu_*/\nu$, although this remains an area of intense research to determine the exact mechanisms of relaminarization.

While large-eddy simulation (LES) studies have become prominent in recent years (see e.g. Beare et al., 2006), many large-scale operational models rely on turbulence parameterizations through the flux-gradient relationships. In a Reynolds-averaged framework, the

turbulent mixing of momentum and heat are absolved into the eddy diffusivities of momentum, K_M, and heat, K_H, respectively.

$$\overline{u'w'} = -K_M \frac{\partial \overline{u}}{\partial z}, \tag{5.5}$$

$$\overline{v'w'} = -K_M \frac{\partial \overline{v}}{\partial z}, \tag{5.6}$$

$$\overline{w'\theta'} = -K_H \frac{\partial \overline{\theta}}{\partial z}, \tag{5.7}$$

where $\overline{u'w'}$ and $\overline{v'w'}$ are the averaged vertical turbulent momentum fluxes. K_M and K_H are also more generically termed the eddy (or turbulent) viscosity and diffusivity, respectively. From dimensional analysis, K_M can be parameterized using characteristic (relevant) velocity and length scales, $K_M \sim u^* l^*$. Models for K_M range in complexity from lower-order schemes with algebraic formulations based on similarity theory (K-theory) to higher-order closures with transport equations for two or more turbulent parameters. Higher-order closure models have not been widely used due to the added computational cost of prognostic equations. One-equation closure models continue to see use in many operational models (see e.g. Holt and Raman, 1988; Cuxart et al., 2006, and references therein). The velocity scale of turbulence can be given by $u^* \sim k^{1/2}$ leading to a model framework with a prognostic equation for TKE and an appropriate mixing length, $l^* \sim l_m$, determined diagnostically. Prandtl's mixing length hypothesis assumes the turbulent eddy size is vertically limited by the height above the surface, $l_m \sim \kappa z$ (Prandtl, 1925). Extended surface-based mixing lengths have been proposed by Blackadar (1962) and Delage (1974) with many subsequent variations (see e.g. Weng and Taylor, 2003; Cuxart et al., 2006; Huang et al., 2013). An alternative approach is to prescribe a local mixing length such as the the buoyancy length scale, $L_B = \sigma_w / N$ where

$\sigma_w = \overline{w'^2}^{1/2}$ is the root-mean-square (r.m.s.) of the vertical velocity fluctuations (e.g. Brost and Wyngaard, 1978; Nieuwstadt, 1984; Hunt et al., 1985). For a uniform flow, σ_w may be an adequate velocity scale (see e.g. Wilson, 2012, and references therein); however, $k^{1/2}$ remains a more general velocity scale applicable to all flow conditions. Several additional local length scales have been investigated (e.g. André et al., 1978; Beljaars and Viterbo, 1998; Weng and Taylor, 2003) yet these formulations take an *ad hoc* approach tuned to match the SABL vertical structure. Considering the governing physics of large-scale motions, turbulence can be classified as "unforced", "shear-dominated", or "buoyancy-dominated" (Mater and Venayagamoorthy, 2014a). In this study, we explore pertinent length scales of turbulent mixing in the SABL and develop parameterizations for eddy viscosity and diffusivity based on atmospheric observations and LES data.

The paper is organized as follows. In section 5.2, we briefly outline the data sets from field campaigns containing high quality measurements of stably stratified atmospheric turbulence. We also introduce the large-eddy simulation (LES) data set for moderately stable conditions of the GEWEX Atmospheric Boundary Layer Study (GABLS). In section 5.3, we first present a discussion on relevant length scales and provide an assessment of how well the two proposed length scales compare with the exact mixing length for momentum using observational data. This is followed by propositions for parameterizing the eddy viscosity and diffusivity. An *a priori* analysis of the LES data is performed to evaluate the parameterizations applied to the SABL vertical structure in section 5.4. Conclusions are given in section 5.5.

5.2. Description of Data Sets

5.2.1. The SHEBA Data. The Surface Heat Budget of the Arctic Ocean experiment (SHEBA) took place from October 1997 to September 1998 in the Beaufort Gyre north

of Alaska that drifted from from approximately 74° N and 144° W to 81° N and 166° W. Full descriptions of the SHEBA campaign, measurement techniques, and data quality can be found in the works of Andreas et al. (1999), Persson et al. (2002), and Uttal et al., (2002). Primary mean and turbulent data were collected on a 20 m tower with five instrumented levels at 2.2, 3.2, 5.1, 8.9, and 18.9 or 14 m depending on the season. The data set contains hourly averaged (1-h) measurements. The gradients of mean velocity and potential temperature are calculated using a second-order polynomial fit and respective derivatives at the individual measurement levels (e.g. Grachev et al., 2005). The data from first level, 2.2 m, is excluded from our analysis due to prominent surface interactions with drifting snow leading to significant scatter (Sorbjan and Grachev, 2010). Bin-averaging is performed using Ri to prescribe bins into which all other data are then sorted. The SHEBA data captured nearly 6000 hours of measurements mostly for weakly stable conditions and absent of common contaminants (e.g. surface inhomogeneities, drainage flows, etc.).

5.2.2. The CASES-99 Data. The Cooperative Atmosphere-Surface Exchange Study - 1999 (CASES-99) was a large collaborative field campaign lasting from 1 to 31 October 1999 in southeastern Kansas, USA located at approximately 38° N latitude (Poulos et al., 2002). Data were collected on a 60 m main tower with sonic anemometers at six levels and 34 thermocouples. Wind speeds were measured at 1, 5, 20, 30, 40, 45, and 50 m while temperatures were measured at 1, 5, 15, 25, 35, 45, and 55 m. The gradients of mean velocity and potential temperature are calculated using a sixth-order polynomial fit and respective derivatives at the individual measurement levels (Sorbjan and Grachev, 2010). The original data set of 5 minute averaged measurements is transformed to hourly averages (1-h). Bin-averaging followed the same procedure as for the SHEBA data based on Ri. The CASES-99

data set contains very stable measurements with weak and strong turbulent mixing events (Mahrt and Vickers, 2006) as well as nocturnal phenomena such as internal gravity waves, Kelvin-Helmholtz instabilities, and drainage fronts (Poulos et al., 2002; Mahrt, 2007).

5.2.3. The GABLS LES Data. The first Global Energy and Water Cycle Experiment (GEWEX) Atmospheric Boundary Layer Study (GABLS) initiative provided an intercomparison of LES (Beare et al., 2006) and single-column models (Cuxart et al., 2006) with an eye towards mixing length specification for national weather prediction (NWP) and climate models. The LES study presents insights on the behavior of the SABL dynamics albeit with lower turbulence and stability levels than those observed in the aforementioned field campaigns and is based on the simulations of Kosović and Curry (2000). The 2.0 m resolution LES reference data set conducted by the National Center for Atmospheric Research (NCAR) (Sullivan et al., 1994) is selected for analysis of proposed turbulence parameterizations in this study.

5.3. Theoretical Formulation

5.3.1. Relevant Length Scales. Relevant velocity and length scales describe active large-scale turbulent motions. From the flux-gradient relationships in equations (5.5), (5.6), and (5.7) and Prandtl's mixing length hypothesis, an "exact" mixing length for momentum can be defined as

$$L_M = \frac{u_*}{S} \equiv \frac{\left(|\overline{u'w'}|^2 + |\overline{v'w'}|^2\right)^{1/4}}{\left[(\partial\overline{u}/\partial z)^2 + (\partial\overline{v}/\partial z)^2\right]^{1/2}}, \tag{5.8}$$

Blackadar (1962) observed eddies tend to reach a maximum size away from the surface defined by $\lambda = 2.7\times10^{-4}Gf^{-1}$ where G is the geostropic wind speed and f is the Coriolis parameter. In practice, λ is oftentimes assigned a constant value in the range 6 - 200 m (e.g. Huang et al.,

2013, and references therein). Combining $l_m \sim \kappa z$ near the surface and $l_m \sim \lambda$ away from the surface, Blackadar (1962) proposed $l_m \sim L_{\text{Blackadar}} = (1/\kappa z + 1/\lambda)^{-1}$. Delage (1974) modified $L_{\text{Blackadar}}$ by adding a stability term given by $l_m \sim L_{\text{Delage}} = (1/\kappa z + 1/\lambda + \beta/\kappa L)^{-1}$ where $\beta \approx 4.7$ is a model constant (Businger et al., 1971). Surface-based mixing lengths provide accurate model predictions when used in conjunction with model constants and stability functions (see e.g. Cuxart et al., 2006) but lack generality in describing active scales of turbulent mixing.

In seeking a unified view of turbulent mixing in the SABL, pertinent length scales can be expressed for unforced, shear-dominated, and buoyancy-dominated turbulence. This approach is not meant to discount the contributions of MO or local similarity theories but rather to focus on fundamental aspects of stably stratified turbulence from which we can develop model parameterizations. The first regime represents unforced or decaying turbulence governed by the length scale, $L_{k\varepsilon} = k^{3/2}/\varepsilon$. While this regime is certainly important to a complete understanding of the SABL, measurements are difficult to obtain with weak winds and fluxes approaching instrument sensitivity. Since we are unable to quantify the unforced regime with atmospheric observations, we focus our efforts on the shear- and buoyancy-dominated regimes. In the shear-dominated regime, the Corrsin length scale represents the largest survivable eddy, $L_C = (\varepsilon/S^3)^{1/2}$ (Corrsin, 1958). Likewise, the Dougherty-Ozmidov length scale, $L_O = (\varepsilon/N^3)^{1/2}$, pertains to the buoyancy-dominated regime (Dougherty, 1961; Ozmidov, 1965). However, L_C and L_O generally describe small-scale turbulence in oceanic flows and direct measurements of ε are historically difficult to obtain and have only recently been captured with microstructure instruments (e.g. Sorbjan and Balsley, 2008). This leads us to seek more suitable length scales from attainable quantities applicable to the high mixing

rates in the atmosphere. Two additional length scales can be constructed with the ratio of the velocity scale, $k^{1/2}$, to a time scale assigned here to explicitly include shear and buoyancy effects by S^{-1} and N^{-1}, respectively.

$$L_{kS} = \frac{k^{1/2}}{S}, \tag{5.9}$$

$$L_{kN} = \frac{k^{1/2}}{N}. \tag{5.10}$$

L_{kS} corresponds to the active fluctuations representing an averaged eddy size for shear flow (Venayagamoorthy and Stretch, 2010) and L_{kN} analogously for a buoyancy-dominant flow. Mater et al. (2013) suggested that L_{kS} and L_{kN} may in fact better describe large-scale motions than L_C and L_O. Through analysis of direct numerical simulation (DNS) and experimental evidence, Mater and Venayagamoorthy (2014a) provide further insights on the relevancy of L_{kS} and L_{kN} for stably stratified shear-flow turbulence.

Equation (5.11) relates the pertinent mixing length scales, L_{kS} and L_{kN}, to the mixing length scale for momentum, L_M.

$$l_m \simeq \begin{cases} C_{kS} L_{kS} \\ \\ C_{kN} L_{kN} \end{cases}, \tag{5.11}$$

where C_{kS} is a constant given by

$$C_{kS} \simeq \frac{L_M}{L_{kS}} \equiv \frac{\left(|\overline{u'w'}|^2 + |\overline{v'w'}|^2\right)^{1/4}}{k^{1/2}}. \tag{5.12}$$

We note that C_{kS} is the square root of the familiar stress-intensity ratio ($C_{kS} = c$) given by

$$c^2 = \frac{\left(|\overline{u'w'}|^2 + |\overline{v'w'}|^2\right)^{1/2}}{k}. \tag{5.13}$$

Numerous experimental studies of unstratified turbulent wall-bounded flows dating back to the 1970's suggest that $c \approx 0.55$ (see e.g. Launder and Spalding, 1974). However, recent high Reynolds number DNS (e.g. Hoyas and Jiménez, 2006) and experimental (see e.g. Marušic and Perry, 1995, and references therein) studies suggest convergence to $c \approx 0.50$ in energetic flows. While the value of c has been extensively investigated for high Reynolds number unstratified boundary layer flows, its dependency on stratification has not received much attention limited to the works of Nieuwstadt (1984) and Mauritsen et al. (2007). Hence, a pertinent question is how does c vary with stable stratification (e.g. with Ri)? Using observations for very high Reynolds number SABL flows, we see a very interesting behavior of C_{kS} presented in figure 5.1. The data indicates two dominant trends. The first striking observation is that C_{kS} remains approximately constant, $C_{kS} = c \approx 0.50$, regardless of stratification. Second, we observe diminishing C_{kS} with increasing stability. The bifurcation in C_{kS} indicates that the stress-intensity ratio may depend dually on the level of stratification and the flow energetics. We can qualitatively delineate energetic and diffusive limits for C_{kS} through a "unique" parameter which we will term the shear-production Reynolds number, Re_{SP}, defined by

$$Re_{SP} = \frac{K_M}{\nu} = \frac{P}{\nu S^2} = \left(\frac{k^2}{\nu P}\right)\left(\frac{P}{kS}\right)^2 = Re_P (ST_P)^{-2}, \tag{5.14}$$

where Re_P is a turbulent (production) Reynolds number, ST_P is a non-dimensional shear parameter that quantifies the ratio of the turbulence production time scale $T_P \equiv k/P$ to the

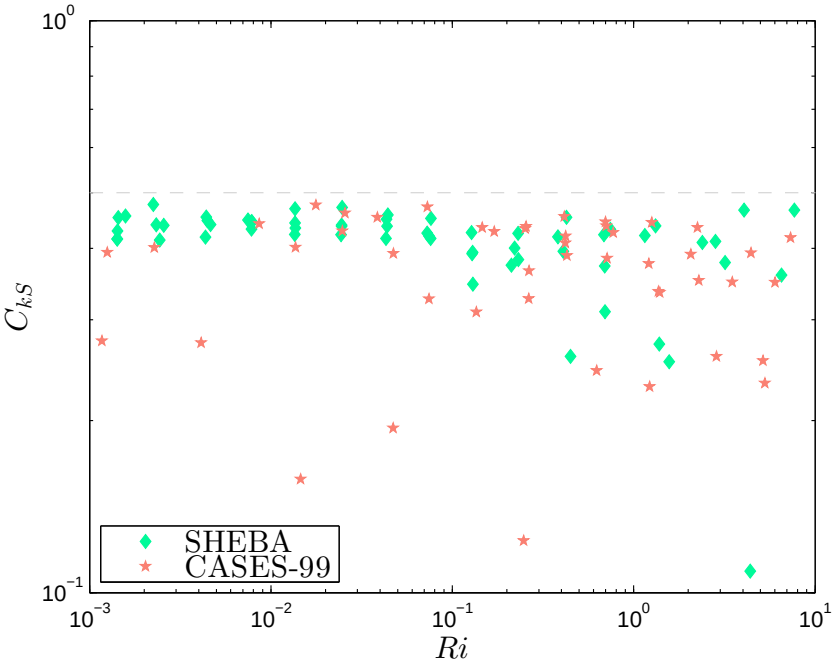

FIGURE 5.1. An evaluation of the model constant C_{kS} as a function of gradient Richardson number Ri. Symbols represent the bin-averaged 1-h SHEBA (diamonds) and CASES-99 (stars) data sets. The gray dashed line represents $C_{kS} = 0.50$.

mean shear time scale S^{-1}. Figure 5.2 presents C_{kS} as a function of Re_{SP}. The presence of high mixing rates (e.g. high Re_{SP}) at high Ri debunks the notion that turbulence can not survive at very high stratification. While weak- and strong-mixing regimes at high Ri have been previously discussed (Zilitinkevich et al., 2008), Re_{SP} lends clarity to the mechanisms of turbulent mixing through shear production of TKE. From these observations, we take a value of $C_{kS} = 0.50$ for further analysis of atmospheric observations.

Additionally, we can define the constant C_{kN} from equation (5.11) as

$$C_{kN} \simeq \frac{L_M}{L_{kN}} \simeq \frac{C_{kS} L_{kS}}{L_{kN}} = C_{kS} Ri^{1/2}. \tag{5.15}$$

Here, we assume that $C_{kN} \simeq C_{kS}/2 = 0.25$. L_{kS} and L_{kN} have been previously studied in the context of the SABL as sub-grid scale (SGS) components of the dissipation length

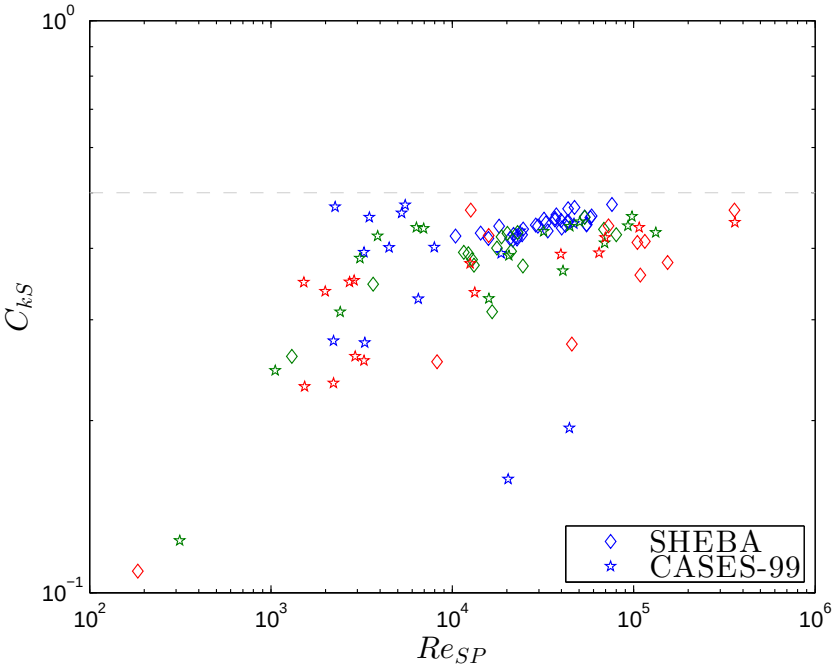

FIGURE 5.2. C_{kS} as a function of the shear-production Reynolds number Re_{SP}. Symbols represent the bin-averaged 1-h SHEBA (diamonds) and CASES-99 (stars) data sets and are colored by stability for the ranges $0 < Ri \leq 0.1$ (blue); $0.1 < Ri \leq 1.0$ (green); and $1.0 < Ri \leq 10.0$ (red). The gray dashed line represents $C_{kS} = 0.50$.

scale (see e.g. Kosović and Curry, 2000) or through mixing lengths of single-column models (see e.g. Grisogono and Belušić, 2008). These previous studies largely employed empirical constants without strict physical relevance. In this research, we have thoroughly evaluated the dependence of the stress-intensity ratio on stability and energetics. Based on the trends of the stress-intensity ratio, we designate $l_m \simeq 0.50 L_{kS}$ and $l_m \simeq 0.25 L_{kN}$ as estimates for the exact mixing length of momentum.

Figure 5.3 compares estimated mixing lengths for momentum with the actual mixing length. To aid in visualization, the bin-averaged data is differentiated into three regimes: (i) *weakly* stable, $0 < Ri \leq 0.1$ (blue symbols); (ii) *intermittently* stable, $0.1 < Ri \leq 1.0$ (green symbols); and (iii) *strongly* stable, $1.0 < Ri \leq 10.0$ (red symbols). Due to high mixing rates of significant portions of data, we do not partition data based on a strict definition of Ri_{c}. We

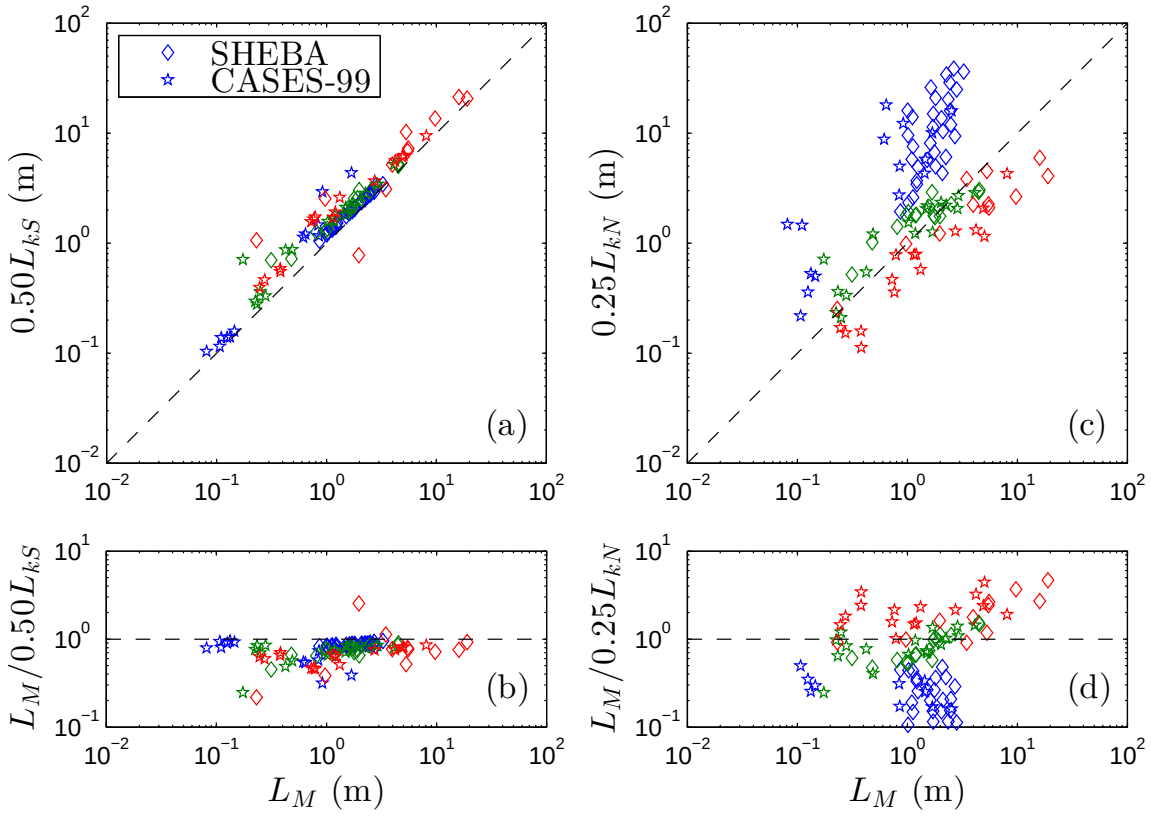

FIGURE 5.3. Comparison of estimated and actual turbulent mixing lengths for momentum: (a) $0.50L_{kS}$ and (c) $0.25L_{kN}$. A normalized ratio of actual to estimated mixing length is presented in (b) $L_M/0.50L_{kS}$ and (d) $L_M/0.25L_{kN}$. Symbols represent the bin-averaged 1-h SHEBA (diamonds) and CASES-99 (stars) data sets and are colored by stability for the ranges $0 < Ri \leq 0.1$ (blue); $0.1 < Ri \leq 1.0$ (green); and $1.0 < Ri \leq 10.0$ (red).

see that $0.50L_{kS}$ compares very well with L_M for all stability and $0.25L_{kN}$ best approximates L_M in the intermittent regime with some agreement in the strongly stable regime. We also observe a wide range of scales in these three regimes. Of particular interest are the large scales at strong stability indicating very active eddies for $1.0 < Ri \leq 10.0$ which we generally tend to associate with non turbulent motions. Large-scale motions indicate significant shear-generated turbulence from breakdown of inertial motions or low-level jets. From analysis of the pertinent length scales, we observe that L_{kS} is an accurate estimate for turbulent mixing whereas L_{kN} seems rather limited in its application to this data.

5.3.2. Eddy Viscosity. The actual eddy viscosity can be determined from the horizontal stress, $\tau \sim u_*^2 = (|\overline{u'w'}|^2 + |\overline{v'w'}|^2)^{1/2}$, and mean shear rate, S, written as

$$K_M = \frac{u_*^2}{S} \equiv \frac{\left(|\overline{u'w'}|^2 + |\overline{v'w'}|^2\right)^{1/2}}{\left[(\partial\overline{u}/\partial z)^2 + (\partial\overline{v}/\partial z)^2\right]^{1/2}}. \tag{5.16}$$

In developing estimates for eddy viscosity from $K_M \sim u^* l^*$, we can assume that an additional model constant is associated with the velocity scale, $u^* \sim k^{1/2}$, given by

$$C_k \simeq \frac{L_M S}{k^{1/2}} \equiv \frac{\left(|\overline{u'w'}|^2 + |\overline{v'w'}|^2\right)^{1/4}}{k^{1/2}}. \tag{5.17}$$

We see that the model constant C_k is also defined by the square root of the stress-intensity ratio, $C_k \equiv C_{kS} = 0.50$. Using the previous analysis of pertinent length scales, two eddy viscosity parameterizations can be defined as

$$\tilde{K}_M \simeq \begin{cases} C_{kS} L_{kS} C_k k^{1/2} \\ C_{kN} L_{kN} C_k k^{1/2} \end{cases}, \tag{5.18}$$

Applying numerical values for the model constants of the observational data we obtain $\tilde{K}_{M_{kS}} \simeq 0.25 L_{kS} k^{1/2}$ and $\tilde{K}_{M_{kN}} \simeq 0.13 L_{kN} k^{1/2}$. Figure 5.4 compares the estimated and actual eddy viscosity. $\tilde{K}_{M_{kS}}$ performs much better than $\tilde{K}_{M_{kN}}$ for the shear-dominated regime while $\tilde{K}_{M_{kS}}$ and $\tilde{K}_{M_{kN}}$ both perform well for the buoyancy-dominated regime. Within the buoyancy-dominated regime, we can observe strong turbulent mixing rates indicative of large-scale events such as the breaking of highly energetic internal waves, low-level jets, or Kelvin-Helmholtz shear instabilities. These points scale better with $\tilde{K}_{M_{kS}}$ as opposed to $\tilde{K}_{M_{kN}}$ at high Ri. Although $\tilde{K}_{M_{kN}}$ shows good comparison with weakly turbulent events at high stratification, a more comprehensive strongly stable data set is needed with similar

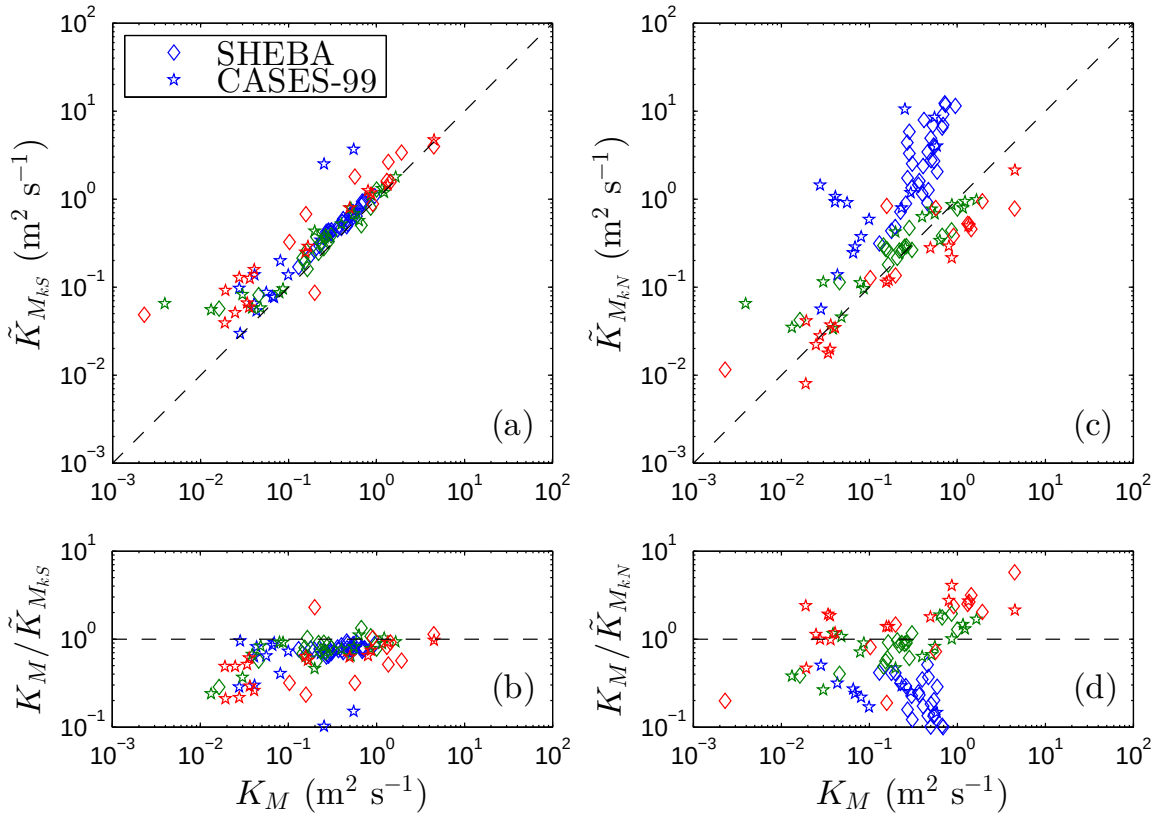

FIGURE 5.4. Comparison of estimated and actual eddy viscosity: (a) $\tilde{K}_{M_{kS}} \simeq 0.25 L_{kS} k^{1/2}$ and (c) $\tilde{K}_{M_{kN}} \simeq 0.13 L_{kN} k^{1/2}$; with the model constants $C_{kS} = 0.50$, $C_{kN} = 0.25$, and $C_k = 0.50$, respectively. A normalized ratio of actual to estimated eddy viscosity is presented in (b) $K_M/\tilde{K}_{M_{kS}}$ and (d) $K_M/\tilde{K}_{M_{kN}}$. Symbols represent the bin-averaged 1-h SHEBA (diamonds) and CASES-99 (stars) data sets and are colored by stability for the ranges $0 < Ri \leq 0.1$ (blue); $0.1 < Ri \leq 1.0$ (green); and $1.0 < Ri \leq 10.0$ (red).

conditions for further evaluation. Such data often remains elusive because representative wind speed and flux measurements approach the instrument sensitivity and may be difficult to separate from unforced turbulence without direct measurements of ε.

5.3.3. EDDY DIFFUSIVITY AND THE TURBULENT PRANDTL NUMBER. The eddy diffusivity of heat is linked to the eddy viscosity through the turbulent Prandtl number, $Pr_t \equiv K_M/K_H \equiv Ri/R_f$. Under neutral stratification, Pr_{t0} is considered to be in the range 0.5 - 1.0 (Kays and Crawford, 1993; Pope, 2000). Businger et al. (1971) proposed $Pr_{t0} \simeq 0.74$

from observations of the 1968 Kansas experiment and Venayagamoorthy and Stretch (2010) arrived at a value of $Pr_{t0} \simeq 0.7$ from fundamental analysis of homogeneous shear flow DNS data. While an exact Pr_t still remains elusive and oftentimes is treated as a tuning parameter in operational models, a strong body of research suggests Pr_t is strongly linked to stability from DNS (e.g. Gerz et al., 1989; Holt et al., 1992; Shih et al., 2000), experiments (e.g. Rohr et al., 1988; Strang and Fernando, 2001), analytical models (e.g. Schumann and Gerz, 1995; Zilitinkevich et al., 2007; Venayagamoorthy and Stretch, 2010), and atmospheric observations (e.g. Webster, 1964; Kondo et al., 1978; Kim and Mahrt, 1992). From definition, Pr_t is assumed to vary linearly with Ri and inversely with R_f. However, numerous studies have concluded that the behavior of R_f can be described with a monotonically increasing function of Ri (see e.g. Townsend, 1958; Mellor and Yamada, 1982; Nakanishi, 2001) reaching a asymptotic limit nearing stationarity in the strongly stable regime, $R_f \rightarrow R_{f\infty} = 0.25$. Under the same conditions, Pr_t is a weak linear function for low stability, $Pr_t \approx Ri$, increasing to $Pr_t \approx 4Ri$ for strong stability. What this simple theoretical derivation does not address is the fact that many SABL flows exhibit non-stationarity and inhomogeneities not included in most stability-dependent prescriptions of Pr_t. Venayagamoorthy and Stretch (2010, hereafter VS10) developed a novel Pr_t proposition derived from a generalized theoretical framework of stationary and non-stationary conditions including irreversible mixing contributions given by

$$Pr_t = Pr_{t0} \exp\left(-\frac{Ri}{Pr_{t0}\Gamma_\infty}\right) + \frac{Ri}{R_{f\infty}}, \tag{5.19}$$

where $Pr_{t0} \simeq 0.7$, $R_{f\infty} = 0.25$, and $\Gamma_\infty = R_{f\infty}/(1 - R_{f\infty}) \simeq 0.33$ is the mixing efficiency nearing strong stability. We note that several other stability-dependent Pr_t formulations have been proposed (see e.g. Kim and Mahrt, 1992; Schumann and Gerz, 1995; Zilitinkevich

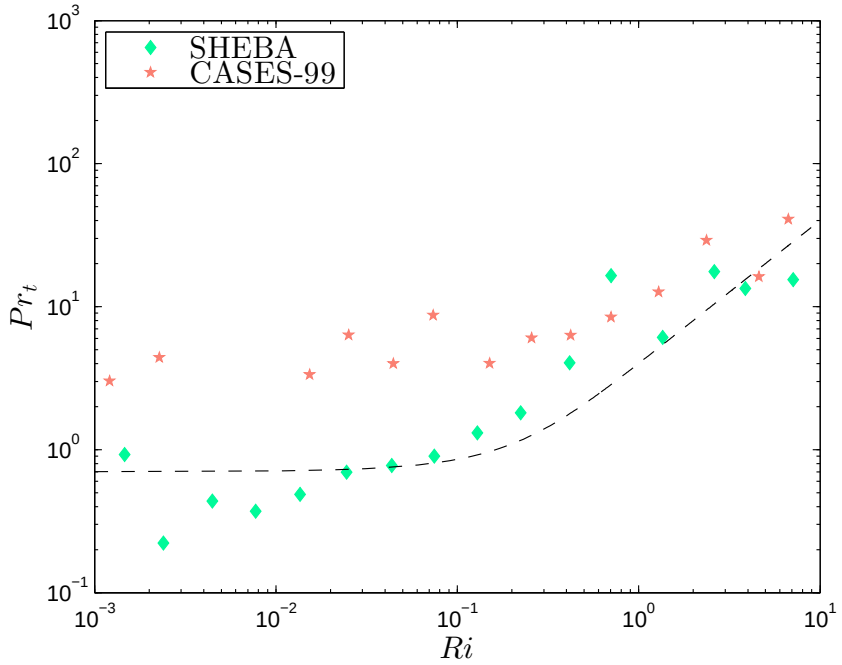

FIGURE 5.5. Evaluation of the actual Pr_t and the proposition of Venayagamoorthy and Stretch (2010, VS10), $Pr_{t_{\mathrm{VS10}}}$ given by equation (5.19) (dashed line) as functions of Ri. Symbols represent the mean bin-averaged 1-h SHEBA (diamonds) and CASES-99 (stars) data sets.

et al., 2007), and references therein) with similar behavior in weak and strong stability. We use the turbulent Prandtl number of VS10 to estimate the eddy diffusivity of heat. Figure 5.5 reveals that Pr_t is indeed a function of Ri from the mean bin-averaged SHEBA and CASES-99 data sets despite some scatter near neutral stability for the SHEBA data set. The data presented in figure 5.5 clearly illustrates the Pr_t increases with Ri for strongly stable flow conditions indicating a decrease in eddy diffusivity implying that momentum transfer is more efficient at strong stability compared to scalar transport.

The eddy diffusivity is now predicted from $\tilde{K}_H \simeq K_M/Pr_t$ with a constant turbulent Prandtl number, $Pr_{t_{0.74}} = 0.74$, and the stability-dependent formula of VS10, $Pr_{t_{\mathrm{VS10}}}$. Figure 5.6 compares the estimated and exact eddy diffusivity with VS10 noticeably improving the prediction of K_H especially for the moderately and strongly stable data. Figure 5.7

compares the parameterized and actual eddy diffusivity with estimates only using $Pr_{t_{\text{VS10}}}$. Both parameterizations perform well in the moderately and strongly stable regimes. The departure of the weakly stable SHEBA data (blue diamonds) in figure 5.7(a) is attributed to the lows values of Pr_t nearing neutral stability as seen in figure 5.5. $\tilde{K}_{M_{kN}}$ appears to accurately predict K_H in figure 5.7(b); however, this result is inaccurate largely due to the over estimation of K_M in the shear-dominated regime leading to the spurious estimation of K_H. Concluding our analysis of observational data from the SHEBA and CASES-99 field campaigns, the parameterization of eddy viscosity, $\tilde{K}_{M_{kS}}$ is an accurate parameter under all stability regimes including strong mixing events in very stable flow conditions. For the weakly turbulent events in the buoyancy-dominated regime, $\tilde{K}_{M_{kN}}$ represents an accurate parameterization. In evaluating the eddy diffusivity of heat, the stability-dependent Pr_t of VS10 improves predictions from $\tilde{K}_H \simeq K_M/Pr_t$ when compared with a constant, $Pr_t = 0.74$. Overall, our generalized assessment of turbulent parameters based on the local pertinent length scales, L_{kS} and L_{kN}, provides insights on turbulence in both shear- and buoyancy-dominated regimes.

5.4. *A priori* Analysis of the SABL Vertical Profile

5.4.1. Model Constants. The SHEBA and CASES-99 data sets clearly indicate that the square root of the stress intensity ratio approaches a constant value for high mixing rates in stably stratified flows with $C_{kS} \equiv C_k \approx 0.50$. With measurements from fixed meteorological towers limited to observations in the lower portion of the ABL, LES data provides information on the upper SABL vertical structure. We revisit C_{kS} as a function of Ri and Re_{SP} in figure 5.8 for the 2.0 m resolution NCAR LES data set from the first

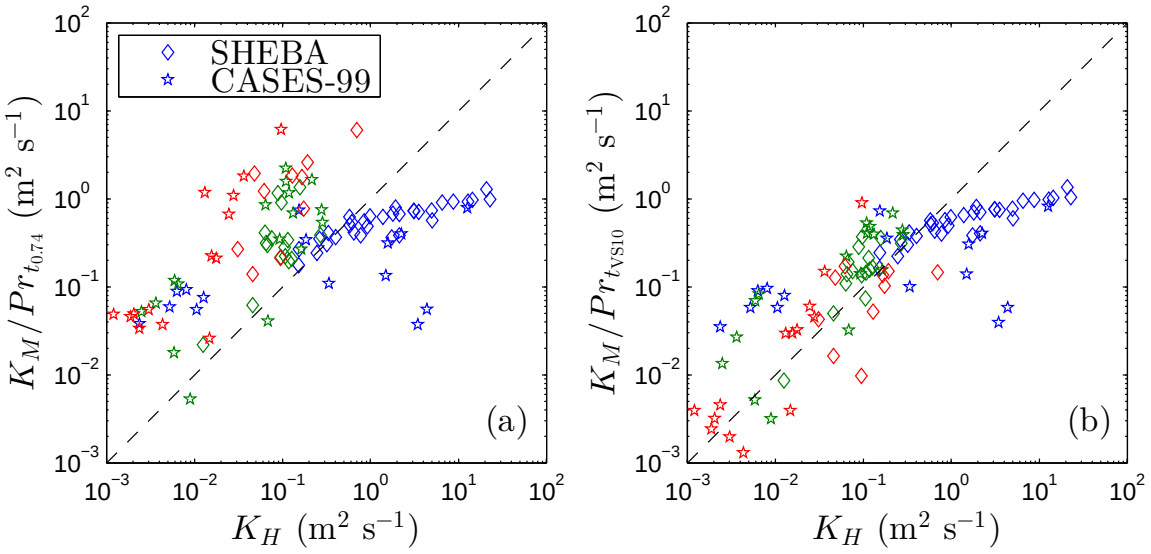

FIGURE 5.6. Comparison of the estimated and actual eddy diffusivity defined as the ratio of (a) actual eddy viscosity to the turbulent Prandtl number, $\tilde{K}_H \simeq K_M/Pr_{t_{0.74}}$ and (b) $\tilde{K}_H \simeq K_M/Pr_{t_{\mathrm{VS10}}}$. The estimated eddy diffusivities in (a) and (b) are based on a constant Prandtl number, $Pr_{t_{0.74}} = 0.74$ and the stability-dependent Prantl number formula of Venayagamoorthy and Stretch (2010, VS10), $Pr_{t_{\mathrm{VS10}}}$ given by equation (5.19), respectively. Symbols represent the bin-averaged 1-h SHEBA (diamonds) and CASES-99 (stars) data sets. Symbols are colored by stability for the ranges $0 < Ri \leq 0.1$ (blue); $0.1 < Ri \leq 1.0$ (green); and $1.0 < Ri \leq 10.0$ (red).

GABLS intercomparison. In the LES analysis of the SABL, transitioning to the buoyancy-dominated regime above the boundary layer height, the flow is less energetic. We observe that the LES data follows the trajectory of the diffusive limit for C_{kS}. C_{kS} approaches the asymptotic upper limit of 0.50 for increasing Re_{SP} but is substantially less for low mixing rates. In contrast to the field observations, we do not observe the coexistence of high mixing rates and strong stratification for the LES data set which is in agreement with the widely assumed notion of turbulence collapse for $Ri > Ri_{\mathrm{c}}$. Analysis of the atmospheric data sets reveals very energetic bursts of shear-generated turbulence at high Ri which contrasts the classical view of Ri_{c}.

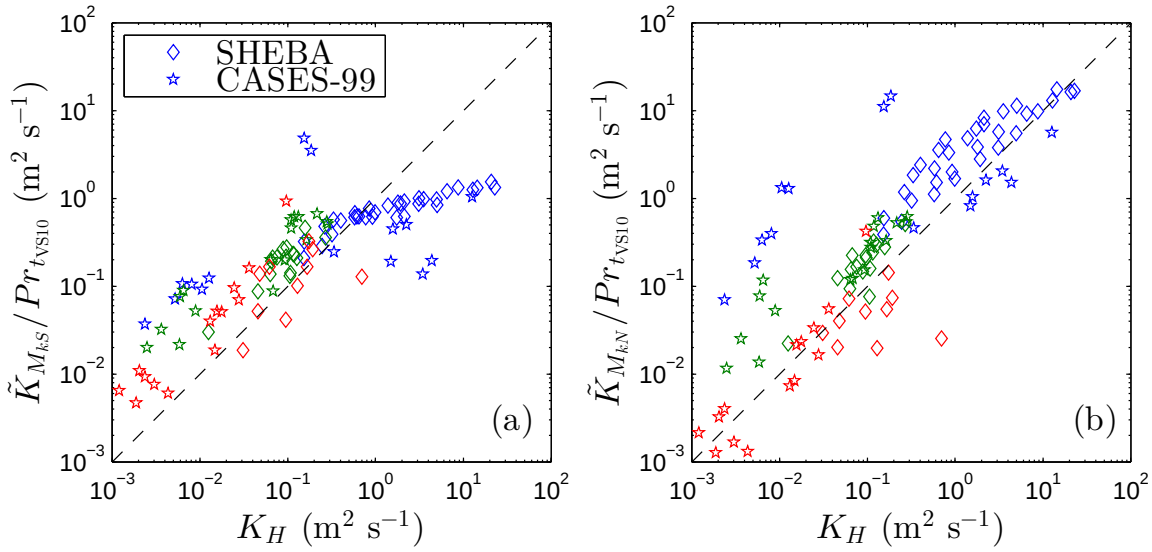

FIGURE 5.7. Comparison of the estimated and actual eddy diffusivity defined as the ratio of estimated eddy viscosity from figure 5.4 to the turbulent Prandtl number , $\tilde{K}_H \simeq \tilde{K}_{M_{kS}}/Pr_{t_{\mathrm{VS10}}}$ (a) and $\tilde{K}_H \simeq \tilde{K}_{M_{kN}}/Pr_{t_{\mathrm{VS10}}}$ (b) where $\tilde{K}_{M_{kS}} \simeq 0.25 L_{kS} k^{1/2}$ and $\tilde{K}_{M_{kN}} \simeq 0.13 L_{kN} k^{1/2}$. Note we employ only the stability-dependent Prandtl number proposition of Venayagamoorthy and Stretch (2010, VS10), $Pr_{t_{\mathrm{VS10}}}$ given by equation (5.19). Symbols represent the bin-averaged 1-h SHEBA (diamonds) and CASES-99 (stars) data sets and are colored by stability for the ranges $0 < Ri \leq 0.1$ (blue); $0.1 < Ri \leq 1.0$ (green); and $1.0 < Ri \leq 10.0$ (red).

5.4.2. EDDY VISCOSITY. In order to advance the proposed turbulent parameters, an *a priori* analysis is performed to evaluate parameterizations of eddy viscosity and diffusivity applied to the SABL vertical structure using the LES data from the first GABLS intercomparison (Beare et al., 2006). In the Reynolds-averaged framework, accurate prediction of eddy viscosity is especially important because overestimation can lead to strong temperature gradients and concentrations of scalar quantities whereas underestimation leads to a very deep boundary layer (Mahrt, 1998). To provide a more complete evaluation, we include existing zero-, one-, and two-equation parameterizations for eddy viscosity in addition to $\tilde{K}_{M_{kS}}$ and $\tilde{K}_{M_{kN}}$ given by equation 5.18. The local similarity model of Nieuwstadt (1984,

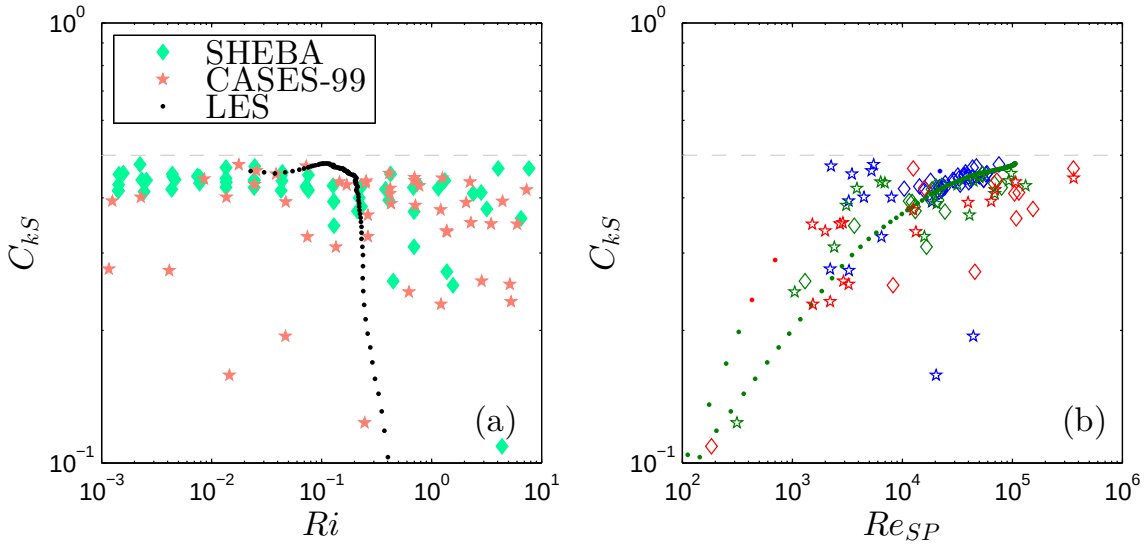

FIGURE 5.8. C_{kS} as a function of (a) Ri for the bin-averaged 1-h SHEBA (diamonds) and CASES-99 (stars) with the NCAR 2.0 m resolution LES data (dots) and (b) shear-production Reynolds number Re_{SP} with symbols colored by stability for the ranges $0 < Ri \leq 0.1$ (blue); $0.1 < Ri \leq 1.0$ (green); and $1.0 < Ri \leq 10.0$ (red). The gray dashed line represents $C_{kS} = 0.50$ in both plots.

hereafter N84) is given by

$$\tilde{K}_M = \frac{\kappa z u_* \left(1 - z/h\right)^2}{1 + \beta z/L}, \tag{5.20}$$

where $h = c_h(u_* L/f)^{1/2}$ is the boundary layer height using the approximation of Zilitinkevich (1972) where $c_h \approx 0.4$ (Garratt, 1982) and $\beta \approx 4.7$ are empirical model constants. The one-equation k-l_m model of André et al. (1978, hereafter A78) gives

$$\tilde{K}_M = l_m \left(\alpha k\right)^{1/2}, \tag{5.21}$$

where $\alpha = 0.3$ is an empirical constant, $l_m = \min\left(L_N, c_s L_{kN}\right)$ is the mixing length with $L_N = [(1+\beta z/L)/\kappa z + 1/\lambda]^{-1}$, and $c_s = 0.36$ is an empirical model constant (Duynkerke and Driedonks, 1987). This implementation specifically represents the modifications proposed by Weng and Taylor (2003) to the original one-equation model of André et al. (1978). The eddy

viscosity for the two-equation k-ε model (Launder and Spalding, 1972) modified for stable stratification is given by

$$\tilde{K}_M = (1 - R_f)\, C_\mu \frac{k^2}{\varepsilon}, \tag{5.22}$$

where $C_\mu = 0.09$ is an empirical model constant. It is noted that the empirical model constants α and C_μ assume a stress-intensity ratio of $c^2 = 0.3$.

Figure 5.9(a) compares the eddy viscosity estimates with the actual eddy viscosity as functions of height. We observe that the parameterization $\tilde{K}_{M_{kS}} \simeq 0.25 L_{kS} k^{1/2}$ accurately estimates the shape and magnitude of the actual eddy viscosity up to the boundary layer height. On the other hand, $\tilde{K}_{M_{kN}} \simeq 0.13 L_{kN} k^{1/2}$ overestimates the magnitude of eddy viscosity in the lower quarter of the boundary layer height but compares quite well as the shear diminishes towards the outer layer. N84 captures the general shape of the actual eddy viscosity, but underestimates the magnitude. A78 misses the shape of the actual eddy viscosity and overestimates the magnitude. Finally, the standard k-ε model significantly overestimates the actual eddy viscosity, a noted difficulty with the k-ε applied to the SABL (e.g. Detering and Etling, 1985; Apsley and Castro, 1997). Overall, the parameterization $\tilde{K}_{M_{kS}}$ performs remarkably well capturing both the shape and magnitude of actual eddy viscosity.

5.4.3. Eddy Diffusivity. Efficacy in predictions of K_H are essential to the transport of heat and other scalars in air pollution and climate change processes. Some interesting features are exhibited in the vertical structure of the SABL. In the outer region, mean shear diminishes leading to super-critical values of Ri and R_f (see e.g. Kosović and Curry, 2000). In Section 3, we observed that the Pr_t proposition of Venayagamoorthy and Stretch (2010) fits the general trend of linear increase with Ri (see e.g. figure 5.5) and leads to accurate

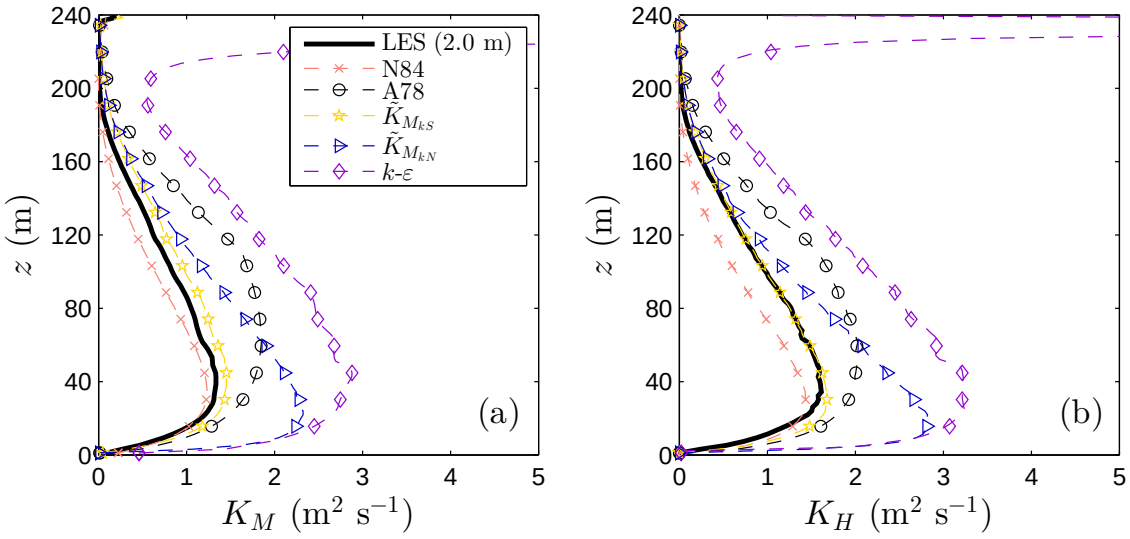

FIGURE 5.9. *A priori* analysis of NCAR 2.0 m resolution LES data for (a) comparison of actual eddy viscosity with estimates for eddy viscosity as functions of height using the proposed parameterizations, $\tilde{K}_{M_{kS}} \simeq 0.25 L_{kS} k^{1/2}$ and $\tilde{K}_{M_{kN}} \simeq 0.13 L_{kN} k^{1/2}$, along with the models of K-theory model of Nieuwstadt (1984, N84), the k-l_m closure of André et al. (1978, A78), and the k-ε model; and (b) comparisons of the actual eddy diffusivity with estimates from the parameterizations of $\tilde{K}_M$ linked through the turbulent Prandtl number proposition of Venayagamoorthy and Stretch (2010, VS10), $\tilde{K}_H \simeq \tilde{K}_M / Pr_{t_{\mathrm{VS10}}}$, as functions of height.

predictions of eddy diffusivity from figures 5.6(b) and 5.7. We now assess the predictions of eddy diffusivity from our *a priori* analysis of LES data using the turbulent Prandtl number of VS10 to provide the linkage between predicted eddy diffusivity and eddy viscosity models, $\tilde{K}_H \simeq \tilde{K}_M / Pr_{t_{\mathrm{VS10}}}$. Figure 5.9(b) compares the vertical profiles of predicted and exact eddy diffusivity. The comparisons in figure 5.9(b) reveals the same general trends for predicted eddy diffusivity and viscosity because of the consistent use of $Pr_{t_{\mathrm{VS10}}}$. The parameterized eddy diffusivity given by $\tilde{K}_H \simeq \tilde{K}_{M_{kS}} / Pr_{t_{\mathrm{VS10}}}$ most accurately predicts the actual eddy diffusivity magnitude and profile. The *a priori* analysis of quasi-stationary LES data for the moderately stable ABL provides some interesting insights for the suggested parameterizations of turbulent mixing. A turbulence collapse was not apparent in the atmospheric

observations (e.g. L_{kS} and $\tilde{K}_{M_{kS}}$ prove accurate even up to $Ri = 10$). Overall, the pertinent length scales, L_{kS} and L_{kN}, provide accurate measures of the large-scale motions in the SABL from which turbulence parameterizations are developed and tested with atmospheric and LES data.

5.5. Conclusions

In this research, we sought to characterize the active turbulent eddies with pertinent length scales using local (or z-less) formulations. Assessing stability through Ri, we generalize flow classification as shear-dominated or buoyancy-dominated. The two length scales, L_{kS} and L_{kN}, are determined to be accurate descriptors of large-scale motions in shear- and buoyancy-dominated flows, respectively, using the data sets from the SHEBA and CASES-99 field campaigns. The analysis of model constants provides insights on the stress-intensity ratio that can be further defined through energetic and diffusive limits. Using Re_{SP} as a measure of flow energetics, we observed that $C_{kS} \approx 0.50$ for high Re_{SP} for all Ri but C_{kS} decreases with Ri for low mixing rates. This perspective suggests that the existence of turbulence for strongly stable flow conditions is influenced more by the large-scale energetics (e.g. Re_{SP}) than Ri. From this assessment of length scales and model constants, we develop subsequent parameterizations for eddy viscosity, $\tilde{K}_{M_{kS}}$ and $\tilde{K}_{M_{kN}}$, respectively, which predict similar trends compared with the actual K_M. Notably, the CASES-99 data set includes observations of nocturnal phenomena (e.g. low-level jets and Kelvin-Helmholtz shear instabilities) which inject strong shear-generated turbulence. These events lead to $\tilde{K}_{M_{kS}}$ comparing well with K_M even in the strongly stable regime and $\tilde{K}_{M_{kN}}$ generally restricted to describing weak turbulent mixing of the buoyancy-dominated regime. We further evaluate K_H from atmospheric observations and the Pr_t formulation of Venayagamoorthy and

Stretch (2010) yielding a more accurate prediction of K_H as opposed to a constant value for Pr_t especially for moderately and strongly stable flow conditions.

These turbulence parameterizations are further evaluated with an *a priori* analysis of the GABLS LES intercomparison data for the SABL vertical structure. While the LES data exhibits only moderately stable stratification and is less turbulent, we observe the shear-based parameters perform well in the lower portion of the boundary layer. As shear diminishes above the boundary layer height, the buoyancy-based parameters become pertinent. A notable result of this research is that the proposed shear-based parameterization for eddy viscosity, $\tilde{K}_{M_{kS}}$, accurately predicts K_M irrespective of stability or non-stationarity in atmospheric observations. In developing a framework for numerical models, the transition between $\tilde{K}_{M_{kS}}$ and $\tilde{K}_{M_{kN}}$ occurs in the realm of $Ri \approx Ri_{\mathrm{c}}$ near the half boundary layer height. Using these eddy viscosity propositions with a stability-dependent Pr_t such as VS10, an accurate measure of eddy diffusivity, K_H, can be obtained. A natural extension of this current work is to implement the proposed turbulence parameters in an operational model for the stable atmospheric boundary layer within the larger context of turbulence modeling in NWP, global circulation, and climate models.

The research in this chapter constitutes the turbulent parameterizations necessary for a Reynolds-averaged model of the SABL. However, implementation requires further effort with careful attention to initial and boundary conditions, numerical schemes, and validating cases. Chapter 6 presents the numerical implementation of the turbulence parameterizations from chapter 5 giving careful consideration to the conclusions made in chapter 4.

CHAPTER 6

Numerical Modeling of Stably Stratified Turbulence with a Hybrid One-Equation Turbulence Closure Model

6.1. Introduction

The research presented in this chapter develops a numerical model based on turbulence parameterizations presented in chapter 5. In a field saturated with numerical models, a gap remains in the growing body of evidence suggesting that strong turbulent mixing can persists under strongly stable stratification in highly energetic geophysical flows (e.g. Cheng et al., 2002; Galperin et al., 2007; Canuto et al., 2008; Zilitinkevich et al., 2008) and the bulk of Reynolds-averaged models that assume turbulence shut-off. Excellent reviews of existing operational and research models are presented by Holt and Raman (1988), Weng and Taylor (2003), and Cuxart et al. (2006). Foremost in the modeling community is turbulent kinetic energy, $k = (1/2)\overline{u_i' u_i'}$, closure for the eddy viscosity, $\nu_t = c l_m k^{1/2}$ where c is an empirical model constant and l_m is a prescribed mixing length.

Recent model developments have focused on the alternatives approaches. Wilson (2012) used the root-mean-square of the vertical velocity fluctuation, $\sigma_w = \overline{w'^2}^{1/2}$, providing a eddy viscosity given by $\nu_t = \sigma_w^2 \tau_w$ where $\tau_w = (\kappa u_* z)/\sigma_w^2$ is an empirical time scale, κ is the von Kármán constant, u_* is the friction velocity, and z is height. For stably stratified turbulent flows, σ_w closure inherently limits turbulence mixing as vertical perturbations are suppressed. While this model showed promise further efforts are needed to validate this model. Another school of thought in recent years is of a total turbulent energy (TTE) closure, $E = k + E_P$

where $E_P = (1/2)\sigma_\theta^2 \beta^2 N^{-2}$, $\sigma_\theta = \overline{\theta'^2}^{1/2}$ is the potential temperature variance, $\beta = g/\theta_0$ is the buoyancy parameter, and N is the buoyancy frequency (e.g. Zilitinkevich and Baklanov, 2002; Mauritsen et al., 2007; Zilitinkevich et al., 2007, 2013). However, these models often rely on considerable empiricism and tuning of model constants.

Employing the estimates for eddy viscosity, ν_t prescribed by equation (5.18) in chapter 5, a turbulent kinetic energy closure is developed with an eye toward the stably stratified atmospheric boundary layer. In an *a priori* analysis of high-Re atmospheric and large-eddy simulation (LES) data, $L_{kS} \equiv k^{1/2}/S$ is found to be an accurate estimate for the mixing length of the momentum field. A shear-based parameterization entails some inherent limitations, for example, as shear diminishes transitioning from the boundary layer to the free atmosphere. In this case, an additional length scale is necessary such as $L_{kN} \equiv k^{1/2}/N$ for stably stratified conditions or $L_{k\varepsilon} \equiv k^{3/2}/\varepsilon$ central to the k-ε closure scheme. The developed model is evaluated for stably stratified channel and Ekman layer flows based on the DNS studies of García-Villalba and del Álamo (2011) and Coleman et al. (1992), respectively. Simulations are performed using in the open-source computational fluid dynamic (CFD) code OpenFOAM (Open Field Operation and Manipulation).

In what follows, section 6.2 contains the theoretical background for this hybrid model proposition. Section 6.3 describes the developed hybrid model. The channel and Ekman layer flows as well as numerical implementation are described in section 6.4. Results are presented and discussed in section 6.5. Conclusions are given in section 6.6.

6.2. Theoretical Background

In developing L_{kS} as an estimate for the turbulent momentum mixing length, L_M (equation (5.8)), an apparent empirical constant C_{kS} is required (equation (5.12)). C_{kS} represents

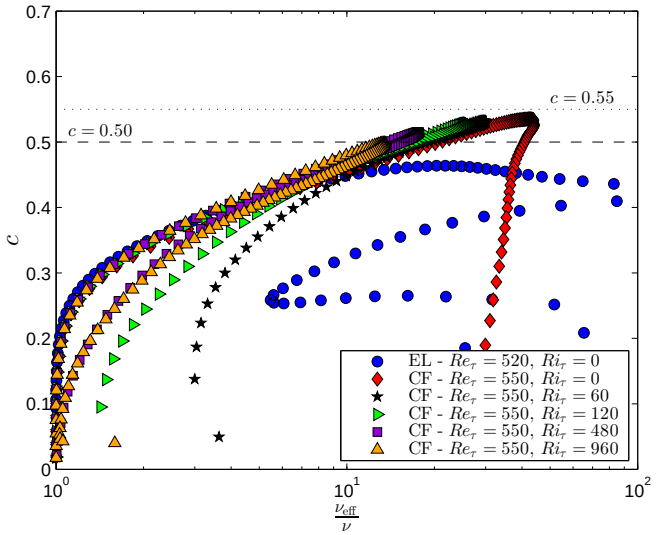

FIGURE 6.1. Square root of the stress-intensity ratio, c, as a function of non-dimensional effective eddy viscosity, ν_{eff}/ν for the unstratified Ekman layer flow (EL) DNS data of Miyashita et al. (2006) and the unstratified and stably stratified channel flow (CF) DNS data of García-Villalba and del Álamo (2011).

the square root of the stress intensity ratio, $C_{kS}^2 = c^2 = |\overline{u'w'}|/k$. In chapter 5, this value is evaluated for atmospheric flows and found to be approximately 0.5 coinciding with the energetic value observed by Marušic and Perry (1995) and Hoyas and Jiménez (2006). The SHEBA and CASES-99 data also suggest that the stress-intensity ratio remains approximately constant for high-Ri. Figure 6.1 compares values of c as functions of non-dimensional eddy viscosity, ν_{eff}/ν, for the Ekman layer data of Miyashita et al. (2006) and channel flow data of García-Villalba and del Álamo (2011). This data is moderately turbulent revealing that the traditional value of $c \approx 0.55$ may in fact be a more appropriate choice for simulations of these flows.

Additionally, as stratification increases for the channel flow, both ν_{eff}/ν and c are reduced in magnitude. García-Villalba and del Álamo (2011) noted that for $Re_\tau = 550$ the laminar flow patches begin to appear in the channel core for $Ri_\tau \gtrsim 120$ while the near-wall region remains turbulent up to $Ri_\tau \gtrsim 1920$. $Re_\tau = u_* h/\nu$ is the friction Reynolds number where

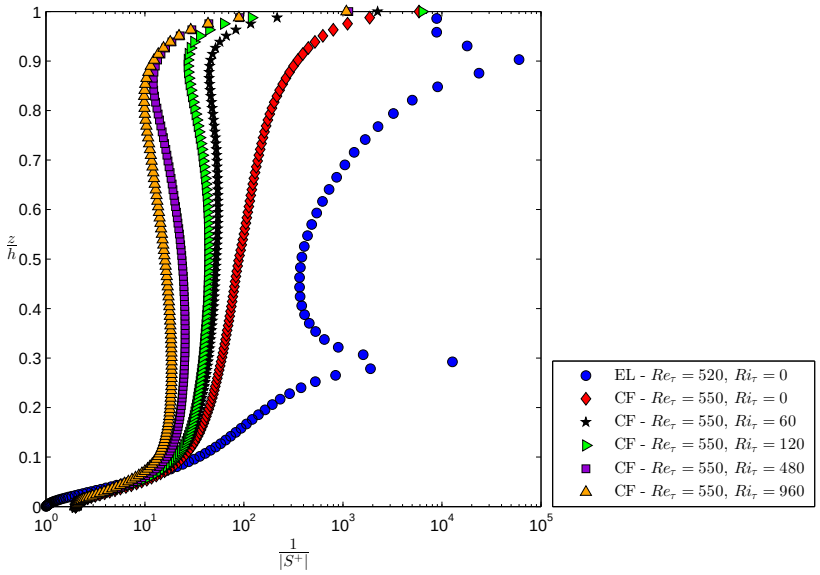

FIGURE 6.2. Evaluation of non-dimensional shear, $|S^+|^{-1}$, as a function of height for the unstratified Ekman layer flow (EL) DNS data of Miyashita et al. (2006) and the unstratified and stably stratified channel flow (CF) DNS data of García-Villalba and del Álamo (2011).

u_* is the friction velocity. $Ri_\tau = \Delta\rho g h/\rho_0 u_*^2$ is the friction Richardson number, $\Delta\rho$ is the density difference between the top and bottom channel walls, h is the channel depth, and ρ_0 is the reference density.

Both channel and Ekman layer flows are shear, boundary layer flows for which L_{kS} provides an accurate estimate for momentum mixing as illustrated in figure 4.4. In regions where shear diminishes (e.g. the channel core), singularities may present in the definition of L_{kS} causing numerical instabilities. To assess the potential for such regions, the inverse non-dimensional shear, $|S^+|^{-1}$, is evaluated as a function of height above the lower surface for these flows. Furthermore, this issue is elucidated further through comparing estimations for the momentum mixing length in figure 6.3. L_{kS} yields an accurate estimate up to $z/\delta \approx 0.9$, above which L_{kN} continues to predict L_M quite well.

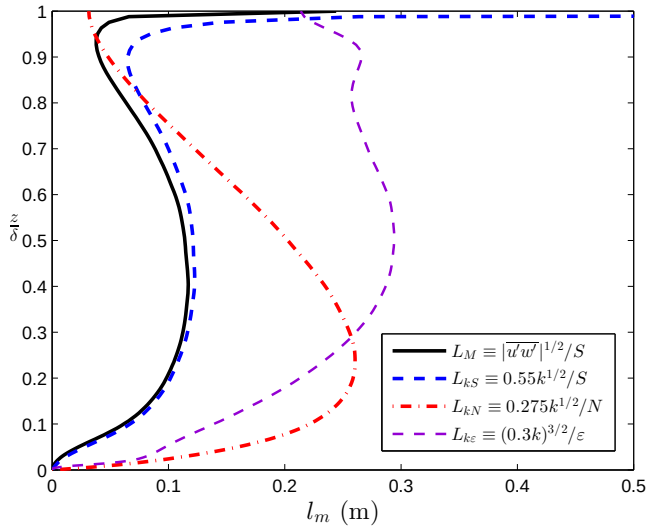

FIGURE 6.3. Comparison of the actual and estimates of the mixing length for the momentum field for stably stratified channel flow with $Re_\tau = 550$ and $Ri_\tau = 60$ from the DNS data of García-Villalba and del Álamo (2011).

6.3. Model Description

The model proposed here assumes a Reynolds-averaged framework employing a prognostic equation for k (equation (3.35)). Here, ε remains an unknown. Rather than solving an algebraic formula, the transport equation for ε (equation (3.41)) is solved. The previous section highlights the capabilities of L_{kS} for estimating L_M. The eddy viscosity can be solved according to

$$\nu_t = c l_m k^{1/2}, \tag{6.1}$$

where c is the square root of the stress-intensity ratio and l_m is the prescribed mixing length. To alleviate the potential for numerical instability, the mixing length is given by

$$l_m = \min\left[c\frac{k^{1/2}}{S}, \frac{c}{2}\frac{k^{1/2}}{N}\right]. \tag{6.2}$$

It is noted that equation (6.2) resembles the formulation of Grisogono and Belušić (2008) for prediction of katabatic flows; however, their model constants were established through a tuning procedure with an inverse relationship (the constant for L_{kS} is one half that of L_{kN}).

The eddy diffusivity for heat is solved for according to $\kappa_t \equiv \nu_t Pr_t^{-1}$. On the basis of the *a priori* study of the GABLS intercomparison LES data in chapter 5, a constant Prandtl number, $Pr_t = 0.74$, and the stability-dependent formulation of Venayagamoorthy and Stretch (2010) will be used (equation (5.19)). For wall-bounded flow, turbulent effects of the near-wall region (e.g. wall-blocking) are likely to have an effect on the transport of momentum and heat and, in turn, on the turbulent Prandtl number (e.g. McEligot and Taylor, 1996; Srinivasan and Papavassiliou, 2011). Karimpour and Venayagamoorthy (2014b) developed a simple Pr_t formulation for wall-bounded stably stratified flows that incorporates the near-wall effects written as

$$Pr_t = \left(1 - \frac{z}{h}\right) \frac{Ri}{R_f} + \left(1 - \frac{z}{h}\right) Pr_{twd0} + Pr_{t0}, \tag{6.3}$$

where $Pr_{twd0} \approx 0.4$ is the difference between the neutral value of $Pr_{t0} = 0.7$ and the value at the wall $Pr_{tw0} \approx 1.1$. R_f is determined by an empirical fit to the model function of Mellor and Yamada (1982)

$$R_f = R_{f\infty}[1 - \exp(-\gamma Ri)], \tag{6.4}$$

where $R_{f\infty} = 0.25$ is the asymptotic limit of mixing and $\gamma = 7.5$ is a model constant. Interestingly, the turbulent potential temperature flux profiles of Nieuwstadt (1984) follow a similar linear profile for the SABL (equation 3.29)).

6.4. Numerical Methods

The development of an operational turbulence model requires significant programming, testing, and validation with appropriate data. As a first step in this process, channel and Ekman layer flow with moderate Reynolds numbers and stratification levels are simulated.

6.4.1. Channel Flow.

A one-dimensional stably stratified turbulent smooth-wall channel flow is simulated for a shear Reynolds number of $Re_\tau = 550$ and stratification levels of $Ri_\tau = 60$ and 120 similar to García-Villalba and del Álamo (2011). The model equations for momentum and density transport are given by

$$\frac{\partial \overline{u}}{\partial t} = -\frac{1}{\rho_0}\frac{\partial \overline{p}}{\partial x} + \nu_{\text{eff}}\frac{\partial^2 \overline{u}}{\partial z^2}, \tag{6.5}$$

and

$$\frac{\partial \overline{\rho}}{\partial t} = \kappa_{\text{eff}}\frac{\partial^2 \overline{\rho}}{\partial z^2}. \tag{6.6}$$

The flow is driven by a constant pressure gradient in the streamwise (x) direction determined from the hydrostatic pressure distribution $-(\partial\overline{p}/\partial x) = \rho_0 u_*^2/h$. Equations (6.5) and (6.6) are solved for using numerical integration in time and space with a merged PISO (Pressure Implicit with Splitting of Operator) SIMPLE (Semi-Implicit Method for Pressure-Linked Equations) in OpenFOAM through a modified version of the `pimpleFoam` solver (OpenCFD, 2012). Spatial and temporal discretization are set to second-order accuracy for flow and turbulent parameters. The stratified cases were initialized from a converged unstratified velocity field onto which a linear density profile is imposed. The simulations were then run until all residuals were minimized before comparing with the averaged, quasi-steady state DNS data of García-Villalba and del Álamo (2011).

6.4.2. Ekman Layer Flow. A two-dimensional stably stratified turbulent Ekman layer flow is simulated over a smooth surface with steady system rotation after Coleman et al. (1992). A relevant Reynolds number is given by $Re_f = G\delta_E/v = 400$ where $G = (u_g^2+v_g^2)^{1/2}$ is geostropic wind speed, $\delta_E = (2\nu/f)^{1/2}$ is the laminar Ekman layer depth, and f is the Coriolis parameter. $Re_f = 400$ corresponds to $Re_\tau = 520$. The Reynolds-averaged momentum and potential temperature equations for a horizontally homogeneous Ekman layer flow are given by

$$\frac{\partial \overline{u}}{\partial t} = f(\overline{v} - v_g) + \nu_{\text{eff}} \frac{\partial^2 \overline{u}}{\partial z^2}, \tag{6.7}$$

$$\frac{\partial \overline{v}}{\partial t} = -f(\overline{u} - u_g) + \nu_{\text{eff}} \frac{\partial^2 \overline{v}}{\partial z^2}, \tag{6.8}$$

$$\frac{\partial \overline{\theta}}{\partial t} = \kappa_{\text{eff}} \frac{\partial^2 \overline{\theta}}{\partial z^2}. \tag{6.9}$$

Equations (6.7)–(6.9) are also solved with a modified `pimpleFoam` solver. Spatial and temporal discretization are second-order accurate for flow and turbulent parameters. The flow field is initially converged for a unstratified case and onto which the initial potential temperature profile is imposed. The stratification level corresponds to a Grashof number $Gr = g\beta_V \theta_w h^3/\nu^2 = 3.15 \times 10^6$ where β_V is the volume expansion coefficient and θ_w is the potential temperature at the bottom wall surface. $Gr = 3.15 \times 10^6$ corresponds to the wall Richardson number of $Ri_w = g\Gamma_w \delta_E/(\theta_w G) = 0.001$ where $\Gamma_w = (\partial\overline{\theta}/\partial z)_w$ is the potential temperature gradient at the wall (or lapse rate). The initial temperature profile is impose according to

$$\theta(z) = \frac{a_*}{2}\left(\frac{-\pi}{\ln(0.01)}\right)^{1/2} \Gamma_w \text{erf}\left(\frac{z/a_*}{(-\ln(0.01))^{-1/2}}\right) + \theta_0, \tag{6.10}$$

where a_* is the approximate height at which $\partial\overline{\theta}/\partial x$ is 1% of Γ_w. For this case, a_*/δ_E is given as 5. As DNS data of a stably stratified Ekman layer flow was not readily available,

the results of Coleman et al. (1992) for a non-dimensional time of $tf = 1.8$ were digitized for evaluation with results.

6.4.3. Wall Boundary Conditions. The standard smooth-wall functions are used for both cases (e.g. Ferziger and Milovan, 1996). Setting the first grid point at the edge of the logarithmic layer ($y^+ \approx 30$), values of k, ε, and $\overline{u}$ can be calculated. Assuming there is no turbulent kinetic energy flux through the solid surface, k is assigned a zero-gradient condition in the wall-normal direction,

$$\left(\frac{\partial k}{\partial z}\right)_w = 0, \tag{6.11}$$

where the subscript $_w$ denotes a value at the wall surface. ε at the first grid point, ε_P, is given by

$$\varepsilon_P = \frac{C_\mu^{3/4} k_P^{3/2}}{\kappa z_P}. \tag{6.12}$$

Rather than assigning the velocity at the first grid point, a more robust formulation connects the wall shear stress to the velocity gradient of the first computational cell to determine the velocity. The shear stress at the wall is related to the mean streamwise velocity by

$$\tau_w = \rho u_*^2 = \rho C_\mu^{1/4} \kappa k^{1/2} \frac{\overline{u}}{\ln(z^+ E)}, \tag{6.13}$$

where $u_* = C_\mu^{1/4} k^{1/2}$ is the shear velocity defined using the local equilibrium assumption, $z^+ = z u_* / \nu$ is the non-dimensional height, $E = \exp(\kappa B)$ is an empirical constant related to the thickness of the viscous sublayer, and $B \approx 5.2$. Assuming that the shear production at

TABLE 6.1. Additional model closures

Model	ν_t	Model Constants
k-ε[a]	$(1-R_f)C_\mu\frac{k^2}{\varepsilon}$	$C_\mu = 0.09$
MA48[b]	$\kappa u_* z\left(1-\frac{z}{\delta}\right)(1+\beta Ri)^\alpha$	$\beta = 10,\ \alpha = -1/2$
N84[c]	$\frac{u_*\kappa z(1-z/h)^2}{1+\beta z/L}$	$\beta = 4.7$

[a]Jones and Launder (1972); Launder and Spalding (1974)
[b]Munk and Anderson (1948)
[c]Nieuwstadt (1984); Holtslag and Nieuwstadt (1986)

the wall is given by $P \approx \tau_w(\partial\overline{u}/\partial z)$, the velocity derivative can be given by

$$\left(\frac{\partial\overline{u}}{\partial z}\right)_P = \frac{C_\mu^{1/4}k_P^{1/2}}{\kappa z_P} \tag{6.14}$$

Equations (6.11)–(6.14) constitute the necessary and sufficient boundary conditions for smooth-wall turbulent boundary layer flows.

6.5. RESULTS

In addition to the proposed model formulation, the standard k-ε and the algebraic formulations of Munk and Anderson (1948) and Nieuwstadt (1984) for the channel and Ekman layer flows, respectively. Table 6.5 provides the details for these additional closure models.

6.5.1. CHANNEL FLOW. The proposed model with $c = 0.55$ produces results very close to the standard k-ε model. The proposed model with $c = 0.5$ clearly deviates to some degree as expected based on the moderate Reynolds number of this channel flow shown in figure 6.1. The algebraic eddy viscosity formula of Munk and Anderson (1948) displays the greatest deviations from the DNS data for all scenarios. The Pr_t of Karimpour and Venayagamoorthy (2014b) produces density profiles closer to the DNS profiles observed in figures 6.6 and 6.9. To this point it remains unclear as to whether this result depends solely

on the imposed linear distribution (equation (6.3)) or the higher $Pr_t \approx 1.1$ at the first gird point alleviates the early departure of the density profile observed in figures 6.4, 6.5, 6.7, and 6.8, for example.

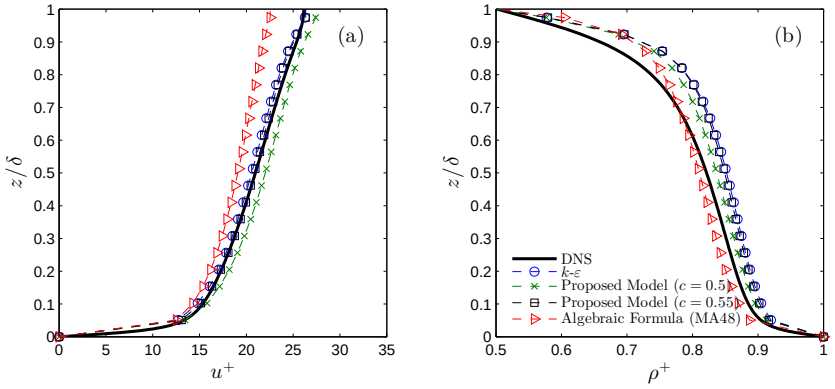

FIGURE 6.4. Channel flow results for $Re_\tau = 550$ and $Ri_\tau = 60$ with $Pr_t = 0.74$. Vertical profiles for (a) non-dimensional velocity, u^+ and (b) non-dimensional density, ρ^+ compared with DNS data of García-Villalba and del Álamo (2011).

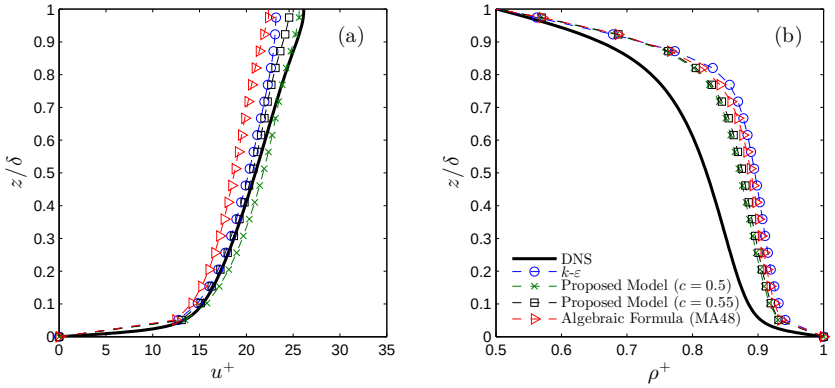

FIGURE 6.5. Channel flow results for $Re_\tau = 550$ and $Ri_\tau = 60$ with the Pr_t of Venayagamoorthy and Stretch (2010). Vertical profiles for (a) non-dimensional velocity, u^+ and (b) non-dimensional density, ρ^+ compared with DNS data of García-Villalba and del Álamo (2011).

6.5.2. EKMAN LAYER FLOW. The proposed model with $c = 0.55$ also preforms remarkably well for the case of Ekman layer flow seen in figures 6.10 and 6.11. The Pr_t of

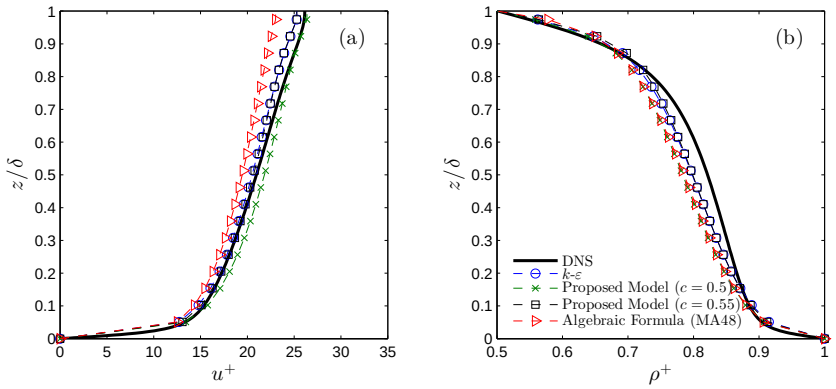

FIGURE 6.6. Channel flow results for $Re_\tau = 550$ and $Ri_\tau = 60$ with the Pr_t of Karimpour and Venayagamoorthy (2014b). Vertical profiles for (a) non-dimensional velocity, u^+ and (b) non-dimensional density, ρ^+ compared with DNS data of García-Villalba and del Álamo (2011).

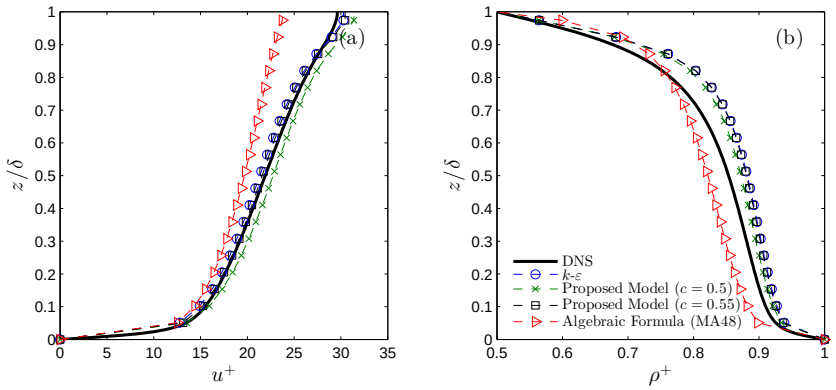

FIGURE 6.7. Channel flow results for $Re_\tau = 550$ and $Ri_\tau = 120$ with $Pr_t = 0.74$. Vertical profiles for (a) non-dimensional velocity, u^+ and (b) non-dimensional density, ρ^+ compared with DNS data of García-Villalba and del Álamo (2011).

Venayagamoorthy and Stretch (2010) improves the potential temperature profile shown in figure 6.11 where $\Phi = (\overline{\theta} - \theta_\infty)/\theta_\infty$ and θ_∞ is the potential temperature at the upper surface. The algebraic formula of Nieuwstadt (1984) is highly dependent on an estimate for the boundary layer height, h which in this case in known *a priori*. For larger-scale planetary boundary layer flows, h is generally approximated by equation (3.30). The Pr_t of Karimpour and Venayagamoorthy (2014b) is excluded from the simulations of the Ekman layer

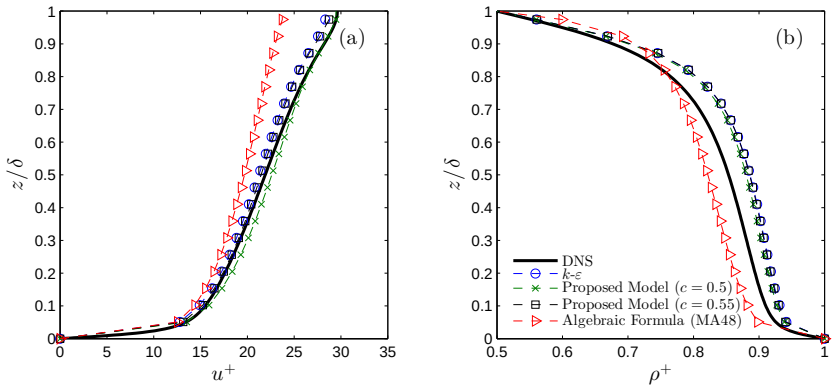

FIGURE 6.8. Channel flow results for $Re_\tau = 550$ and $Ri_\tau = 120$ with the Pr_t of Venayagamoorthy and Stretch (2010). Vertical profiles for (a) non-dimensional velocity, u^+ and (b) non-dimensional density, ρ^+ compared with DNS data of García-Villalba and del Álamo (2011).

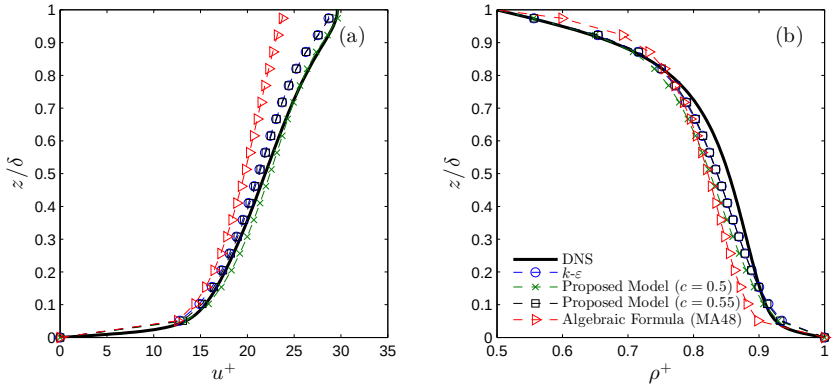

FIGURE 6.9. Channel flow results for $Re_\tau = 550$ and $Ri_\tau = 120$ with the Pr_t of Karimpour and Venayagamoorthy (2014b). Vertical profiles for (a) non-dimensional velocity, u^+ and (b) non-dimensional density, ρ^+ compared with DNS data of García-Villalba and del Álamo (2011).

because of its basis on the linear stress distribution from channel flow analysis. The stress distribution of a boundary layer flow is nonlinear (e.g. Pope, 2000). For the initial potential temperature profile in these simulations, an initial surface lapse rate is prescribed potentially eliminating the near-wall Pr_t number effects that $Pr_{t_{\mathrm{KV14}}}$ corrects.

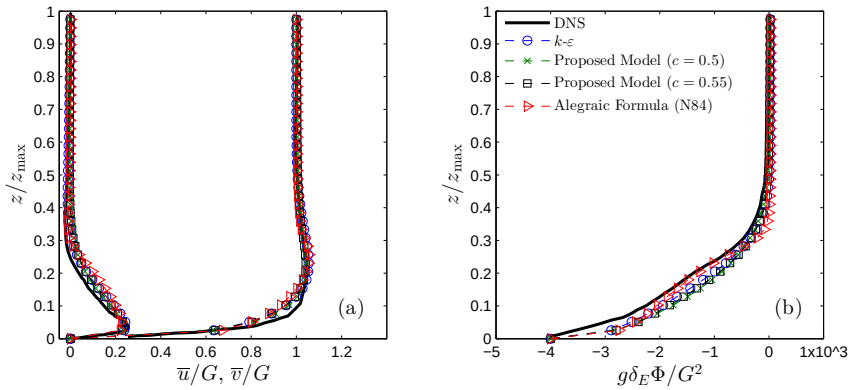

FIGURE 6.10. Ekman layer results for $Pr_t = 0.74$ at $tf = 1.8$. Vertical profiles for (a) non-dimensional velocity components, $\overline{u}/G$ and $\overline{v}/G$, and (b) non-dimensional potential temperature, $g\delta_E\Phi/G^2$ compared with digitized DNS data of Coleman et al. (1992).

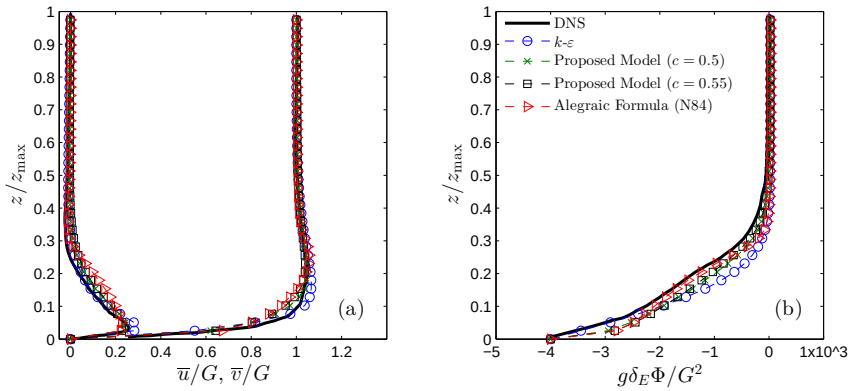

FIGURE 6.11. Ekman layer results for $Pr_{t_{\mathrm{VS10}}}$ at $tf = 1.8$. Vertical profiles for (a) non-dimensional velocity components, $\overline{u}/G$ and $\overline{v}/G$, and (b) non-dimensional potential temperature, $g\delta_E\Phi/G^2$ compared with digitized DNS data of Coleman et al. (1992).

6.6. CONCLUSIONS

The research presented in this chapter illustrates the capabilities of the proposed L_{kS}-based model parameterizations. The results suggest the implemented hybrid model is as capable as the standard k-ε for the cases of stably stratified channel and Ekman layer flows. The parameterization for eddy viscosity is developed from the highly energetic SABL flows

presented in chapter 5 but perform equally well for moderate Re flows with the slight modification of $c = 0.55$. An accurate model of stably stratified turbulence is clearly not as simple as a specification of eddy viscosity. The turbulent Prandtl number is central to the diffusivity of the density or temperature field and subsequent effects on the velocity field. A key question in this study is whether or not there is a component of energetics missing from R_f and Pr_t formulations? Can R_f and Pr_t simply be cast as functions of Ri or must Re be an explicit factor? Likewise, is κ_t dependent upon flow energetics? Such research would extend well beyond the pages of this dissertation; however, a further investigation on the influence of energetics on the eddy diffusivity is needed.

Overall, chapter 6 begins the process of developing a robust model framework for simulating stably stratified turbulence. Further validation is required scaling up to higher Re flows such as the GABLS model intercomparison cases (e.g. Cuxart et al., 2006). In extending this model, diligence is required in selection of proper rough-wall boundary conditions. The hybrid model framework with prognostic equations for k and ε is appealing because of the dynamic nature of ε as opposed to an algebraic specification. If implemented in a regional (or larger) scale operational model, the additional prognostic equation for ε may be undesirable. As such, a purely one-equation k-closure model will also be fully explored. Upon validation, this model could be easily implemented in global circulation or national weather prediction (NWP) models such as the weather research and forecasting (WRF) model. WRF provides idealized cases that could be used for further validation as well as the necessary links to provide "real-world" simulations.

Furthermore, there has been extensive development in linking WRF to OpenFOAM in recent years (e.g. Srinivasan and Papavassiliou, 2011; Mirocha et al., 2014). This link allows

for accurate computational fluid dynamics (CFD) simulations to be assessed on a smaller scale within the context of a regional or global simulation. To begin, wind turbine models must first be evaluated for their efficacy in predicting downstream wake characteristics and computational requirements. The flow near and downstream of a turbine rotor is far more complicated even under neutral stratification than the boundary layer flows considered in this chapter. Thus, to begin the analysis of wind turbine interactions in the atmospheric boundary layer, chapter 7 presents research pertaining to three turbine models evaluated under neutrally stratified conditions.

CHAPTER 7

Modeling Wind Turbine Interactions in the Atmospheric Boundary Layer[1]

7.1. Introduction

As wind turbines reach higher into the atmosphere with increasing rotor diameters and wind farms expand beyond 20 km in length, understanding the flow dynamics imposed by the atmospheric boundary layer (ABL) and local turbine wake interactions becomes an essential part of wind farm design and optimization. Wakes not only decrease the downstream mean velocity and corresponding power production but increase turbulent fluctuations leading to structural fatigue issues. Field observations provide valuable data but can only be collected from existing sites. Laboratory studies yield *a priori* information but are limited to moderate Reynolds number flows and cannot replicate large mesoscale motions. Computational fluid dynamic (CFD) analysis has become an important tool in the study of ABL flow dynamics and wind engineering allowing unprecedented studies of wind turbine wake dynamics and interactions (e.g. Meyers and Meneveau, 2012; Porté-Agel et al., 2011; Calaf et al., 2010; Churchfield et al., 2010; Sørensen and Shen, 2002). As computational power continues to increase and numerical techniques are refined, CFD will be at the forefront of wind turbine design and wind farm layout.

The high Reynolds numbers of ABL flows (e.g. $10^7 - 10^9$) dictate that spatial or temporal closure schemes be used to handle turbulence either through large-eddy simulations

[1]The research presented in this chapter represents a publication in the *Journal of Solar Energy Engineering* entitled "Comparisons of horizontal-axis wind turbine wake interaction models" (Wilson et al., 2014, *doi:10.1115/1.4028914*). This work represents a collaborative effort with Cole J. Davis, Dr. Subhas K. Venayagamoorthy, and Dr. Paul R. Heyliger. The full rotor model simulations were performed by Cole J. Davis as part of his masters thesis research (Davis, 2011).

(LES) or Reynolds-Averaged Navier-Stokes (RANS) simulations, respectively. Direct numerical simulation (DNS) of the Navier-Stokes equations remains limited to moderately low Reynolds numbers and simple geometries. LES provides resolution of large turbulent scales but relies on less accurate subgrid-scale (SGS) models for modeling smaller turbulent scales. LES requires considerable computational resources especially when scaling to multiple turbines and wind farms. On the other hand, RANS simulations apply temporal filtering to the governing Navier-Stokes equations providing an averaged flow field based on turbulence closure assumptions requiring significantly less computational time. The k-ε turbulence model Jones and Launder (1972) is perhaps the most widely used RANS model for engineering flows in research communities and industry, but most notably fails to accurately capture severely separated flows with adverse pressure gradients. Literature suggests that appropriate modifications (e.g. wall functions and boundary conditions consistent with field data and laboratory experiments) to the k-ε scheme provide accurate simulations of ABL flow and horizontal-axis wind turbine (HAWT) wake dynamics (Parente et al., 2011a; Réthoré, 2009; Vermeer et al., 2003). The favorable behavior of the k-ε model in the free stream has been incorporated into other various RANS turbulence models through blending functions. One such model is the k-ω SST model (Menter, 1994) combining the k-ω model (Wilcox, 1988) in the near-wall region and the k-ε model in the free-shear region.

In order to study the dynamics of large wind turbines, the NREL 5MW reference turbine is selected (Jonkman et al., 2009). While this turbine was developed as a theoretical tool for studying power production and structural responses in large wind turbines, the blade geometry is appropriate for fluid dynamic analysis. The accurate depiction of HAWTs in a computational model is essential. An actuator disk model (ADM) is one of the simplest

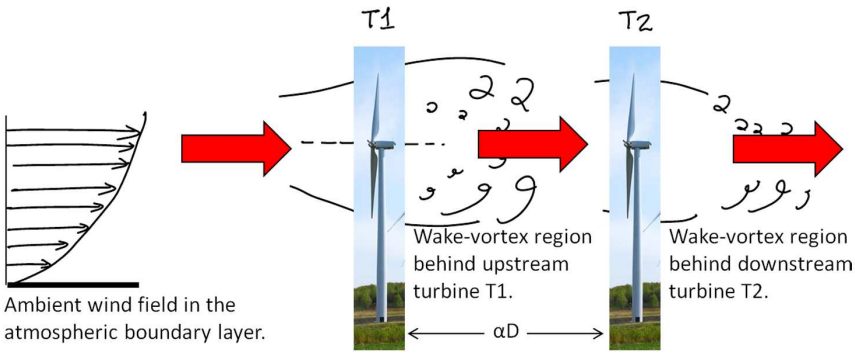

FIGURE 7.1. Schematic of two inline turbines

representations of a turbine rotor applying a uniform integration of rotor forces to the computational domain (Sørensen and Myken, 1992; Madsen, 1996). Increasing in sophistication, actuator line models (ALMs) include non-uniform rotor forces integrated along discrete lines, rotational effects, and tip vortices. Full rotor models (FRMs) give a three-dimensional rotor representation to investigate blade aerodynamics, near-wake dynamics, and power production (Sørensen and Shen, 2002). In this study, a comparison of wake dynamics for ADM, ALM, and FRM rotor representations of the NREL 5MW reference turbine are explored. To further understanding on dynamic loading of very large turbine blades, a high resolution full rotor model is analyzed to highlight the pressure distributions on blade surfaces. Finally, simulations of two inline turbines spaced 5 diameters ($5D$) apart are performed to investigate wake interaction dynamics. Figure 7.1 provides a schematic of the two inline turbines. The objective of this study is to further understand the development and resolution of turbine wakes using ADM, ALM, and FRM methods applicable to optimization of power production and fatigue load minimization.

In the following, a brief theoretical overview of the numerical methods, simulations, and rotor models is provided in Section 2. Section 3 presents the results of numerical simulations comparing single ADM, ALM, and FRM methods, pressure distributions on

turbine blades for a high resolution FRM, and two-inline turbine models spaced at $5D$. Results are thoroughly discussed in Section 4, providing a better understanding of wake interaction for large wind turbines and turbine blade loading.

7.2. Theory

This section is meant to highlight the turbulence closure models used in this study for neutral ABL flow. In the Reynolds-averaging process, an additional term is added to the momentum equation referred to as the Reynolds stress term ($-\overline{u_i' u_j'}$). Turbulence closure schemes use the turbulent-viscosity hypothesis to define the Reynolds stresses given by equation (7.1).

$$-\overline{u_i' u_j'} = \nu_t \left(\frac{\partial \overline{U}_i}{\partial x_j} + \frac{\partial \overline{U}_j}{\partial x_i} \right) - \frac{2}{3} k \delta_{ij}, \tag{7.1}$$

where $\overline{U}_{i,j}$ is the mean velocity field (individual velocity components are given by $\overline{u}$ in the x-direction (streamwise), $\overline{v}$ in the y-direction (spanwise), and $\overline{w}$ in the z-direction (vertical)), k is the turbulent kinetic energy, δ_{ij} is the Kronecker delta function, ν_t is the turbulent viscosity, and $\left(\partial \overline{U}_i / \partial x_j + \partial \overline{U}_j / \partial x_i\right)$ is twice the mean strain rate tensor ($\overline{S}_{ij}$). The turbulent viscosity is commonly solved through an algebraic combination of velocity and length scales ($\nu_t \sim u^* l^*$). These scales can be solved using a myriad of methods ranging in complexity from zero-equation models to Reynolds-stress models. This study focuses on the two-equation k-ε and k-ω SST turbulence closure schemes described in the following subsections.

7.2.1. Standard k-ε Model.

The standard k-ε model (Jones and Launder, 1972) is a two-equation closure model based on the exchanges between turbulent kinetic energy (k) and the dissipation rate of the turbulent kinetic energy (ε). This model is widely used for simulation of engineering and geophysical flows including HAWT interactions in the neutrally

stratified ABL (Balogh et al., 2012; Parente et al., 2011a,b; Kasmi and Masson, 2008; Rodi, 1987). This model is used for simulations of actuator disk and line models. The governing transport equations for k and ε are given by equations (7.2) and (7.3), respectively.

$$\frac{\bar{D}k}{\bar{D}t} = \frac{\partial}{\partial x_j}\left[\left(\nu + \frac{\nu_t}{\sigma_k}\right)\frac{\partial k}{\partial x_j}\right] + P_k - \varepsilon, \tag{7.2}$$

$$\frac{\bar{D}\varepsilon}{\bar{D}t} = \frac{\partial}{\partial x_j}\left[\left(\nu + \frac{\nu_t}{\sigma_\varepsilon}\right)\frac{\partial \varepsilon}{\partial x_j}\right] + C_{\varepsilon 1}\frac{\varepsilon}{k}P_k - C_{\varepsilon 2}\frac{\varepsilon^2}{k}, \tag{7.3}$$

where ν is the molecular viscosity, $P_k = 2\nu_t \overline{S}_{ij}\overline{S}_{ij}$ is production of turbulent kinetic energy, $\sigma_k = 1.3$ is the Prandtl number for k, $\sigma_\varepsilon = 1.0$ is the Prandtl number for ε, and $C_{\varepsilon 1} = 1.44$ and $C_{\varepsilon 2} = 1.92$ are model constants that are assigned their standard values (Launder and Spalding, 1974). The turbulent viscosity is given by

$$\nu_t = C_\mu \frac{k^2}{\varepsilon}, \tag{7.4}$$

where C_μ is a model coefficient with a standard value of 0.09 (Launder and Spalding, 1974).

Numerous modifications have been suggested in literature for the standard k-ε model in ABL applications. Crespo et al. (1985) used $C_\mu = 0.03$ to reduce excessive model dissipation. Additionally, Kasmi and Masson (2008) suggested an extended k-ε model for flow through HAWTs improving on the simple modification of Crespo et al. (1985). Furthermore, Gorlé et al. (2009) and Parente et al. (2011a,b) added additional source terms to the transport equations for k and ε and cast $C_\mu = u_*^4/k(z)^2$ as a function of height. $u_* = \sqrt{\tau_w/\rho}$ is the shear velocity and τ_w is the shear stress at the surface. Obviously, there is yet to be a consensus for proper modification of the standard k-ε model in ABL applications which becomes further complicated in the presence of stratification. Stratification introduces buoyant forces that

influence mixing and transport processes of turbulent flows (see e.g. Rodi, 1987). Future research will consider modifications to the k-ε model but the current work uses the standard formulation along with the consistency condition for the turbulent Prandtl number of ε (Wilcox, 1993; Hargreaves and Wright, 2007).

$$\sigma_\varepsilon = \frac{\kappa^2}{(C_{\varepsilon 2} - C_{\varepsilon 1})\sqrt{C_\mu}}, \tag{7.5}$$

where κ is the von Kármán constant ($\kappa = 0.4$). For $C_\mu = 0.09$, equation (7.5) results in $\sigma_\varepsilon = 1.11$ instead of the standard value of 1.3 (Launder and Spalding, 1974).

7.2.2. k-ω SST Model. The k-ω SST turbulence closure model (Menter, 1994) is used for the full rotor simulations due to its aptitude for simulation of near-wall viscous effects, separated flows, and free-stream conditions (Menter, 2009). The governing transport equations for turbulent kinetic energy (k) and specific dissipation of turbulent kinetic energy (ω) are given by equations (7.6) and (7.7), respectively.

$$\frac{\bar{D}k}{\bar{D}t} = \frac{\partial}{\partial x_j}\left[\left(\nu + \frac{\nu_t}{\sigma_k}\right)\frac{\partial k}{\partial x_j}\right] + \tilde{P}_k - Y_k, \tag{7.6}$$

$$\frac{\bar{D}\omega}{\bar{D}t} = \frac{\partial}{\partial x_j}\left[\left(\nu + \frac{\nu_t}{\sigma_\omega}\right)\frac{\partial \omega}{\partial x_j}\right] + P_\omega - Y_\omega + D_\omega, \tag{7.7}$$

where $\sigma_k = 1/[F_1/\sigma_{k,1} + (1 - F_1)/\sigma_{k,2}]$, $\tilde{P}_k = \min(P_k, 10\beta^* k\omega)$ represents the production of turbulent kinetic energy, $Y_k = \beta^* k\omega$ is the dissipation of turbulent kinetic energy, $\sigma_\omega = 1/[F_1/\sigma_{\omega,1} + (1 - F_1)/\sigma_{\omega,2}]$ is the Prandtl number for ω, $P_\omega = \alpha\omega P_k/k$ is the production of specific dissipation of turbulent kinetic energy, $\alpha = \alpha_1 F_1 + \alpha_2(1 - F_1)$ is a blending function, $Y_\omega = \beta\omega^2$ is the dissipation of specific dissipation of turbulent kinetic energy, $\beta = F_1\beta_{i,1} + (1-F_1)\beta_{i,2}$ is blending function for specific dissipation, and $D_\omega = 2(1-F_1)\sigma_{\omega,2}\frac{1}{\omega}\frac{\partial k}{\partial x_j}\frac{\partial \omega}{\partial x_j}$

TABLE 7.1. k-ω SST model constants

α^*_∞	α_∞	β^*_∞	a_1	$\beta_{i,1}$	$\beta_{i,2}$	$\sigma_{k,1}$	$\sigma_{k,2}$	$\sigma_{\omega,1}$	$\sigma_{\omega,2}$
1.0	0.52	0.09	0.31	0.075	0.0828	1.176	1.0	2.0	1.168

is the cross-diffusion term. F_1 is a blending function equal to zero away from the surface ($k-\varepsilon$ model) and one in the surface boundary layer ($k-\omega$ model). The turbulent viscosity for the k-ω SST model is given by

$$\nu_t = \frac{k}{\omega}\frac{1}{\max\left(\frac{1}{\alpha^*}, \frac{SF_2}{a_1\omega}\right)}, \tag{7.8}$$

where $\alpha^* = \alpha^*_\infty[(\alpha^*_0 + Re_t/R_k)/(1+Re_t/R_k)]$ is a damping function for low-Reynolds number correction and F_2 is a second blending function. In the near wall region the $SF_2/a_1\omega$ term is dominant and in the free stream the $1/\alpha^*$ term is dominant. Table 7.1 presents the standard model constants for the k-ω SST model. This section highlights the major transport equations and terms in the k-ω SST model. Menter (1994) provides a thorough explanation of the k-ω SST model and numerous blending functions in the turbulence model formulation.

7.2.3. NUMERICAL FRAMEWORK. This study focuses on the influence of very large wind turbine interactions leading to the selection of the NREL 5MW reference turbine for simulations (Jonkman et al., 2009). While the turbine was intended for theoretical dynamic structural and drivetrain research for offshore wind turbines, it has been used in CFD studies as well (Sørensen and Johansen, 2007; Churchfield et al., 2010; Tossas and Leonardi, 2013). This study used two different CFD software packages: OpenFOAM 2.1.0. and ANSYS Fluent 13.0.

The finite-volume code OpenFOAM (Open-source Field Operations and Manipulations) is a set of C++ libraries solving differential equations of the flow equations using the finite-volume method for unstructured meshes and is highly parallelizable through the message passing interface (MPI) (OpenCFD, 2012). The SIMPLE (Semi-Implicit Method for Pressure-Linked Equations) algorithm was used for steady-state simulations of the actuator disk models. Transient simulations of the actuator line models used the PISO (Pressure Implicit with Splitting of Operators) algorithm. Spatial discretizations were set to Gauss linear for gradient and divergence terms and Gauss linear corrected for Laplacian terms. First-order implicit Eularian discretization was used for temporal terms in the ALM model simulations.

Fluent 13.0 is a commercially available finite-volume CFD simulator with a built-in post-processor (ANSYS, 2010). The code is adaptable through user-defined functions (UDFs), but there is no direct access to the source code which leads to some ambiguity in implementation of modifications. Fluent was used for the fully resolved turbine rotor model case using a sliding mesh method. Transient solutions again used the PISO algorithm with second-order accuracy in temporal and spatial discretizations.

The computational domain was sized $2D$ (252 m) upstream of the turbine, $20D$ (2520 m) downstream of the first turbine, $2.5D$ (315 m) spanwise on either side of the turbines, and 378 m in height, where D is the rotor diameter. The total domain was 2772 x 630 x 378 m. Considering the relatively small domain size in the performed simulations Coriolis effects can be neglected leaving the driving boundary conditions and surface roughness as the primary influences on the boundary layer. The domain size was sufficient to not encounter boundary effects in the flow and allow downstream wake observation. The turbine models were placed

at the hub height of 90 m. A grid independence study was performed to ensure solution independence for each of the rotor models, ADM, ALM, and FRM, respectively.

7.2.4. Boundary Conditions. The fully-developed inlet profiles of mean streamwise velocity ($\overline{u}$), turbulent kinetic energy (k), and dissipation rate turbulent kinetic energy (ε) of Richards and Hoxey (1993) were applied at the domain inlet in simulations.

$$\overline{u}\left(z\right) = \frac{u_*}{\kappa} \ln\left(\frac{z + z_0}{z_0}\right), \tag{7.9}$$

$$k = \frac{u_*^2}{\sqrt{C_\mu}}, \tag{7.10}$$

$$\varepsilon(z) = \frac{u_*^3}{\kappa\left(z + z_0\right)}, \tag{7.11}$$

where z_0 is the aerodynamic roughness length. Equations (7.9-7.11) are analytical solutions to the standard k-ε model if the Prandtl number for ε is defined by equation (7.5)(Hargreaves and Wright, 2007). Equations (7.9) and (7.11) are standard boundary conditions for $\overline{u}$ and ε. The boundary condition for k is specified as a fixed value given by equation (7.10). A UDF was compiled in Fluent to implement the inlet conditions for $\overline{u}$, k, and ε. The domain outlet was specified as pressure outlet with a constant value of 0 Pa (gage). The top and side (front and back) surfaces of the computational domain were assigned a slip condition. A slip condition ensures zero-gradient ($\partial/\partial n$) for scalar quantities. For vector quantities, the normal component is set to zero and tangential components are assigned zero-gradient.

Figure 7.2 depicts the vertical profiles of mean streamwise velocity and turbulent kinetic energy for an empty domain using the prescribed boundary conditions. The mean velocity profile is maintained and the TKE does not exhibit a strong peak near the wall surface. A

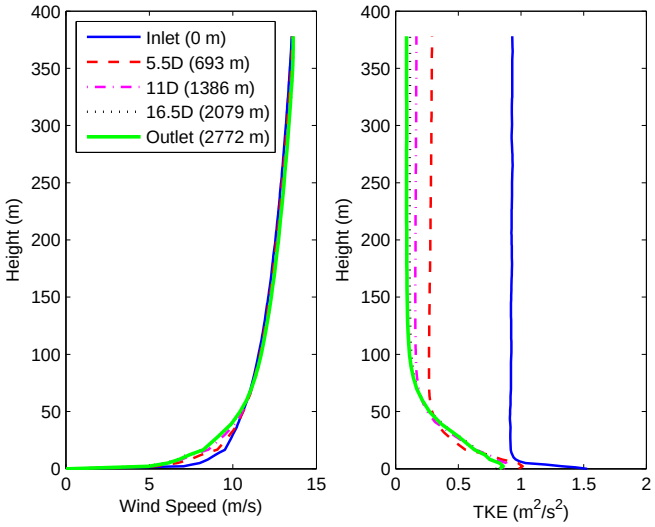

FIGURE 7.2. Vertical profiles of mean streamwise velocity (left) and turbulent kinetic energy (right)

vertical gradient (wall-normal coordinate) of TKE is consistent with the numerical simulations of the neutral ABL (Yang et al., 2009; Parente et al., 2011a,b). However, maintaining the inlet TKE profile for the neutral ABL is a well documented difficulty and active area of research in the RANS framework (Richards and Hoxey, 1993; Spalart and Rumsey, 2007). Overall, resolution of the mean velocity profile is of primary importance for the comparison of HAWT models which is achieved prior to incidence with the upstream turbine.

7.2.5. WALL FUNCTIONS. The bottom (or ground) surface in the domain was treated as a fully aerodynamically rough wall. Wall functions are employed due to the high Reynolds number of ABL flow rather than resolving the scales near the wall. Wall-resolving models require very fine mesh resolution and are not practical due to high computational costs. The velocity and turbulent dissipation rate are defined at the first cell centroid, z_p, using the formulation of Richards and Hoxey (1993) as

$$\overline{u}_P = \frac{u_*}{\kappa} \ln\left(\frac{z_p + z_0}{z_0}\right), \tag{7.12}$$

$$\varepsilon_P = \frac{C_\mu^{3/4} k^{3/2}}{\kappa \left(z_P + z_0\right)}, \tag{7.13}$$

where the subscript $_P$ denotes the value at the first grid point. The mean streamwise velocity at the first grid point is enforced by relating the shear stress over the wall-adjacent cell to the wall shear stress (τ_w).

$$\tau_w = \rho u_*^2 = \rho C_\mu^{1/4} \kappa k^{1/2} \frac{\overline{u}_P}{\ln\left(\frac{z_p + z_0}{z_0}\right)}, \tag{7.14}$$

where $u_* = C_\mu^{1/4} k^{1/2}$ is the shear velocity defined using the local equilibrium assumption. Assuming that the shear production at the wall is given by $P_k \approx \tau_w(\partial\overline{u}/\partial z)$, the velocity derivative is given by

$$\left(\frac{\partial \overline{u}}{\partial z}\right)_P = \frac{C_\mu^{1/4} k_P^{1/2}}{\kappa \left(\frac{z_p + z_0}{z_0}\right)} \tag{7.15}$$

Using the relationship between wall shear stress and velocity gradient over the wall-adjacent cell is a more robust condition for turbulence models than directly applying equation (7.12) (Ferziger and Milovan, 1996). The wall boundary condition for k is set to a zero-gradient in the normal direction.

$$\left(\frac{\partial k}{\partial n}\right)_w = 0 \tag{7.16}$$

Equations (7.13), (7.15), and (7.16) are enforced as boundary conditions for ε, $\overline{u}$, and k, respectively, in OpenFOAM and Fluent.

7.2.6. Wind Turbine Models. Wind turbine computational models vary in levels of sophistication, but all are based on the principle of momentum extraction from the fluid stream. Actuator disk and line models are generally used to determine the influence of a wind turbine on the ABL and wake dynamics while full rotor models determine loads on

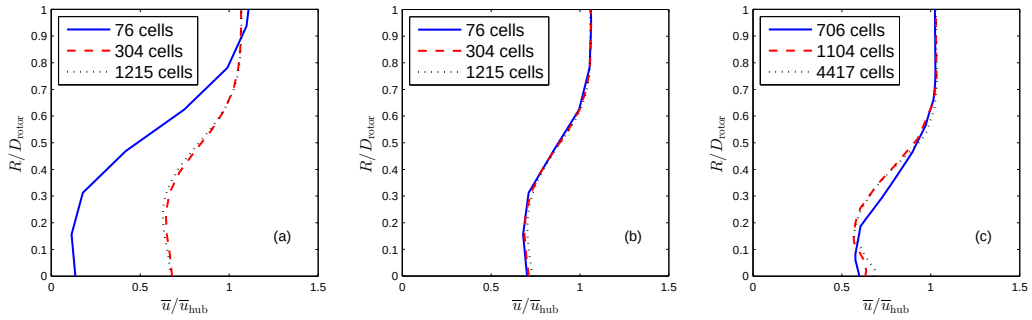

FIGURE 7.3. Grid independence study for a) ADM, b) ALM, and c) FRM rotor models. Mean streamwise velocity ($\overline{u}$) is measured $0.5D$ downstream. The number of cells is calculated over a circular region centered at the rotor hub with a diameter of 150 m (coinciding with the sliding mesh surface of the FRM).

turbine structures and power production. Rated conditions were specified for all turbine models with a wind speed of 11.4 m/s at 90 m hub height correlating to a rotor speed of 12.1 rpm at a pitch angle of 0.0° (Jonkman et al., 2009). Figure 7.3 presents the results from a grid independence study of the individual rotor models.

7.2.6.1. *Actuator Disk Model.* Actuator disk theory replaces the rotor of a HAWT with a representative disk upon which blade forces are distributed. This simplification allows for a computational model without the need for a highly resolved mesh in the region of the turbine to accurately capture the boundary layer effects along the blades. Development of actuator disk methods are further described by Madsen (1996), Sørensen and Kock (1995), and Sørensen and Myken (1992). The essential quantities in this formulation are thrust (T), power (P), and torque (Q), described in equations (7.17-7.19), respectively.

$$T = \frac{\rho V_0^2}{2} \pi R^2 C_T, \tag{7.17}$$

$$P = \frac{\rho V_0^3}{2} \pi R^2 C_P, \tag{7.18}$$

$$Q = \frac{P}{\Omega}, \tag{7.19}$$

where V_0 is the freestream velocity, R is the rotor radius, C_T is the turbine thrust coefficient, C_P is the turbine power coefficient, and Ω is the turbine rotational speed. Equations (7.20) and (7.21) prescribe the volume integral for thrust and torque of the actuator disk.

$$T = \int_V f_{bx}\ dV, \tag{7.20}$$

$$Q = \int_V f_{b\theta}\ dV, \tag{7.21}$$

where f_{bx} is the body force in the axial direction and $f_{b\theta}$ is the body force in the tangential direction.

For the NREL 5MW reference turbine, C_T and C_P are set to 0.6 and 0.5, corresponding to typical operating conditions. The disk radius is 63 m. The center of the actuator disks is located 252 m downstream of the inlet boundary for a single turbine and 252 m and 882 m for two turbines spaced $5D$ apart. The computational domain was meshed to 128 x 128 x 256 using the meshing utility `blockMesh` in OpenFOAM. The mesh was clustered in the streamwise direction where the actuator disks were placed. The resolution provided convergence of results and a reasonable computation time. Residuals of relevant flow and turbulent quantities were monitored for solution convergence. The actuator disk model allows for steady-state computations given the uniform force distributions.

7.2.6.2. *Actuator Line Model.* Actuator line models allow for discretized wind turbine blades to be represented as compact lines of body forces. A significant advantage is that tip vortices can be captured with the actuator line model. The most widely used adaptation of this technique was developed by Sørensen and Shen (2002) and will be used in this research

as implemented by Churchfield et al. (2012b) in NREL's SOWFA (Simulator for Offshore Wind Farm Applications) solver set for OpenFOAM. Similar to the actuator disk model, the actuator line model does not depict the nacelle or tower.

This model also has the ability to be dynamically controlled, responding to changes in the incoming flow field. For a RANS simulation this feature is not essential, but is desirable when moving to a higher order simulation such as LES. The velocity magnitude and local flow angle can be computed for each of the segments on the actuator line based on airfoil type, chord, twist, and local flow velocity. Assuming the effects of up- and downwash are small from lift, the magnitude of lift and drag can be computed from airfoil lookup tables as follows.

$$L = \frac{1}{2} C_l \alpha \rho V_0^2 c w, \tag{7.22}$$

$$D = \frac{1}{2} C_d \alpha \rho V_0^2 c w, \tag{7.23}$$

where C_l is the lift coefficient, C_d is the drag coefficient, α is the induction factor, c is the chord length, and w is the actuator line segment length. From Sørensen and Shen (2002), the actuator line forces are projected onto the computational domain as a body force field using a Gaussian projection given by

$$F_i^T(x, y, z, t) = -\sum_{j=1}^{N} f_i^T(x_j, y_j, z_j, t) \frac{1}{\epsilon^3 \pi^{3/2}} \exp\left[-\left(\frac{|\overline{r}_j|}{\epsilon} \right)^2 \right], \tag{7.24}$$

where ϵ controls the width of the Gaussian projection and its specification is analyzed in detail by Martinez et al. (2012). Churchfield et al. (2012b) discuss the numerical framework for their implementation of the Sørensen and Shen (2002) actuator line model. The computational domain was meshed to 128 x 128 x 256 using the meshing utility `blockMesh` in OpenFOAM

clustered in the regions of turbine placement. Grids were refined to 1 m in the streamwise direction and sufficiently fine to have at least 20 cells over the turbine area. This resolution provided convergence of results and a reasonable time based on the recommendations for sufficient grid resolution (Churchfield et al., 2012b). Again, residuals of relevant flow and turbulent quantities were monitored for solution convergence.

7.2.6.3. *Full Rotor Turbine Model.* The full rotor model of the NREL 5M reference turbine was created in SolidWorks to the specifications of Jonkman et al. (2009) for rated conditions. This geometry was exported into ANSYS DesignModeler, where the domain geometry was created. A cylindrical domain 150 m in diameter and 20 m in thickness encapsulating each turbine rotor was created to allow for sliding mesh computations. Meshing was performed in ANSYS using an unstructured tetrahedral mesh. Cell sizes were set to 1 m on the blade surfaces and hubs and 0.5 m on the blade tips. Cells were kept to a maximum size of 15 m in the horizontal direction and 10 m in the vertical direction. Inflation layers were implemented on all solid surfaces with a maximum growth rate of 1.2. The front and back faces of the rotating domains were constrained to 7 m cell sizes and the circular surfaces of the rotating domains were restricted to 4 m cell sizes. With these restrictions, the FRM contained approximately 2.15 million cells. Figure 7.4 shows the meshed domains for the FRM. Models were run as transient simulations until they reached a quasi-steady state (approximately 10 minutes in real flow time) with convergence of residuals.

7.3. Results and Discussion

This section discusses the results from single turbine simulations of ADM, ALM, and FRM models and compares streamwise velocity profiles for the NREL 5MW reference turbine. These simulations illustrate the physics of wake formation and resolution for different

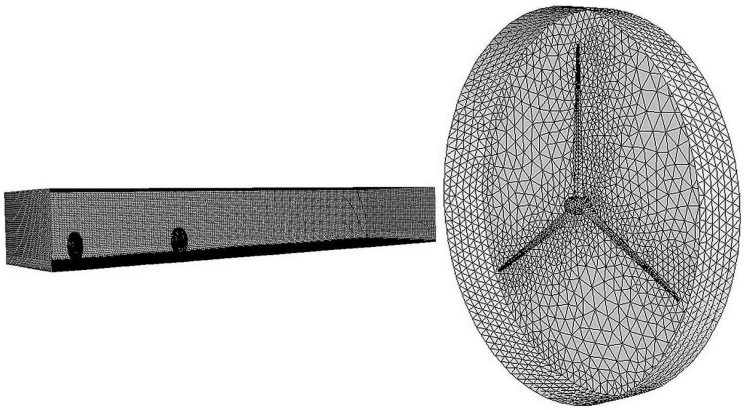

FIGURE 7.4. Computational grid for FRM simulations of two turbines with $5D$ spacing (left) and grid of a sliding mesh domain for a turbine rotor enclosed (right).

models. A high-resolution FRM model is simulated for analysis of blade pressure distributions. Finally, two inline turbines spaced $5D$ (630 m) apart were simulated using ADM, ALM, and FRM. These additional simulations further illustrate wake interaction and resolution.

7.3.1. SINGLE TURBINE SIMULATIONS. Figure 7.5 displays velocity contours for the single turbine simulations. Streamwise velocity profiles for the ADM, ALM, and FRM, respectively, are presented in figure 7.6. The velocity deficit is more pronounced for the FRM compared with ADM and ALM. The downstream wake recovers slightly faster for the ADM as compared to the ALM while the FRM velocity deficit persists throughout the domain. To further analyze the flow characteristics, contours of turbulence intensity ($I = u'/|\overline{U}|$) are displayed in figure 7.7. Within the RANS framework, the fluctuating velocities, u' are estimated by $u' = \sqrt{(2/3)k}$ and $|\overline{U}| = \sqrt{\overline{u}^2 + \overline{v}^2 + \overline{w}^2}$ is the magnitude of the three-dimensional velocity field. Behind a single turbine, the turbulence intensity is significantly more pronounced for ADM and ALM compared with FRM. This difference is attributed largely to the difference in k-ε and k-ω SST turbulence models. Notably, the

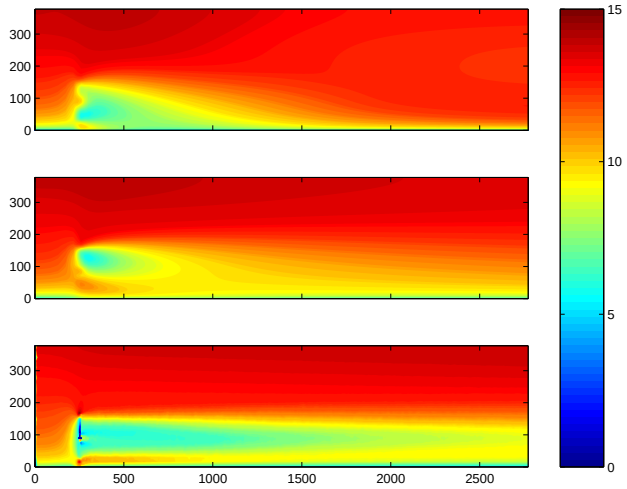

FIGURE 7.5. Contours of streamwise velocity (m/s) for single turbine models. ADM (Top), ALM (Center), FRM (Bottom).

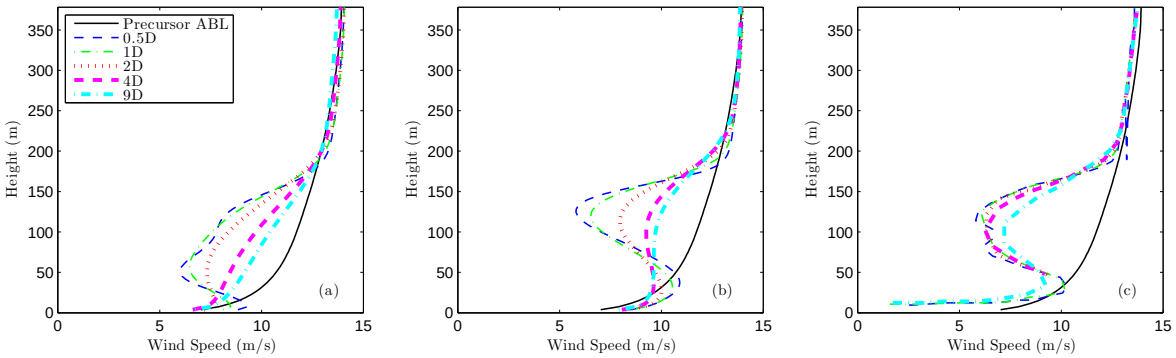

FIGURE 7.6. Comparison of downstream vertical profiles of streamwise velocity (m/s) for a) ADM, b) ALM, and c) FRM.

k-ε model overpredicts k in regions with adverse pressure gradients. However, these effects only have minor influences on the mean flow field which is of primary interest in a RANS framework.

Overall, results compare well qualitatively with literature for simulations of the NREL 5MW reference turbine (Tossas and Leonardi, 2013; Troldborg et al., 2011; Sørensen and Johansen, 2007). Wake effects for large wind turbines persist further downstream than standard wind farm spacings of $5D$ to $10D$ and may not be adequate for optimal performance

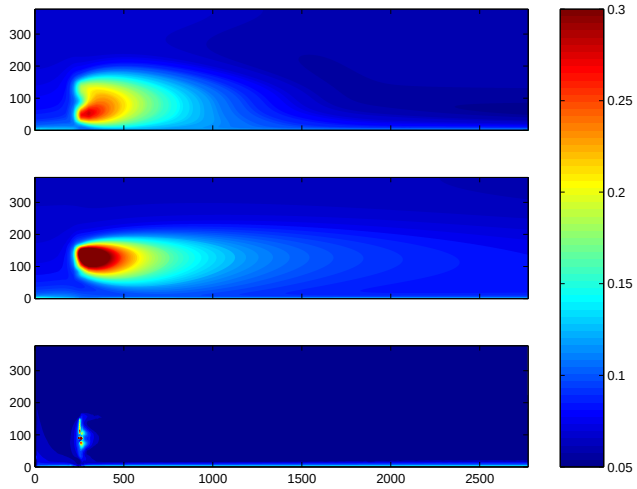

FIGURE 7.7. Contours of turbulence intensity for single turbine models. ADM (Top), ALM (Center), FRM (Bottom).

(Meyers and Meneveau, 2012). The contours and vertical profiles of streamwise velocity indicate a close comparison between the actuator disk and line models. It is well known that actuator disk and line models provide a more accurate representation of far-field wake effects compared with full rotor models (Tossas and Leonardi, 2013; Porté-Agel et al., 2011). Additionally, actuator disk and line models require significantly less computational time than a comparable full rotor model which becomes increasingly important when scaling simulations to numerous turbines in large wind farm settings. ADM and ALM simulations present a significant increase in the fidelity of wake prediction compared with empirical models (Stovall et al., 2010). Finally, the large blade diameter of the NREL reference turbine experiences greater shear forces under neutrally-stratified ABL conditions (an approximate difference of 2 m/s in incident wind velocity from the bottom to top of the rotor domain). When placed in an array of turbines, this shear and the additional wake effects can present significant structural concerns that are important to consider for evaluating fatigue related failures.

TABLE 7.2. FRM high-resolution grid sizing

Blade Face (m)	1	0.8	0.65	0.5	0.1
Blade Tip (m)	0.5	0.2	0.15	0.1	0.05
Rotating Domain Face (m)	7	5	4	4	2
Rotating Domain Cylinder (m)	4	4	4	4	2
Total Cells ($\times 10^6$)	0.789	0.951	1.09	1.27	5.43

7.3.2. HIGH-RESOLUTION FRM SIMULATIONS. To further the current study for large wind turbines, a high resolution FRM was simulated to analyze the pressure distributions on the blade surfaces. While the original converged computational grid was sufficient to capture flow dynamics, refinement is needed to investigate the surface (or near-wall) characteristics. A similar setup was carried out for the grid independence study of the high resolution FRM as with the single and two turbine simulations. For these models the domain included only one rotating turbine located $2D$ from the inlet and extended only $5D$ downstream of the turbine. The mesh sizes were varied on the turbine and rotating domain surfaces. Table 7.2 provides the mesh restrictions and model cell counts.

The results of this grid independence study were quite interesting. The FRM maximum pressure is nearly the same as the stagnation pressure calculated from the Bernoulli principle occurring along the leading edge of the blade shown in figure 7.8. The pressure exerted on the blades increases dramatically and levels off at the case of 1.09 million cells with a cell size of 0.65 m on the blade surfaces. This is a very small change from the previous case but with dramatic results. Although this maximum pressure can be approximated with the Bernoulli equation, the distribution of the pressure along the blade requires CFD simulation presented in figure 7.9. The maximum blade pressure in the single turbine simulation is found to be approximately 1.4 kPa which agrees well with the findings of Bazilevs et al. (2011a) and Bazilevs et al. (2011b) in their LES study which yielded a maximum pressure of

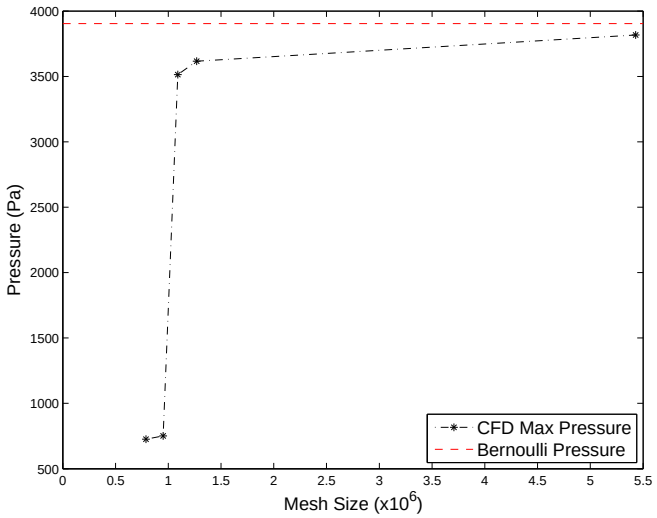

FIGURE 7.8. Grid independence study of maximum turbine blade pressure compared to the theoretical maximum Bernoulli pressure.

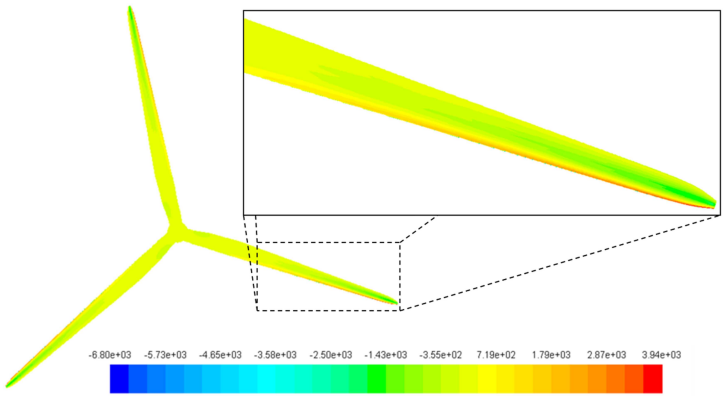

FIGURE 7.9. Contours of pressure (Pa) along blade surfaces

1.2 kPa. It is noted that their blade configuration was slightly altered from ideal operating conditions which can explain the difference in values. This distributed loading by pressure forces leads to significant torque and non-linear bending in the highly anisotropic turbine blade materials. These distributions suggest that investigation into non-linear beam effects should be pursued since they are likely to load the blade outside the limits of linear response. As wind speeds increase, the increased pitch response would lead to a redistribution of the blade pressures and further the need for investigation of non-linear beam mechanics.

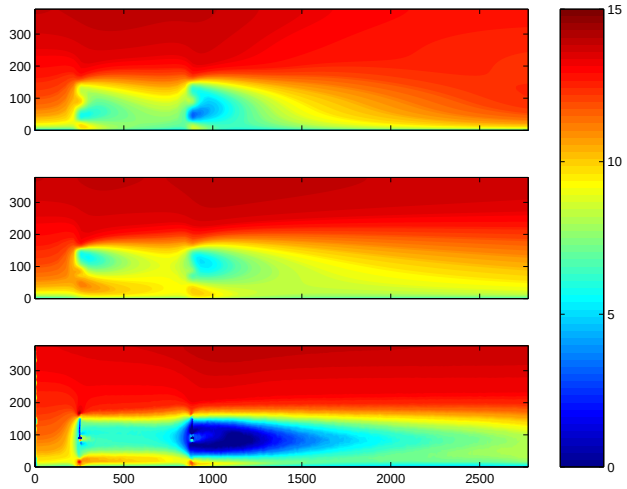

FIGURE 7.10. Contours of streamwise velocity (m/s) for inline turbines spaced $5D$ apart. ADM (Top), ALM (Center), FRM (Bottom).

7.3.3. INLINE TURBINE SIMULATIONS. An investigation of wake interactions was performed for two inline turbines spaced $5D$. Figure 7.10 displays the velocity contours. A clear increase in the downstream velocity deficit for the second turbine can be noticed for all three models. Figure 7.11 shows the vertical profiles of streamwise velocity $0.5D$ and $4D$ behind the first turbine (T1) and second turbine (T2). Both velocity contours and streamwise velocity profiles clearly illustrate ADM and ALM exhibit wake restoration in the computational domain. The FRM wake extends beyond the domain limits. The contours of turbulence intensity for the inline turbine models are shown in figure 7.12. There is a noticeable increase in the size and magnitude of the regions of turbulence intensity downstream of the second turbine. Behind the second FRM there is a significant region of turbulence intensity indicative of the onset of wake meandering effects increasing the turbulent kinetic energy (Churchfield et al., 2012b). Wake meandering can have significant effects on power production and fatigue loading especially in arrays with multiple rows of turbines.

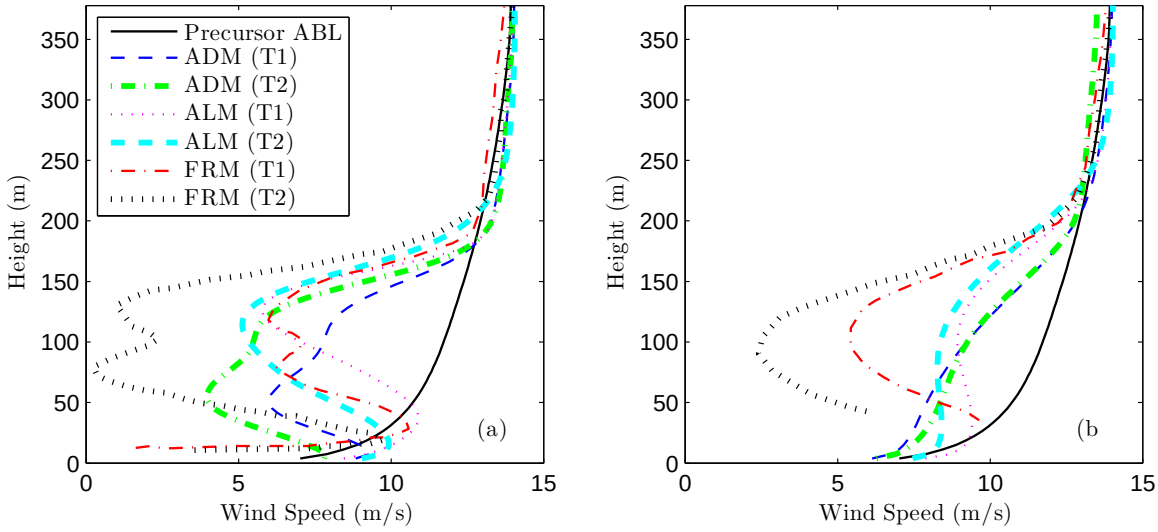

FIGURE 7.11. Comparison of downstream vertical profiles of streamwise velocity (m/s) for a) $0.5D$ downstream and b) $4D$ downstream for first and second turbines (T1 and T2, respectively).

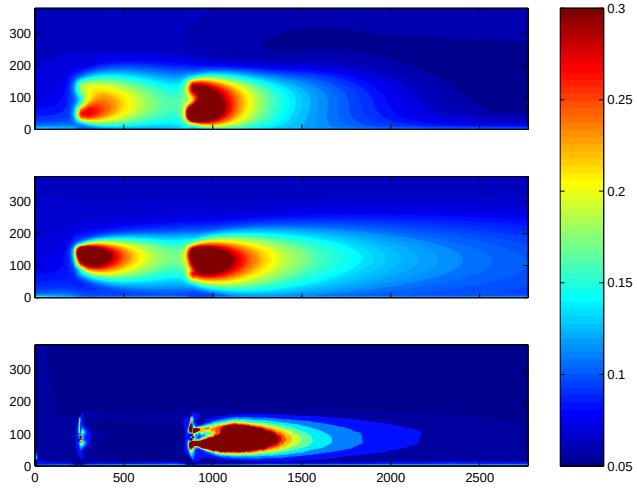

FIGURE 7.12. Contours of turbulence intensity for inline turbines spaced $5D$ apart. ADM (Top), ALM (Center), FRM (Bottom).

The simulations of inline turbine models reveal the strong interaction of turbine wakes when spaced only $5D$ apart. Again, the contours and vertical profiles of streamwise velocity show a good comparison between the actuator disk and line models. The FRM results are well outside of the magnitudes in ADM and ALM simulations again showing the weakness

of the FRM in far-wake field prediction. Downstream of the first turbine (T1), velocity and turbulence intensity fields closely resemble those of the single turbine simulations. Significant increases in velocity deficit reveal a strong decrease in the available energy for power production. The increase in turbulence intensity results from a corresponding increase in the turbulent fluctuations or analogously the turbulent kinetic energy. These fluctuations can induce strong peak loading on downstream turbines leading to structural concerns. Overall, results indicate that $5D$ spacing is inadequate for large wind turbines in neutrally-stratified conditions due to reduced power generation and increased fluctuating loads.

7.4. Conclusions

Several important findings resulted from this study of the NREL 5MW reference turbine. The single turbine simulations for actuator disk, actuator line, and full rotor models compared well qualitatively with literature for the NREL 5MW reference turbine (Tossas and Leonardi, 2013; Sørensen and Johansen, 2007) and similar large HAWT simulations (Porté-Agel et al., 2011; Vermeer et al., 2003). ADM and ALM results compared closely while the FRM exhibited a more sustained velocity deficit. Wake effects were observed beyond the typical spacing of $5D$ to $10D$ and warrants further investigation into the spacing of large wind turbines in arrays and wind farm settings. The k-ε model yields an increased turbulence intensity behind rotors, but ADM and ALM still represent an increase in wake prediction accuracy compared with empirical models (Stovall et al., 2010). A high-resolution study of a single FRM revealed interesting pressure distributions for a 0.0° pitch angle operating at the rated conditions. The maximum observed pressure was remarkably close to the calculated Bernoulli maximum pressure located on the leading edge of the blades. The pressure distributions suggest that the blades may be loaded beyond linear limits and require non-linear

beam mechanics to accurately quantify the blade behavior. Finally, wake interactions were observed for turbines spaced $5D$. Results suggest that this spacing would yield a significant reduction in power production from downstream turbines. The increase in turbulence intensity could also lead to serious fatigue loading. While the NREL 5MW reference turbine was used in this study to highlight the differences between the different turbine wake models, it provides a base model for simulations of large wind turbines. As turbines continue to grow in size, a stronger collaboration between the research community and industry is needed to better evaluate the physics not only involved in the interaction of the ABL on turbines and turbine-turbine interactions but also the influence of turbines on atmospheric dynamics.

Future research will investigate structural dynamics and aeroelastic effects of large wind turbine blades based on the obtained pressure distributions from the FRM. The potential of non-linear bending in blades constructed with anisotropic composite materials presents significant structural issues. Additionally, stably stratified ABLs will be considered. Stable stratification can introduce high shear rates, low-level jets, and wave motions in the ABL. These stable boundary layer effects lead to higher loads on blades and increased shear forces over the wind turbine rotor.

CHAPTER 8

Summary and Conclusions

8.1. Summary of Research

The research presented here focused on an analysis from DNS, LES, laboratory, and observational data to highlight the influence of energetics on stably stratified turbulence. This analysis provides a framework to develop and test parameterizations of turbulent mixing through theoretical and numerical endeavors. In this research, the mixing length for the turbulent momentum field has been the primary indicator of turbulent mixing. With an eye toward wind energy applications, wind turbine models are evaluated for their efficacy and computational requirements.

The research presented in chapter 4 highlights a fundamental flaw in assuming that theories of stably stratified turbulence developed from small-scale DNS and laboratory experiments hold for highly energetic geophysical flows. This disconnect is elucidated through a direct comparison of an ensemble data set through dimensional analysis of stability, mixing, and energetic parameters.

In chapter 4, the efficacy of $L_{kS} \equiv k^{1/2}/S$ in predicting the actual mixing length of the turbulent momentum field, L_M, is assessed. This concept is fully explored in chapter 5 with the additional length scale $L_{kN} \equiv k^{1/2}/N$. From these length scale parameterizations, estimates for eddy viscosity and diffusivity are evaluated *a priori* for observational field data and LES results of the stable atmospheric boundary layer.

The proposed parameterizations are tested in a numerical modeling framework in chapter 6. The developed hybrid closure model is based on fundamental observations in chapters

4 and 5 performing well compared with existing models without additional empiricism or tuning model parameters.

In chapter 7, the groundwork is laid for studying the implications of the stably stratified atmospheric boundary layer on wind energy through CFD simulations of wind turbine models under neutrally stratified conditions.

8.2. Conclusions on Key Findings

A summary of the key findings of this research are:

- Turbulent mixing measured by the non-dimensional effective eddy viscosity, ν_{eff}/ν, in the atmospheric boundary layer is sustained at strong stability ($Ri \approx 10$). For evaluating large energy-containing motions in shear flows, the shear production of turbulent kinetic energy, P, is a valuable parameter from which the relevant timescale is given by $T_P \equiv k/P$. This trend of strong mixing at high stability is also confirmed using the buoyancy parameter, NT_P, where the turbulent production Reynolds number, $Re_P = k^2/(\nu P)$, provides insights on the energetics of these large-scale motions. This research represents one of the first major uses of P rather than ε in evaluating large-scale motions.
- The stress-intensity ratio, c^2, at very high-Re remains relatively unaffected by stability. While c^2 has been widely studied in unstratified flows, the presentation in chapter 5 as a function of Ri is the first time that this near constant energetic value, $c^2 \approx 0.25$, has been observed in the context of stably stratified turbulence.
- The pertinent length scale L_{kS} accurately estimates the actual mixing length, L_M, of large-scale turbulent motions regardless of stability. For observational data, L_{kS} holds near the neutral limit up to $Ri \approx 10$. The bandwidth of applicability is smaller

for DNS and laboratory data ($0 \leq Ri \lesssim 1$), resulting from low-Re effects following a trajectory of turbulence collapse for $Ri \sim O(1)$. In this case, L_{kN} is shown to be an appropriate estimate for L_M. Using a turbulent kinetic energetic energy closure, the estimates for eddy viscosity, $\tilde{K}_{M_{kS}}$ and $\tilde{K}_{M_{kN}}$, are found to be accurate measures of K_M.

- The key turbulence parameterizations are applied towards developing an improved numerical model without reliance on damping and/or stability functions. This task is accomplished through direct application of parameterizations from high-Re flows under stable flow conditions. A conceptual extension towards wind energy applications begins with an evaluation of CFD wind turbine models. Studying the wake interactions provides valuable knowledge for further studies on effects under stable stratification.

8.3. Suggestions for Future Research

The numerical model development presented here requires additional effort. The first task is to employee a single equation model with a diagnostic formula for ε. Second, high-Re validation simulations will be carried out, such as the idealized GABLS intercomparison cases. Upon completion, this research will be submitted for publication as a follow-up to the research presented in chapter 5. Further insights will come to light on the implementation of the parameterizations. The intent is to then implement this model within the weather research and forecasting (WRF) model to test with idealized and real model cases.

Additionally, the research presented in chapter 7 provides a platform to evaluate wind turbine interactions under stable conditions. The results of the initial study elucidate that the actuator line model provides a realistic description of a downstream wakes from large-scale

horizontal-axis wind turbines in a computationally efficient manner. Turbulence parameterizations developed in this current research will provide valuable information in the further evaluation of turbulence models for capturing stable boundary layer dynamics in addition to wind turbine wake interactions and restoration.

Furthermore, this research presents a new lens from which to view stably stratified turbulence in geophysical flows. Here, analysis was limited to observations of the atmospheric boundary layer where variance and covariance measurements of turbulence are available which is not the case oftentimes in oceanic studies. As measurement techniques are refined and such data becomes available filtering techniques will need to be investigated, such the methodology of Vickers and Mahrt (2003), to isolate turbulent events from internal wave motions. While it may not be feasible to isolate turbulence from wave motions with absolute certainty, advances in SODAR and LIDAR technologies may overcome some of the limitations of sonic anemometry. These technologies are advantageous in their ability to provide four-dimensional measurements giving clarity to non-stationary tendencies of stably stratified turbulence.

Finally, the fundamental turbulence theory of down-gradient energy transfer has come into question in recent years. High-Re geophysical flows bring about additional mechanisms of turbulence generation and dissipation which have only just begun to be studied. With technological innovations in high fidelity measurements in the natural environment and exponential increases in computational power allowing for unprecedented DNS simulations, the time is right to explore the fundamental mechanisms of turbulence under neutral and stably stratified conditions. It is acknowledged that this by no means a inconsequential task and would require an extensive collaborative effort.

REFERENCES

Aitken, M. L., B. Kosovi, J. D. Mirocha, and J. K. Lundquist, 2014: Large eddy simulation of wind turbine wake dynamics in the stable boundary layer using the weather research and forecasting model. *J. Renewable and Sustainable Energy*, **6 (3)**.

Alinot, C. and C. Masson, 2002: Aerodynamic simulations of wind turbines operating in atmospheric boundary layer with various thermal stratifications. *40th collection of technical papers*, Reno, NV, ASME Wind Energy Symposium, AIAA-2002-42.

Alinot, C. and C. Masson, 2005: k-ε model for the atmospheric boundary layer under various thermal stratifications. *J. Sol. Energy Eng.*, **127 (4)**, 438–443.

André, J. C., G. De Moor, P. Lacarrère, G. Therry, and R. du Vachat, 1978: Modeling the 24-hour evolution of the mean and turbulent structures of the planetary boundary layer. *J. Atmos. Sci.*, **35**, 1861–1883.

Andreas, E. I., C. W. Fairall, P. S. Guest, and P. O. G. Persson, 1999: An overview of the SHEBA atmospheric surface flux program, Dallas, TX, USA. American Meteorological Society., 550–555, 13th Symposium on Boundary Layers and Turbulence.

Andrén, A., A. R. Brown, J. Graf, P. J. Mason, C.-H. Moeng, F. T. M. Nieuwstadt, and U. Schumann, 1994: Large-eddy simulation of a neutrally stratified boundary layer: A comparison of four computer nodes. *Quart. J. Roy. Meteorol. Soc.*, **120**, 1457–1484.

ANSYS, 2010: *ANSYS FLUENT User's Guide*. Canonsburg.

Apsley, D. D. and I. P. Castro, 1997: A limited-length-scale k-ε model for the neutral and stably-stratified atmospheric boundary layer. *Bound.-Lay. Meteorol.*, **83 (1)**, 75–98.

Armenio, V. and S. Sakar, 2002: An investigation of stably stratified turbulent channel flow using large-eddy simulation. *J. Fluid Mech.*, **459**, 1–42.

Balogh, M., A. Parente, and C. Benocci, 2012: RANS simulation of ABL flow over complex terrains applying an enhanced k-ε model and wall function formulation: Implementation and comparison for Fluent and OpenFOAM. *J. Wind Eng. Ind. Aerodyn.*, **104-106**, 360–368.

Bartello, P., 1995: Geostropic adjustment and inverse cascades in rotating stratified turbulence. *J. Atmos. Sci.*, **52**, 4410–4428.

Baumert, H. and H. Peters, 2000: Second-order closures and length scales for weakly stratified turbulent shear flows. *J. Geophys. Res.*, **105**, 6453–6468.

Bazilevs, Y., M.-C. Hsu, I. Akkerman, S. Wright, K. Takizawa, B. Henicke, T. Spielman, and T. E. Tezduyar, 2011a: 3D simulation of wind turbine rotors at full scale. Part I: Geometry modeling and aerodynamics. *Int. J. Numer. Methods Fluids*, **65 (1-3)**, 207–235.

Bazilevs, Y., M.-C. Hsu, J. Kiendl, R. Wüchner, and K.-U. Bletzinger, 2011b: 3D simulation of wind turbine rotors at full scale. Part II: Fluid-structure interaction modeling with composite blades. *Int. J. Numer. Methods Fluids*, **65 (1-3)**, 236–253.

Beare, R. J. and Coauthors, 2006: An intercomparison of large-eddy simulations of the stable boundary layer. *Bound.-Lay. Meteorol.*, **118 (2)**, 247–272.

Beljaars, A. C. M. and A. A. M. Holtslag, 1991: Flux parameterizations over land surfaces for atmospheric models. *J. Appl. Meteorol.*, **30**, 327–341.

Beljaars, A. C. M. and P. Viterbo, 1998: Role of the boundary layer in a numerical weather prediction model. *Clear and Cloudy Boundary Layers*, A. Holtslag and P. Duynkerke, Eds., Royal Netherlands Academy of Arts and Sciences, Amsterdam, 287–304.

Blackadar, A. K., 1957: Boundary layer wind maxima and their significance for the growth of nocturnal inversions. *Bull. Amer. Meteorol. Soc.*, **38 (5)**, 283–290.

Blackadar, A. K., 1962: The vertical distribution of wind and turbulent exchanges in neutral atmosphere. *J. Geophys. Res.*, **67**, 3095–3102.

Blumen, W., R. Banta, S. P. Burns, D. C. Fritts, R. Newsom, G. S. Poulos, and J. Sun, 2001: Turbulence statistics of a Kelvin-Helmholtz billow event observed in the night-time boundary layer during the Cooperative Atmospheric-Surface Exchange Study field program. *Dyn. Atmos. Oceans*, **34**, 189–204.

Bowen, B. M., 1996: Example of reduced turbulence during thunderstorm outflows. *J. Appl. Meteorol.*, **35**, 1028–1032.

Brost, R. A. and J. C. Wyngaard, 1978: A model study of the stably stratified planetary boundary layer. *J. Atmos. Sci.*, **35**, 1427–1440.

Burchard, H. and H. Baumert, 1995: On the performance of a mixed-layer model based on the k–ε turbulence closure. *J. Geo. Res.-Oceans*, **100 (C5)**, 8523–8540.

Burton, T., D. Sharpe, N. Jenkins, and E. Bossanyi, 2001: *Wind Energy Handbook*. Wiley.

Businger, J., J. Wyngaard, Y. Izumi, and E. Bradley, 1971: Flux-profile relationships in the atmospheric surface layer. *J. Atmos. Sci.*, **28**, 181–189.

Calaf, M., C. Meneveau, and J. Meyers, 2010: Large eddy simulation study of fully developed wind-turbine array boundary layers. *Phys. Fluids*, **22 (1)**.

Canuto, V. M., Y. Cheng, A. M. Howard, and I. N. Esau, 2008: Stably stratified flows: A model with no Ri(cr)*. *J. Atmos. Sci.*, **65**, 2437–2447.

Cermak, J. E., 1971: Laboratory simulation of the atmospheric boundary layer. *AIAA J.*, **9 (9)**, 1746–1754.

Cheng, Y. and W. Brutsaert, 2005: Flux-profile relationships for wind speed and temperature in the stable atmospheric boundary layer. *Bound.-Lay. Meteorol.*, **114 (3)**, 519–538.

Cheng, Y., V. M. Canuto, and A. M. Howard, 2002: An improved model for the turbulent PBL. *J. Atmos. Sci.*, **59 (9)**, 1550–1565.

Churchfield, M. J., S. Lee, J. Michalakes, and P. J. Moriarty, 2012a: A numerical study of the effects of atmospheric and wake turbulence on wind turbine dynamics. *J. Turb.*, **13 (14)**, 1–32.

Churchfield, M. J., S. Lee, P. J. Moriarty, L. A. Martinez, S. Leonardi, G. Vijayakumar, and J. G. Brasseur, 2012b: Large-eddy simulation of wind plant aerodynamics. Tech. Rep. NREL/CP-500-53554, National Renewable Energy Laboratory (NREL).

Churchfield, M. J., P. J. Moriarty, G. Vijayakumar, and J. G. Brasseur, 2010: Wind energy-related atmospheric boundary layer large-eddy simulation using OpenFOAM. Tech. Rep. NREL/CP-500-48905, National Renewable Energy Laboratory (NREL).

Clarke, R. H., A. J. Dyer, R. R. Brook, D. G. Reid, and A. J. Troup, 1971: The Wangara experiment: Boundary layer data. Tech. rep., Div. Meteorol. Phys. CSIRO, Australia.

Coleman, G. N., J. H. Ferziger, and P. R. Spalart, 1990: A numerical study of the turbulent Ekman layer. *J. Fluid Mech.*, **213**, 313–348.

Coleman, G. N., J. H. Ferziger, and P. R. Spalart, 1992: Direct simulation of the stably stratified turbulent Ekman layer. *J. Fluid Mech.*, **244**, 677–712.

Corrsin, A., 1958: Local isotropy in turbulent shear flow. *NACA research memorandum 58B11.*

Counihan, J., 1969: An improved method of simulating an atmospheric boundary layer in a wind tunnel. *Atmos. Environ.*, **3**, 197–214.

Crespo, A., F. Manuel, D. Moreno, E. Fraga, and J. Hernández, 1985: Numerical analysis of wind turbine wakes. *Proceedings of the Delphi Workshop on Wind Energy Applications*, Delphi, Greece, 15–25.

Cuxart, J. and Coauthors, 2006: Single-column model intercomparison for a stably stratified atmospheric boundary layer. *Bound.-Lay. Meteorol.*, **118 (2)**, 273–303.

Davis, C. J., 2011: Computational modeling of wind turbine wake interactions. M.S. thesis, Colorado State University, Fort Collins, CO.

De Silva, I. P. D., H. J. S. Fernando, F. Eaton, and D. Hebert, 1996: Evolution of Kelvin-Helmholtz billows in nature and laboratory. *Earth Planet. Sci. Lett.*, **143 (1)**, 217–231.

Delage, Y., 1974: A numerical study of the nocturnal atmospheric boundary layer. *Quart. J. Roy. Meteorol. Soc.*, **100**, 351–364.

Derbyshire, H., 1994: A balanced approach to stable boundary layer dynamics. *J. Atmos Sci.*, **51**, 3486–3504.

Derbyshire, S. H., 1990: Nieuwstadt's stable boundary layer revisited. *Quart. J. Roy. Meteorol. Soc.*, **116**, 127–158.

Detering, H. W. and D. Etling, 1985: Application of the e-ε turbulence model to the atmospheric boundary layer. *Bound.-Lay. Meteorol.*, **33 (2)**, 113–133.

Deusebio, E., G. Brethouwer, P. Schlatter, and E. Lindborg, 2014: A numerical study of the unstratified and stratified Ekman layer. *J. Fluid Mech.*, **755**, 672–704.

Dougherty, J. P., 1961: The anisotropy of turbulence at the meteor level. *J. Atmos. Terr. Phys.*, **21 (2–3)**, 210–213.

Durbin, P. A. and B. A. Pettersson Reif, 2001: *Statistical Theory and Modeling for Turbulent Flows*. Wiley.

Duynkerke, P. G. and G. M. Driedonks, 1987: A model for the turbulent structure of the stratocumulus-topped atmospheric boundary layer. *J. Atmos. Sci.*, **71**, 43–64.

Dyer, A. J., 1974: A review of flux-profile relationships. *Bound.-Lay. Meteorol.*, **7**, 363–372.

Ekman, V. W., 1905: On the influence of the earth's rotation on ocean currents. *Arkiv Matematik Astron. Fysik*, **2**, 1–53.

Ellison, T. H., 1957: Turbulent transport of heat and momentum from an infinite rough plane. *J. Fluid Mech.*, **200**, 563–594.

Ferziger, J. H. and P. Milovan, 1996: *Computational Methods for Fluid Dynamics*. Springer.

Finnigan, J. J. and S. E. Belcher, 2004: Flow over a hill covered with a plant canopy. *Quart. J. Roy. Meteorol. Soc.*, **130 (596)**, 1–29.

Fitch, A. C., J. K. Lundquist, and J. B. Olson, 2013a: Mesoscale influences of wind farms throughout a diurnal cycle. *Mon. Wea. Rev.*, **141**, 2173–2198.

Fitch, A. C., J. B. Olson, and J. K. Lundquist, 2013b: Parameterizations of wind farms in climate models. *J. Clim.*, **26 (17)**, 6439–6458.

Flores, O. and J. Riley, 2011: Analysis of turbulence collapse in the stably stratified surface layer using direct numerical simulation. *Bound.-Layer Meteorol.*, **139 (2)**, 241–259.

Foken, T., 2006: 50 years of the Monin-Obukhov similarity theory. *Bound.-Lay. Meteorol.*, **119**, 431–447.

Frandsen, S., 1992: On the wind speed reduction in the center of large clusters of wind turbines. *J. Wind Eng. Ind. Aerodyn.*, **39**, 251–265.

Frandsen, S., R. Barthelmie, S. Pryor, O. Rathmann, S. Larsen, J. Højstrup, and M. Thøgersen, 2006: Analytical modeling of wind speed deficit in large offshore wind farms. *Wind Energy*, **9**, 39–53.

Freedman, F. R. and M. Z. Jacobson, 2003: Modification of the standard ε-equation for the stable ABL through enforced consistency with Monin-Obukhov similarity theory. *Bound.-Lay. Meteorol.*, **106**, 383–410.

Galperin, B., A. Sukoriansky, and P. S. Anderson, 2007: On the critical Richarson number in stably stratified turbulence. *Atmos. Sci. Lett.*, **8**, 65–69.

Garcia, J. R. and J. P. Mellado, 2012: Direct numerical simulation of a dry shear-free convective boundary layer, 65th Annual Meeting of the Division of Fluid Dynamics, American Physical Society. San Diego, CA.

García-Villalba, M. and J. C. del Álamo, 2011: Turbulence modification by stable stratification in channel flow. *Phys. Fluids*, **23 (4)**.

Garratt, J. R., 1982: Observations in the nocturnal boundary layer. *Bound.-Lay. Meteorol.*, **22**, 21–48.

Garratt, J. R., 1990: The internal boundary layer a review. *Bound.-Lay. Meteorol.*, **50 (1-4)**, 171–203.

Garratt, J. R., 1992: *The Atmospheric Boundary Layer*. Cambridge University Press.

Gerz, T., U. Schumann, and S. E. Elghobashi, 1989: Direct numerical simulation of stratified homogeneous turbulent shear flows. *J. Fluid Mech.*, **200**, 563–594.

Gibson, C. H., 1980: *Marine Turbulence*, chap. Fossil temperature, salinity, and vorticity turbulence in the ocean, 221–257. Elsevier.

Gibson, C. H., 1999: Fossil turbulence revisited. *J. Mar. Syst.*, **21**, 147–167.

Gómez-Elvira, R., A. Crespo, E. Migoya, F. Manuel, and J. Hernández, 2005: Anisotropy of turbulence in wind turbine wakes. *J. Wind Eng. Ind. Aerodyn.*, **93 (10)**, 797–814.

Gorlé, C., J. v. Beeck, P. Rambaud, and G. V. Tendeloo, 2009: CFD modelling of small particle dispersion: The influence of the turbulence kinetic energy in the atmospheric boundary layer. *Atmospheric Environment*, **43 (3)**, 673–681.

Grachev, A. A., E. L. Andreas, C. W. Fairall, P. S. Guest, and P. O. G. Persson, 2005: Stable boundary-layer scaling regimes: the SHEBA data. *Bound.-Lay. Meteorol.*, **116 (2)**, 201–235.

Grachev, A. A., E. L. Andreas, C. W. Fairall, P. S. Guest, and P. O. G. Persson, 2013: The critical Richardson number and limits of applicability of local similarity theory in the stable boundary layer. *Bound.-Lay. Meteorol.*, **147**, 51–82.

Grachev, A. A., E. L. Andreas, C. W. Fairall, P. S. Guest, and P. O. G. Persson, 2014: Similarity theory based on the Dougherty-Ozmidov length scale. *Manuscript submitted to Quart. J. Roy. Meteorol. Soc.*

Gregg, M. C., 1987: Diapycnal mixing in the thermocline. *J. Geophys. Res.*, **92**, 5249–5286.

Grisogono, B. and Belušić, 2008: Improving mixing length-scale for stable boundary layers. *Quart. J. Roy. Meteorol. Soc.*, **134**, 2185–2192.

Hargreaves, D. M. and N. G. Wright, 2007: On the use of the k–ε model in commercial CFD software to model the neutral atmospheric boundary layer. *J. Wind Eng. Ind. Aerodyn.*, **95 (5)**, 355–369.

Högström, U., D. N. Asimakopoulos, H. Kambezidis, C. G. Helmis, and A. Smedman, 1988: A field study of the wake behind a 2 MW wind turbine. *Atmospheric Environment*, **22 (4)**, 803–820.

Holt, S. E., J. R. Koseff, and J. H. Ferziger, 1992: A numerical study of the evolution and structure of homogeneous stably stratified sheared turbulence. *J. Fluid Mech.*, **237**, 499–539.

Holt, T. and S. Raman, 1988: A review and comparative evaluation of multilevel boundary layer parameterizations for first-order and turbulent kinetic energy closure schemes. *R. Geophys.*, **26 (4)**, 761–780.

Holtslag, A. and F. Nieuwstadt, 1986: Scaling the atmospheric boundary layer. *Bound.-Lay. Meteorol.*, **36 (1-2)**, 201–209.

Hopfinger, E. J., 1973: Development of a stratified shear flow, Novosibirsk, USSR. American Society of Civil Engineers, New York, 553565, International Symposium on Stratified Flows.

Hopfinger, E. J., 1987: Turbulence in stratified fluids: A review. *J. Geophys. Res.*, **92**, 5287–5303.

Howard, L., 1961: Note on a paper of John W. Miles. *J. Fluid Mech.*, **10**, 509–512.

Hoyas, S. and J. Jiménez, 2006: Scaling of the velocity fluctuations in turbulent channels up to $Re_\tau = 2003$. *Phys. Fluids*, **18**.

Huang, J., E. Bou-Zeid, and J.-C. Golaz, 2013: Turbulence and vertical fluxes in the stable atmospheric bounday layer. Part II: A novel mixing-length model. *J. Atmos. Sci.*, **70**, 1528–1542.

Hunt, J. S. R., J. C. Kaimal, and J. E. Gaynor, 1985: Some observations of turbulence structure in stable layers. *Quart. J. Roy. Meteorol. Soc.*, **111**, 793–815.

Itsweire, E. C., K. N. Helland, and C. W. V. Atta, 1986: The evolution of grid-generated turbulence in a stably stratified fluid. *J. Fluid Mech.*, **162**, 299–338.

Itsweire, E. C., J. R. Koseff, D. A. Briggs, and J. H. Ferziger, 1993: Turbulence in stratified shear flows: Implications for interpreting shear-induced mixing in the ocean. *J. Phys. Oceanogr.*, **23 (7)**, 1508–1522.

Ivey, G. N. and G. M. Corcos, 1982: Boundary mixing in a stratified fluid. *J. Fluid Mech.*, **121**, 1–26.

Ivey, G. N. and J. Imberger, 1991: On the nature of turbulence in a stratified fluid. Part I: The energetics of mixing. *J. Phys. Oceanogr.*, **21**, 650–658.

Ivey, G. N., K. B. Winters, and J. R. Koseff, 2008: Density stratification, turbulence, but how much mixing? *Annu. Rev. Fluid Mech.*, **40**, 169–184.

Jones, W. and B. Launder, 1972: The prediction of laminarization with a two-equation model of turbulence. *Int. J. Heat Mass Tran.*, **15 (2)**, 301–314.

Jonkman, J., S. Butterfield, W. Musial, and G. Scoot, 2009: Definition of a 5-MW reference wind turbine for offshore system development. Tech. Rep. NREL/TP-500-38060, National Renewable Energy Laboratory (NREL).

Kaimal, J. C. and J. J. Finnigan, 1994: *Atmospheric Boundary Layer Flows: Their Structure and Measurement*. Oxford University Press.

Karimpour, F. and S. K. Venayagamoorthy, 2014a: A revisit of the equilibrium assumption for predicting near-wall turbulence. *J. Fluid Mech. (In press)*.

Karimpour, F. and S. K. Venayagamoorthy, 2014b: A simple turbulence model for stably stratified wall-bounded flows. *J. Geophys. Res.-Oceans*.

Kasmi, A. E. and C. Masson, 2008: An extended k-ε model for turbulent flow through horizontal-axis wind turbines. *J. Wind Eng. Ind. Aerodyn.*, **96 (1)**, 103–122.

Kays, W. M., 1994: Turbulent Prandtl number - where are we? *J. Heat Transfer*, **116**, 284–295.

Kays, W. M. and M. E. Crawford, 1993: *Convective Heat and Mass Transfer*. McGraw-Hill.

Keller, K. H. and C. W. van Atta, 2000: An experimental investigation of the vertical temperature structure of homogeneous stratified shear turbulence. *J. Fluid Mech.*, **425**, 1–29.

Kelley, N., M. Shirazi, D. Jager, S. Wilde, J. Adams, M. Buhl, P. Sullivan, and E. Patton, 2004: Lamar low-level jet project interim report. Tech. Rep. NREL/TP-500-34593, National Renewable Energy Laboratory (NREL).

Kim, J. and L. Mahrt, 1992: Simple formulation of turbulent mixing in the stable free atmosphere and nocturnal boundary layer. *Tellus A*, **44 (5)**, 381–394.

Klipp, C. L. and L. Mahrt, 2004: Flux-gradient relationship, self-correlation and intermittency in the stable boundary layer. *Quart. J. Roy. Meteorol. Soc.*, **130 (601)**, 2087–2103.

Kolmogorov, A. N., 1941: The local structure of turbulence in incompressible viscous fluid for very large Reynolds number. *Dokl. Akad. Nauk SSSR*, **30**, 299–303.

Kondo, J., O. Kanechika, and N. Yasuda, 1978: Heat and momentum transfers under strong stability in the atmospheric surface layer. *J. Atmos. Sci.*, **35 (6)**, 1012–1021.

Kosović, B., 1997: Subgrid-scale modelling for the large-eddy simulation of high-reynolds-number boundary layers. *J. Fluid Mech.*, **336**, 151–182.

Kosović, B. and J. A. Curry, 2000: A large eddy simulation of a quasi-steady, stably stratified atmospheric boundary layer. *J. Atmos. Sci.*, **57**, 1052–1068.

Launder, B. E. and D. B. Spalding, 1972: *Mathematical Models of Turbulence*. Academic.

Launder, B. E. and D. B. Spalding, 1974: The numerical computation of turbulent flows. *Comput. Method. Appl. M.*, **3 (2)**, 269–289.

Lee, N. H. and S. U. Kao, 1979: Finite-element numerical modeling of atmospheric turbulent boundary layer. *J. Appl. Meteorol.*, **18**, 1287–1295.

Lelong, M.-P. and T. J. Dunkerton, 1998: Inertia-gravity wave breaking in three dimensions. Part I: Convectively stable waves. *J. Atmos. Sci.*, **55 (15)**, 2473–2488.

Lilly, D. K., 1983: Stratified turbulence and the mesoscale variability of the atmosphere. *J. Atmos. Sci.*, **40**, 749–761.

Lin, J.-T. and Y.-H. Pao, 1979: Wakes in stratified fluids. *Annu. Rev. Fluid Mech.*, **11**, 317–338.

Lin, J.-T. and S. D. Veenhuizen, 1974: Measurements of the decay of grid generated turbulence in a stably stratified fluid. *Bull. Am. Phys. Soc.*, **19**, 1142–1143.

Lombard, P. N. and J. J. Riley, 1996: On the breakdown into turbulence of propagating internal waves. *Dyn. Atmos. Oceans*, **23 (1)**, 345–355.

Lu, H. and F. Porté-Agel, 2011: Large-eddy simulation of a very large wind farm in a stable atmospheric boundary layer. *Phys. Fluids*, **23 (6)**.

Madsen, H. A., 1996: A CFD analysis for the actuator disc flow compared with momentum theory results. *Proceedings of the 10th IEA Symposium of Aerodynamics and Wind Turbines*, Lyngby, Denmark: Technical University of Denmark.

Mahrt, L., 1989: Intermittency of atmospheric turbulence. *J. Atmos. Sci.*, **46**, 79–95.

Mahrt, L., 1998: Stratified atmospheric boundary layers and breakdown of models. *Theor. Comp. Fluid Dyn.*, **11**, 263–279.

Mahrt, L., 1999: Stratified atmospheric boundary layers. *Bound.-Lay. Meteorol.*, **90**, 375–396.

Mahrt, L., 2007: Weak-wind mesoscale meandering in the nocturnal boundary layer. *Environ. Fluid Mech.*, **7**, 331–334.

Mahrt, L., 2014: Stably stratified atmospheric boundary layers. *Annu. Rev. Fluid Mech.*, **46**, 23–45.

Mahrt, L. and D. Vickers, 2002: Contrasting vertical structures of nocturnal boundary layers. *Bound.-Lay. Meteorol.*, **105**, 351–363.

Mahrt, L. and D. Vickers, 2005: Boundary layer adjustment over small-scale changes of surface heat flux. *Bound.-Lay. Meteorol.*, **116**, 313–330.

Mahrt, L. and D. Vickers, 2006: Extremely weak mixing in stable consitions. *Bound.-Lay. Meteorol.*, **119**, 19–39.

Marchuk, G. I., V. P. Kochergin, V. I. Klimok, and V. A. Sukhorukov, 1977: On the dynamics of the ocean surface mixed layer. *J. Phys. Oceanogr.*, **7**, 865–875.

Marlatt, S., S. Waggy, and S. Biringen, 2012: Direct numerical simulation of the turbulent Ekman layer: Evaluation of closure models. *J. Atmos. Sci.*, **69**, 1106–1117.

Martinez, L. A., S. Leonardi, M. J. Churchfield, and P. J. Moriarty, 2012: A comparison of actuator disc and actuator line wind turbine models and best practices for their use. *50^{th} AIAA Aerospace Sciences Meeting and Exhibit*, Washington, D. C., AIAA.

Marušic, I. and A. E. Perry, 1995: A wall-wake model for the turbulence structure of boundary layers. Part 2. Further experimental support. *J. Fluid Mech.*, **298**, 389–407.

Mason, P. J. and S. H. Derbyshire, 1990: Large-eddy simulation of the stably-stratified atmospheric boundary layer. *Bound.-Lay. Meteorol.*, **53**, 117–162.

Mason, P. J. and R. I. Sykes, 1980: A two-dimensional numerical study of horizontal roll vortices in the neutral atmospheric boundary layer. *Quart. J. Roy. Meteorol. Soc.*, **106**, 351–366.

Mason, P. J. and D. J. Thomson, 1987: Large-eddy simulations of the neutral-static-stability planetary boundary layer. *Quart. J. Roy. Meteorol. Soc.*, **113 (476)**, 413–443.

Mater, B. D., S. M. Schaad, and S. K. Venayagamoorthy, 2013: Relevance of the Thorpe length scale in stably stratified turbulence. *Phys. Fluids*, **25 (7)**.

Mater, B. D. and S. K. Venayagamoorthy, 2014a: A unifying framework for parameterizing stably stratified shear-flow turbulence. *Phys. Fluids*, **26 (3)**.

Mater, B. D. and S. K. Venayagamoorthy, 2014b: The quest for an unambiguous parameterization of mixing efficiency in stably stratified geophysical flows. *Geophys. Res. Lett.*, **41**, 4646–4653.

Mauritsen, T., G. Svensson, S. S. Zilitinkevich, I. Esau, L. Enger, and B. Grisogono, 2007: A total turbulent energy closure model for neutrally and stably stratified atmospheric boundary layers. *J. Atmos. Sci.*, **64**, 4113–4126.

McEligot, D. M. and M. F. Taylor, 1996: The turbulent Prandtl number in the near-wall region for low-Prandtl-number gas mixtures. *Int. J. Heat Mass Transfer*, **39 (6)**, 1287 – 1295.

Mellor, G. L. and P. A. Durbin, 1975: The structure and dynamics of the ocean surface mixed layer. *J. Phys. Oceanogr.*, **5 (4)**, 718–728.

Mellor, G. L. and T. Yamada, 1982: Development of a turbulence closure model for geophysical fluid problems. *Rev. Geophys.*, **20 (4)**, 851–875.

Menter, F. R., 1994: Two-equation eddy-viscosity turbulence models for engineering applications. *AIAA J.*, **32 (8)**, 1598–1605.

Menter, F. R., 2009: Review of the shear-stress transport turbulence model experience from an industrial perspective. *Int. J. Comp. Fluid Dyn.*, **23 (4)**, 305–316.

Meyers, J. and C. Meneveau, 2012: Optimal turbine spacing in fully developed wind farm boundary layers. *Wind Energy*, **15 (2)**, 305–317.

Mikkelsen, R., 2003: Actuator disc methods applied to wind turbines. Ph.D. thesis, Technical University of Denmark, Denmark.

Miles, J. W., 1961: On the stability of heterogeneous shear flows. *J. Fluid Mech.*, **10**, 496–508.

Mirocha, J. D., B. Kosovic, M. L. Aitken, and J. K. Lundquist, 2014: Implementation of a generalized actuator disk wind turbine model into the weather research and forecasting model for large-eddy simulation applications. *J. Renewable and Sustainable Energy*, **6 (1)**.

Miyashita, K., K. Iwamoto, and H. Kawamura, 2006: Direct numerical simulation of the neutrally stratified turbulent Ekman boundary layer. *J. Earth Sim.*, **6**, 3–15.

Moeng, C.-H. and P. P. Sullivan, 1994: A comparison of shear- and buoyancy-driven planetary boundary layer flows. *J. Atmos. Sci.*, **51**, 999–1022.

Moeng, C.-H. and J. C. Wyngaard, 1984: Statistics of conservative scalars in the convective boundary layer. *J. Atmos. Sci.*, **41 (21)**, 3161–3169.

Monin, A. S. and A. M. Obukhov, 1954: Basic laws of turbulent mixing in the surface layer of the atmosphere. *Contrib. Geophys. Inst. Acad. Sci. USSR*, **151**, 163–187.

Monin, A. S. and A. M. Yaglom, 1971: *Statistical Fluid Mechanics: Mechanics of Turbulence, Vol 1.* MIT Press.

Munk, W. H. and E. R. Anderson, 1948: Notes on the theory of the thermocline. *J. Mar. Res.*, **3**, 276–295.

Nakanishi, M., 2001: Improvement of the Mellor-Yamada turbulence closure model based on large-eddy simulation data. *Bound.-Lay. Meteorol.*, **99**, 349–378.

Newsom, R. K. and R. M. Banta, 2003: Shear instability gravity waves in the stable nocturnal boundary layer as observed by dopple lidar during CASES-99. *J. Atmos. Sci.*, **60**, 16–33.

Nieuwstadt, F. T. M., 1984: The turbulent structure of the stable, nocturnal boundary layer. *J. Atmos. Sci.*, **41 (14)**, 2202–2216.

Nieuwstadt, F. T. M., 2005: Direct numerical simulation of stable channel flow at large stability. *Bound.-Layer Meteorol.*, **116 (2)**, 277–299.

Obukhov, A. M., 1946: Turbulence in an atmosphere with a non-uniform temperature. *Trudy Inst. Theor. Geofiz.*, **1**, 95–115.

Ohya, Y., R. Nakamuram, and T. Uchida, 2008: Intermittent bursting of turbulence in a stable boundary layer with low-level jet. *Bound.-Lay. Meteorol.*, **126 (3)**, 349–363.

OpenCFD, 2012: *OpenFOAM: The open source CFD toolbox - progammer's guide v. 2.1.0.*

Ozmidov, R. V., 1965: On the turbulent exchange in a stably stratified ocean. *Izvestiya, Atmos. Ocean Physics*, **1 (8)**, 493–497.

Pahlow, M., M. Parlange, and F. Porté-Agel, 2001: On Monin–Obukhov similarity in the stable atmospheric boundary layer. *Bound.-Lay. Meteorol.*, **99 (2)**, 225–248.

Panofsky, H. A., H. Tennekes, D. H. Lenschow, and J. C. Wyngaard, 1977: The characterisitics of turbulent velocity components in the surface layer under convective conditions. *Bound.-Lay. Meteorol.*, **11**, 355–361.

Parente, A., C. Gorlé, J. v. Beeck, and C. Benocci, 2011a: Improved k–ε model and wall function formulation for the RANS simulation of ABL flows. *J. Wind Eng. Ind. Aerodyn.*, **99 (4)**, 267–278.

Parente, A., C. Gorlé, J. van Beeck, and C. Benocci, 2011b: A comprehensive modelling approach for the neutral atmospheric boundary layer: Consistent inflow conditions, wall functions and turbulence model. *Bound.-Lay. Meteorol.*, **140**, 411–428.

Peltier, W. R. and C. P. Caufield, 2003: Mixing efficiency in stratified shear flows. *Annu. Rev. Fluid Mech.*, **35**, 135–167.

Persson, P. O., C. W. Fairall, E. L. Andreas, P. S. Guest, and D. K. Perovich, 2002: Measurements near the atmospheric surface flux group at SHEBA: Near-surface conditions and surface energy budget. *J. Geophys. Res.*, **107 (C10)**, 8045.

Pope, S. B., 2000: *Turbulent Flows*. Cambridge University Press.

Porté-Agel, F., C. Meneveau, and M. B. Paralange, 2000: A scale-dependent dynamic model for large-eddy simulation: Application to a neutral atmospheric boundary layer. *J. Fluid Mech.*, **415**, 261–284.

Porté-Agel, F., Y.-T. Wu, H. Lu, and R. J. Conzemius, 2011: Large-eddy simulation of atmospheric boundary layer flow through wind turbines and wind farms. *J. Wind Eng. Ind. Aerodyn.*, **99 (4)**, 154–168.

Poulos, G. S. and Coauthors, 2002: CASES-99: A comprehensive investigation of the stable nocturnal boundary layer. *Bull. Amer. Meteorol. Soc.*, **85**, 555–581.

Prandtl, L., 1925: Bericht über die Entstehung der Turbulenz. *Z. Angew Math. Mech.*, **5**, 136–139.

Réthoré, P.-E. M., 2009: Wind turbine wake in atmospheric turbulence. Ph.D. thesis, Ris National Laboratory for Sustainable Energy.

Reynolds, O., 1894: On the dynamical theory of incompressible viscous flows and the determination of criterion. *Philos. Trans. R. Soc. London Ser.*, **A 186**, 123–161.

Richards, P. J. and R. P. Hoxey, 1993: Appropriate boundary conditions for computations wind engineering models using the k-ε turbulence model. *J. Wind Eng. Ind. Aerodyn.*, **46 & 47**, 145–153.

Richardson, L. F., 1920: The supply of energy from and to atmospheric eddies. *Proc. R. Soc. Lond. A.*, **97**, 354–373.

Richardson, L. F., 1922: *Weather Prediction by Numerical Process*. Cambridge University Press.

Riley, J. J. and S. M. deBruynKops, 2003: Dynamics of turbulence strongly influenced by buoyancy. *Phys. Fluids*, **15 (7)**, 2047–2059.

Riley, J. J. and M.-P. Lelong, 2000: Fluid motions in the presence of strong stable stratification. *Annu. Rev. Fluid Mech.*, **32**, 613–657.

Riley, J. J. and E. Lindborg, 2008: Stratified turbulence: A possible interpretation of some geophysical turbulence measurements. *J. Atmos. Sci.*, **65**, 2416–2424.

Rodi, W., 1980: Turbulence models and their application in hydraulics. State of the art paper, IAHR, Delft.

Rodi, W., 1987: Examples of calculation methods for flow and mixing in stratified fluids. *J. Geophys. Res.-Oceans*, **92 (C5)**, 5305–5328.

Rohr, J. J., E. C. Itsweire, K. N. Helland, and C. W. Van Atta, 1988: Growth and decay of turbulence in a stably stratified shear flow. *J. Fluid Mech.*, **195**, 77–111.

Schlatter, P., R. Örlü, Q. Li, G. Brethouwer, and J. H. M. Fransson, 2009: Turbulent boundary layers up to Re_θ=2500 studied through simulation and experiment. *Phys. Fluids*, **21**.

Schumann, U. and T. Gerz, 1995: Turbulent mixing in stably stratified shear flows. *J. Appl. Meteorol.*, **34**, 33–48.

Shih, L. H., J. R. Koseff, J. H. Ferziger, and C. R. Rehmann, 2000: Scaling and parameterization of stratified homogeneous turbulent shear flow. *J. Fluid Mech.*, **412**, 1–20.

Shih, L. H., J. R. Koseff, G. N. Ivey, and J. H. Ferziger, 2005: Parameterization of turbulent fluxes and scales using homogeneous sheared stably stratified turbulence simulations. *J. Fluid Mech.*, **525**, 193–214.

Smyth, W. D. and J. N. Moum, 2000: Anisotropy of turbulence in stably stratified mixing layers. *Phys. Fluids*, **12 (6)**, 1343–1362.

Sorbjan, Z., 1989: *Structure of the Atmospheric Boundary Layer*. Prentice Hall.

Sorbjan, Z., 2006: Local structure of turbulence in stably-stratified boundary layers. *J. Atmos. Sci.*, **63 (5)**, 1526–1537.

Sorbjan, Z., 2012: A study of the stable boundary layer based on a single-column K-theory model. *Bound.-Lay. Meteorol.*, **142**, 33–53.

Sorbjan, Z. and B. Balsley, 2008: Microstructure of turbulence in the stably stratified boundary layer. *Bound.-Lay. Meteorol.*, **129 (2)**, 191–210.

Sorbjan, Z. and A. A. Grachev, 2010: An evaluation of the flux-gradient relationship in the stable boundary layer. *Bound.-Lay. Meteorol.*, **135**, 385–405.

Sørensen, J. N. and C. W. Kock, 1995: A model for unsteady rotor aerodynamics. *J. Wind Eng. Ind. Aerodyn.*, **58**, 259–275.

Sørensen, J. N. and A. Myken, 1992: Unsteady actuator disc model for horizontal axis wind turbines. *J. Wind Eng. Ind. Aerodyn.*, **39**, 139–149.

Sørensen, J. N. and W. Z. Shen, 2002: Numerical modeling of turbine wakes. *J. Fluid Eng.*, **124**, 393–399.

Sørensen, N. N. and J. Johansen, 2007: Upwind, aerodynamics and aero-elasticiy, rotor aerodynamics in atmospheric shear conditions. 2007 European Wind Energy Conference and Exhibition, Milan, Italy, EWEA.

Spalart, P. R. and C. L. Rumsey, 2007: Effective inflow conditions for turbulence models in aerodynamic calculations. *AIAA*, **45 (10)**, 2544–2553.

Spedding, G. R., F. K. Browand, and A. M. Fincham, 1996: Turbulence, similarity scaling and vortex geometry in the wake of a towed sphere in a stably stratified fluid. *J. Fluid Mech.*, **314**, 53–103.

Srinivasan, C. and D. V. Papavassiliou, 2011: Prediction of the turbulent Prandtl number in wall flows with lagrangian simulations. *Ind. Eng. Chem. Res.*, **50 (15)**, 8881–8891.

Stewart, R. W., 1969: Turbulence and waves in a stratified atmosphere. *Radio Science*, **4 (12)**, 1269–1278.

Stillinger, D. C., K. N. Helland, and C. W. V. Atta, 1983: Experiments on the transition of homogeneous turbulence to internal waves in a stratified fluid. *J. Fluid Mech.*, **131**, 91–122.

Stovall, T., G. Pawlas, and P. J. Moriarty, 2010: Wind farm wake simulations in OpenFOAM. *48th AIAA Aerospace Sciences Meeting and Exhibit*, Orlando, Florida, AIAA.

Strang, E. J. and H. J. S. Fernando, 2001: Vertical mixing and transports through a stratified shear layer. *J. Phys. Oceanogr.*, **31 (8)**, 2026–2048.

Stull, R. B., 1988: *An Introduction to Boundary Layer Meteorology*. Springer.

Sullivan, P. P., J. C. McWilliams, and C.-H. Moeng, 1994: A subgrid-scale model for large-eddy simulation of planetary boundary-layer flows. *Bound.-Lay. Meteorol.*, **71**, 247–276.

Sumner, J. and C. Masson, 2012: The Apsley and Castro limited-length-scale k-ε model revisited for improved performance in the atmospheric surface layer. *Bound.-Lay. Meteorol.*, **144 (2)**, 199–215.

Sun, J., 2011: Vertical variations of mixing lengths under neutral and stable conditions during CASES-99. *J. Appl. Meteorol. Climatol.*, **50**, 2030–2041.

Sun, J. and Coauthors, 2004: Atmospheric disturbances that generate intermittent turbulence in nocturnal boundary layers. *Bound.-Lay. Meteorol.*, **110 (2)**, 255–279.

Sun, J., R. Desjardins, L. Mahrt, and I. MacPherson, 1998: Transport of carbon dioxide, water vapor, and ozone by turbulence and local circulations. *J. of Geophys. Res.-Atmos.*, **103 (D20)**, 25 873–25 885.

Svensson, U., 1979: The structure of the turbulent Ekman layer. *Tellus*, **31**, 340–350.

Taylor, G. I., 1931: Effects of variation in density on the stability of superimposed streams of fluids. *Proc. Roy. Soc. (Lond.), Ser.*, **132**, 499–523.

Tennekes, H. and J. L. Lumley, 1972: *A First Course in Turbulence*. The MIT Press.

Thorpe, S. A., 1973: Turbulence in stably stratified fluids: A review of laboratory experiments. *Bound.-Lay. Meteorol.*, **5**, 95–119.

Thorpe, S. A., 1982: On the clouds of bubbles formed by breaking wind-waves in deep water, and their role in air–sea gas transfer. *Phil. Trans. R. Soc. Lond.*, **304**, 155–210.

Tossas, L. A. M. and S. Leonardi, 2013: Wind turbine modeling for computational fluid dynamics. Tech. Rep. NREL/SR-5000-55054, National Renewable Energy Laboratory (NREL).

Townsend, A. A., 1958: The effects of radiative transfer on turbulent flow of a stratified fluid. *J. Fluid Mech.*, **3**, 361–372.

Townsend, A. A., 1976: *The Structure of Turbulent Shear Flow*. Cambridge University Press.

Troldborg, N., G. C. Larsen, H. A. Madsen, K. S. Hansen, J. N. Srensen, and R. Mikkelsen, 2011: Numerical simulations of wake interaction between two wind turbines at various inflow conditions. *Wind Energy*, **14 (7)**, 859–876.

Turner, J. S., 1973: *Buoyancy effects in fluids*. Cambridge University Press.

Uttal, T. and Coauthors, 2002: Surface heat budget of the arctic ocean. *Bull. Amer. Meteorol. Soc.*, **83**, 255–275.

Venayagamoorthy, S. K. and D. D. Stretch, 2010: On the turbulent Prandtl number in homogeneous stably stratified turbulence. *J. Fluid Mech.*, **644**, 359–369.

Vermeer, L. J., J. N. Sørensen, and A. Crespo, 2003: Wind turbine wake aerodynamics. *Prog. Aerosp. Sci.*, **39 (67)**, 467–510.

Vickers, D. and L. Mahrt, 2003: The cospectral gap and turbulent flux calculations. *J. Atmos. Oceanic Technol.*, **20 (5)**, 660–672.

Viterbo, P., A. Beljaars, J.-F. Mahfouf, and J. Teixeira, 1999: The representation of soil moisture freezing and its impact on the stable boundary layer. *Quart. J. Roy. Meteorol. Soc.*, **125 (559)**, 2401–2426.

Webster, C., 1964: An experimental study of turbulence in a density-stratified shear flow. *J. Fluid Mech.*, **19 (02)**, 221–245.

Weng, W. and P. Taylor, 2003: On modelling the one-dimensional atmospheric boundary layer. *Bound.-Lay. Meteorol.*, **107**, 371–400.

Weng, W. and P. A. Taylor, 2006: Modelling the one-dimensional stable boundary layer with an *e-l* turbulence closure scheme. *Bound.-Lay. Meteorol.*, **118 (2)**, 305–323.

Whiteman, C. D., X. Bian, and S. Zhong, 1997: Low-level jet climatology from enhanced rawinsonde observations at a site in the southern Great Plains. *J. Appl. Meteorol.*, **36**, 1363–1376.

Wilcox, D. C., 1988: Re-assessment of the scale-determing equation for advanced turbulence models. *AIAA J.*, **26 (11)**, 1299–1310.

Wilcox, D. C., 1993: *Turbulence Modelling for CFD*. DCW Industries Inc.

Willis, G. E. and J. W. Deardorff, 1974: A laboratory model of the unstable planetary boundary layer. *J. Atmos. Sci.*, **31**.

Wilson, J. D., 2012: An alternative eddy-viscosity model for the horizontally uniform atmospheric boundary layer. *Bound.-Lay. Meteorol.*, **145**, 165–184.

Wu, Y. T. and F. Porté-Agel, 2011: Large-eddy simulation of wind turbine wakes: Evaluation of turbine parametrisations. *Bound.-Lay. Meteorol.*, **138**, 345–366.

Wyngaard, J. C., 2010: *Turbulence in the Atmosphere*. Cambridge University Press.

Wyngaard, J. C. and O. R. Coté, 1972: Cospectral similarity in the atmospheric surface layer. *Quart. J. Roy. Meteorol. Soc.*, **98**, 590–603.

Xu, G. and L. N. Sankar, 2000: Computational study of horizontal axis wind turbines. *J. Sol. Energ.*, **122 (1)**, 35–39.

Yang, Y., M. Gu, S. Chen, and X. Jin, 2009: New inflow boundary conditions for modelling the neutral equilibrium atmospheric boundary layer in computational wind engineering. *J. Wind Eng. Ind. Aerodyn.*, **97 (2)**, 88–95.

Zhou, B. and F. K. Chow, 2012: Turbulence modeling for the stable atmospheric boundary layer and implications for wind energy. *Flow, Turbulence, and Combustion*, **88**, 255–277.

Zilitinkevich, S. S., 1972: On the determination of the height of the Ekman boundary layer. *Bound.-Lay. Meteorol.*, **3 (2)**, 141–145.

Zilitinkevich, S. S. and A. Baklanov, 2002: Calculation of the height of the stable boundary layer in practical applications. *Bound.-Lay. Meteorol.*, **105**, 389–409.

Zilitinkevich, S. S., T. Elperin, N. Kleeorin, and I. Rogachevskii, 2007: Energy-and flux-budget (EFB) turbulence closure model for stably stratified flows. Part I: steady-state, homogeneous regimes. *Bound.-Layer Meteorol.*, **125 (2)**, 167–191.

Zilitinkevich, S. S., T. Elperin, N. Kleeorin, I. Rogachevskii, and I. Esau, 2013: A hierarchy of energy-and flux-budget (EFB) turbulence closure models for stably-stratified geophysical flows. *Bound.-Layer Meteorol.*, **146 (3)**, 341–373.

Zilitinkevich, S. S., T. Elperin, N. Kleeorin, I. Rogachevskii, I. Esau, T. Mauritsen, and M. W. Miles, 2008: Turbulence energetics in stably stratified geophysical flows: Strong and weak mixing regimes. *Quart. J. Roy. Meteorol. Soc.*, **134 (633)**, 793–799.